CHEMICAL REVIEWS

pubs.acs.org/CR

Review

Phase Transitions and Dynamics in Mixed Three- and Low-Dimensional Lead Halide Perovskites

Mantas Simenas,* Anna Gagor, Juras Banys, and Miroslaw Maczka

Cite This: *Chem. Rev.* 2024, 124, 2281−2326

Read Online

ACCESS | Metrics & More | Article Recommendations

ABSTRACT: Lead halide perovskites are extensively investigated as efficient solution-processable materials for photovoltaic applications. The greatest stability and performance of these compounds are achieved by mixing different ions at all three sites of the $APbX_3$ structure. Despite the extensive use of mixed lead halide perovskites in photovoltaic devices, a detailed and systematic understanding of the mixing-induced effects on the structural and dynamic aspects of these materials is still lacking. The goal of this review is to summarize the current state of knowledge on mixing effects on the structural phase transitions, crystal symmetry, cation and lattice dynamics, and phase diagrams of three- and low-dimensional lead halide perovskites. This review analyzes different mixing recipes and ingredients providing a comprehensive picture of mixing effects and their relation to the attractive properties of these materials.

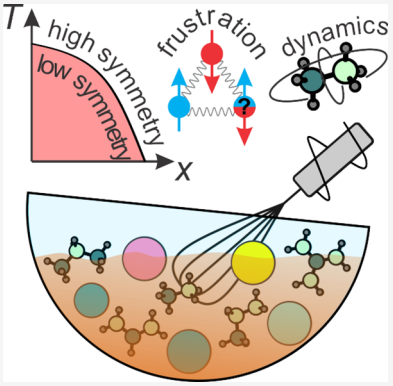

CONTENTS

1. Introduction 2282
1.1. Benefits of Mixing in Lead Halide Perovskites and Related Compounds 2283
1.2. Mixing Effects in Classical Inorganic Compounds 2285
1.3. Methods to Study Mixing Effects in Lead Halide Perovskites 2285
1.3.1. Diffraction Techniques 2285
1.3.2. Calorimetric Techniques 2286
1.3.3. Spectroscopic Techniques 2286
1.3.4. Computational Techniques 2287
2. Structural Phase Transitions in Nonmixed 3D Lead Halide Perovskites 2287
2.1. **$MAPbI_3$** 2287
2.2. **$MAPbBr_3$** 2288
2.3. **$MAPbCl_3$** 2288
2.4. **$FAPbI_3$** 2288
2.5. **$FAPbBr_3$** 2288
2.6. **$FAPbCl_3$** 2288
2.7. **$CsPbI_3$** 2289
2.8. **$CsPbBr_3$** 2289
2.9. **$CsPbCl_3$** 2289
2.10. **$MHyPbX_3$** 2289
2.11. **$AZRPbX_3$** 2289
3. Structural Phase Transitions in Lead Halide Perovskites Comprising Two Cations 2289
3.1. Ruddlesden−Popper Phases ($n \geq 2$) 2289
3.2. Dion-Jacobson Phases ($n \geq 2$) 2290
3.3. ACI Perovskites 2291
4. A-Site Mixing in 3D Perovskites 2291
4.1. $MA_{1-x}FA_xPbX_3$ 2291
4.1.1. **$MA_{1-x}FA_xPbI_3$** 2291
4.1.2. **$MA_{1-x}FA_xPbBr_3$** 2293
4.2. MA-Based Compounds 2295
4.2.1. **$MA_{1-x}Cs_xPbBr_3$** 2295
4.2.2. **$MA_{1-x}Cs_xPbI_3$** 2295
4.2.3. **$MA_{1-x}DMA_xPbX_3$ (X = I, Br)** 2295
4.2.4. **$MA_{1-x}EA_xPbI_3$** 2297
4.2.5. **$MA_{1-x}GA_xPbI_3$** 2299
4.2.6. **$MA_{1-x-y}GA_xFA_yPbI_3$** 2299
4.3. FA-Based Compounds 2300
4.3.1. **$FA_{1-x}Cs_xPbX_3$ (X = I, Br)** 2300
4.3.2. **$FA_{1-x}GA_xPbI_3$** 2302
4.4. Summary 2302
5. X-Site Mixing in 3D Perovskites 2303
5.1. MA-Based Compounds 2303
5.1.1. **$MAPb(I_{1-x}Br_x)_3$** 2303
5.1.2. **$MAPb(I_{1-x}Cl_x)_3$** 2305
5.1.3. **$MAPb(Br_{1-x}Cl_x)_3$** 2305
5.2. Cs-Based Compounds 2305

Received: July 25, 2023
Revised: December 15, 2023
Accepted: February 9, 2024
Published: February 29, 2024

https://doi.org/10.1021/acs.chemrev.3c00532
Chem. Rev. 2024, 124, 2281−2326

5.2.1. $CsPb(I_{1-x}Br_x)_3$ 2305
5.2.2. $CsPb(Br_{1-x}Cl_x)_3$ 2307
5.3. MHy-Based Compounds 2307
5.3.1. $MHyPb(Br_{1-x}Cl_x)_3$ 2307
5.3.2. $MHyPb(Br_{1-x}I_x)_3$ 2307
5.4. Summary 2307
6. Simultaneous A- and X-Site Mixing in 3D Perovskites 2308
6.1. $FA_{1-x}MA_xPb(I_{1-y}Br_y)_3$ 2308
6.2. $FA_{1-x}Cs_xPb(I_{1-y}Br_y)_3$ 2309
7. B-Site Mixing in 3D Perovskites 2309
7.1. $MAPb_{1-x}Sn_xI_3$ 2309
7.2. $FAPb_{1-x}Sn_xI_3$ 2309
8. Halide, Metal, and Cation (A-, A′-, A″-Site) Mixing in Lower-Dimensional Perovskites and Related Compounds 2310
8.1. $CHA_2Pb(Br_{1-x}I_x)_4$ 2310
8.2. $(C_9H_{19}NH_3)_2PbI_2Br_2$ 2310
8.3. $Br\text{-}PEA_2Pb(Br_xCl_{1-x})_4$ 2310
8.4. $PEA_2Pb(Br_xCl_{1-x})_4$ and $PEA_2Pb(Br_xI_{1-x})_4$ 2310
8.5. $HA_2Pb(Br_xI_{1-x})_4$ and $HA_2FAPb_2(Br_xI_{1-x})_7$ 2310
8.6. $Et_3PrNPb(Br_{1-x}I_x)_3$ 2310
8.7. $t\text{-}BA_2Pb(Br_{1-x}I_x)_4$ 2310
8.8. $(3AMP)_x(4AMP)_{1-x}(FA)_y(MA)_{1-y}Pb_2Br_7$ 2310
8.9. $(BA_{0.5}PEA_{0.5})_2MAPb_2Br_7$ 2311
8.10. $[AA_xIdPA_{1-x}]_2MA_{n-1}Pb_nI_{3n+1}$ (n = 2−4) 2311
8.11. $(BA)_2(MA_{1-x}EA_x)_2Pb_3I_{10}$ 2311
8.12. $(PEA)_2(MA_{1-x}GA_x)_2Pb_3I_{10}$ 2311
8.13. $(BA)_2(MA_{1-x}Cs_x)Pb_2Br_7$ 2311
8.14. $PEA_2Pb_{1-x}Sn_xBr_4$ 2311
9. Conclusions and Outlook 2311
Author Information 2313
Corresponding Author 2313
Authors 2313
Notes 2313
Biographies 2313
Acknowledgments 2313
Abbreviations 2313
References 2314

1. INTRODUCTION

In the past decade, lead halide perovskites $APbX_3$ (A = molecular or inorganic cation, X = halide anion) and related materials have received unprecedented attention due to their potential applications for photovoltaic devices such as efficient solar cells and light-emitting diodes (LEDs).[1−7] The power conversion efficiency of solar cells based on these solution-processable compounds experienced an extraordinary boost and currently exceeds 25%,[8,9] with the best performance and stability achieved using perovskites with mixed compositions.[10,11]

Depending on the type and relative size of the constituent ions, lead halide perovskites can form either three-dimensional (3D) or lower-dimensional structures.[12,13] The stability of the 3D perovskite structure is determined by the tolerance factor first introduced by Goldschmidt for inorganic oxides[14] and later modified for organic−inorganic perovskites by introduction of the effective ionic radius r_{eff} of the molecular cations.[15,16] This semiempirical approach is based on the assumption of rotational freedom of the molecular cations around their center of mass and work surprisingly well for organic−inorganic perovskites, thus confirming the highly dynamical nature of the these cations within the perovskite cavities. The anisotropic size of the molecular cations, together with the number and the type of hydrogen donors for N−H···X hydrogen bonding, are important in shaping the distortions of the ordered or partially ordered low-temperature phases.[17] When the tolerance factor falls in the range of 0.9 to 1.0, 3D perovskites of cubic symmetry are formed, while a tolerance factor of 0.80 to 0.89 typically leads to lower symmetry. Low-dimensional structures typically emerge, when the tolerance factor is higher than 1 or lower than 0.7.

The low-dimensional lead halides can crystallize in several stoichiometries and can be regarded as two-, one-, or zero-dimensional (2D, 1D, and 0D) structures. The 2D hybrid organic−inorganic lead halides are derived from 3D perovskites by removing inorganic layers along the (100), (110), or (111) directions, and the most common stoichiometry is $A'_2A_{n-1}Pb_nX_{3n+1}$ or $A''A_{n-1}Pb_nX_{3n+1}$, where A, A′, and A″ are a small monovalent, large monovalent and large divalent cation, respectively.[18] 1D structures have various stoichiometries, and they contain chains composed of corner-, edge-, or face-shared PbX_6 octahedra separated by organic cations.[19] 0D structures also have various stoichiometries, for instance, A_4PbX_6, and they consist of completely isolated PbX_6 octahedra or lead halide clusters.[20,21] In most cases, the isolation is achieved by employment of large organic cations. As discussed by Akkerman and Manna, these types of lead halides, especially 1D and 0D, have little in common with the 3D perovskite structure, and therefore they should not be identified as perovskites.[22] However, the term "perovskite" for these low-dimensional structures has been widely accepted in the literature, and in this review we will call such structures perovskites.

The 3D structures of lead halide perovskites have a typical $APbX_3$ topology, where the A-site cation is enclosed in an inorganic lead-halide cage formed out of the corner-sharing PbX_6 octahedra (Figure 1a). Currently, there are five known A-site cations (methylammonium (MA), formamidinium (FA), methylhydrazinium (MHy), aziridinium (AZR), and Cs^+), which stabilize the 3D perovskite structure (Table 1). Among these, hybrid organic−inorganic $MAPbI_3$ and $FAPbI_3$, and all-inorganic $CsPbX_3$ perovskites are the most promising for solar cell and related applications.[8,9]

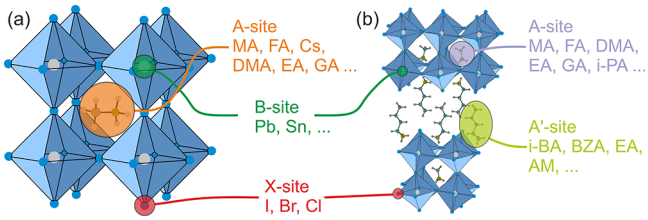

Figure 1. Mixing in the (a) 3D and (b) lower-dimensional (Ruddlesden−Popper) lead halide perovskites.

Mixing in 3D perovskites can be performed in all three sites of the lattice (Figure 1a),[10,11] although the B-site (metal) mixing is significantly less frequent. The choice of organic and inorganic cations for the A-site mixing is rather broad with the most popular cations listed in Table 1 together with their corresponding effective ionic radii, tolerance factors, and dipole moments. The mixing ingredients at the X-site are limited to I^-, Br^-, and Cl^- anions, which have different ionic radii and affinities to form H-bonds with the molecular cations.

https://doi.org/10.1021/acs.chemrev.3c00532
Chem. Rev. 2024, 124, 2281−2326

Table 1. The Most Popular A-site Cations Used for Mixing and Formation of 3D Lead Halide Perovskites[a]

A-site cation	r_{eff} (pm)	tolerance factor	dipole moment (D)
Methylammonium (MA) $CH_3NH_3^+$	217	0.91	2.26
Hydrazinium (HY) $H_3N\text{-}NH_2^+$	217	0.91	3.24
Formamidinium (FA) $HC(NH_2)_2^+$	253	0.99	0.22
Imidazolium (IM) $C_3N_2H_5^+$	258	1.00	1.42
Methylhydrazinium (MHy) $CH_3NH_2NH_2^+$	264	1.01	2.80
Dimethylammonium (DMA) $(CH_3)_2NH_2^+$	272	1.03	1.52
Ethylammonium (EA) $(C_2H_5)NH_3^+$	274	1.03	3.95
Acetamidinium (ACE) $H_3C(NH_2)_2^+$	277	1.04	1.33
Guanidinium (GA) $C(NH_2)_3^+$	278	1.04	0
Cs^+	167	0.81	-
Rb^+	152	0.78	-

[a]The effective cation radius r_{eff} and the tolerance factor (in the lead iodide framework) were calculated by following the procedure described in ref 15. The electric dipole moment was calculated for the isolated cation using DFT (B3LYP/6-31G*).

Upon mixing with high amounts of large molecular cations, the 3D perovskite structure becomes unstable due to the increase of the tolerance factor.[15,16] In this limit, typically a phase separation occurs in the 3D perovskite and low-dimensional perovskite-like structures. Currently, the low-dimensional perovskites are widely applied in fabrication of solar cells,[23−25] LEDs,[4−7,19,25−28] photodetectors,[26,29] piezoelectric sensors,[26,30] scintillators,[19,31] nonlinear optical (NLO) switches,[32,33] and dielectric switches.[34,35] These compounds occur in various topologies comprising one or two organic cations, where examples of the former compounds are $A_2'PbX_4$ and $A''PbX_4$ layered perovskites (A′ = monovalent cation, A″ = divalent cation).[36−41] There are many reports on the formation of lead halide perovskites comprising two organic cations. One of these groups constitutes an alternating cation in the interlayer space (ACI) perovskites with the general formula $A'A''_nPb_nX_{3n+1}$ ($n \geq 1$).[42−44] Another and very large group constitutes quasi-layered Dion-Jacobson (DJ, $A''A_{n-1}Pb_nX_{3n+1}$) and Ruddlesden−Popper (RP, $A'_2A_{n-1}Pb_nX_{3n+1}$) phases with $n \geq 2$, where A, A′, and A″ is a small "perovskitizer" cation, large spacer monovalent cation. and large spacer divalent cation, respectively (Figure 1b).[23,45−47] Most of the small cations are the same as those used in the synthesis of pure and mixed-cation 3D perovskites, e.g., MA, FA, DMA, GA, etc., but the relaxed tolerance factor in such low-dimensional perovskites also allows the incorporation of larger cations such as isopropylammonium (i-PA) and 1,2,4-triazolium (TZ) into the perovskite cavities.[48,49]

There are numerous studies and reviews on the mixing effects on the photovoltaic performance, optical properties, and stability of lead halide perovskites (see e.g. refs 11, 50−52). However, despite these properties highly depending on the atomistic picture of the mixed compositions,[53−57] a systematic understanding of how mixing affects the structural and dynamics phenomena in these materials is still lacking. This is especially important in the context of classical inorganic perovskites, where mixing is known to drastically alter the long-range order and lattice dynamics, causing formation of exotic frustrated phases such as relaxors and electric dipole glasses.[58−62]

The main goal of this review is to provide the first comprehensive and systematic understanding and highlight common aspects of mixing effects on the structural and dynamic properties of lead halide perovskites. The introductory section of the review is structured to briefly cover the most important photovoltaic aspects of mixing followed by a brief summary of ion substitution effects in classical inorganic compounds and the most common tools employed to study the structural and dynamic properties of mixed lead halide perovskites. The subsequent sections provide an in-depth analysis of the structural phase transitions in nonmixed parent compounds forming a basis for the subsequent chapters, which deal with the A-, X-, and B-site mixing in 3D perovskites. Afterward, the mixing effects in the low-dimensional lead halide systems are discussed. The review ends with the generalization of the common aspects observed in different mixed systems followed by an outlook, which draws a roadmap for further studies of these intricate systems.

1.1. Benefits of Mixing in Lead Halide Perovskites and Related Compounds

It is well-known that one of the main limiting factors of the most popular 3D perovskites $MAPbI_3$ and $FAPbI_3$ is their low chemical stability in a humid environment and under exposure to light as well as low thermal stability. One of the main strategies to increase stability is the A-site mixing with larger organic cations like GA, DMA, IM, EA, HY, ACE, hydroxyethylammonium (HEA), or thioethylammonium (TEA)[63−74] (see Table 1 for the most popular A-site cations). For instance, mixing of $MAPbI_3$ with 5% of GA led to a 62% decrease in the degradation rate under illumination.[63] Another very important benefit of mixing at the A-sites is a better photovoltaic,[63−67,69−71,75−80] photodetecting,[68,73,74,81] and photoluminescence (PL) performance[63] as well as tunability of the NLO properties.[82] For example, mixing of $MAPbI_3$ with GA increased PL lifetimes and enhanced efficiency of solar cell devices.[63]

There are numerous experimental and theoretical reports showing that the A-site mixing affects the electronic structure including band gap and electron−phonon coupling.[69,80,81,83−87] Studies of $MA_{1-x}Cs_xPbI_3$ and $FA_{1-x}Cs_xPbI_3$ showed that the band gap gradually increased with increasing Cs content, and this effect was attributed to shortening of the Pb−I bond lengths, when the larger MA cation is replaced by the smaller Cs^+.[83,87] Mixing of $MAPbX_3$ compounds with larger cations also revealed a gradual increase of the band gap with increasing level of mixing. For instance, in the $MA_{1-x}DMA_xPbBr_3$ solid solution, the band gap showed a change from 2.17 eV for $x = 0$ to 2.23 eV for $x = 0.3$,[86] while in the $MA_{1-x}GA_xPbI_3$ system the change was from 1.49 eV ($x = 0$) to 1.53 eV $x = 0.22$.[80] This behavior was attributed to local distortions of the inorganic sublattice, especially alteration of the X−Pb−X bond angles mediated by the new H-bonds.[69,84] Computations performed for the $MA_{1-x}DMA_xPbI_3$ and $MA_{1-x}GA_xPbI_3$ solid solutions suggested that the A-site mixing effectively suppressed the strength of the electron−phonon coupling and that this effect is stronger for the GA-based system.[81] It was suggested that the reduced strength of the electron−phonon coupling may also contribute to the longer carrier lifetimes in the mixed perovskite.[81] Latter temperature-dependent studies of the PL properties of $MA_{1-x}FA_xPbI_3$ solid

https://doi.org/10.1021/acs.chemrev.3c00532
Chem. Rev. 2024, 124, 2281−2326

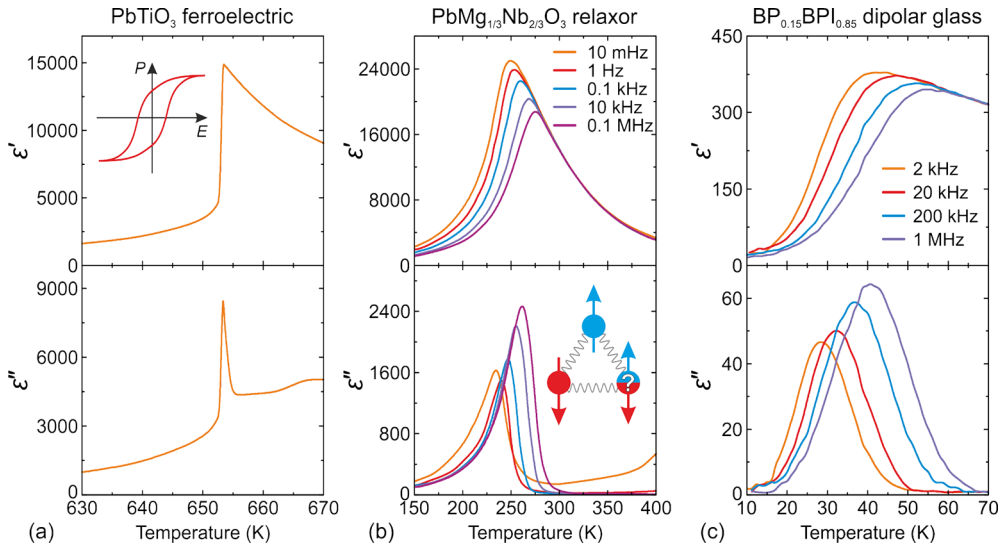

Figure 2. Temperature dependence of the complex dielectric permittivity of (a) $PbTiO_3$ perovskite ferroelectric, (b) canonical relaxor $PbMg_{1/3}Nb_{2/3}O_3$, and (c) dipolar glass $(betaine{-}phosphate)_{0.15}(betaine{-}phosphite)_{0.85}$. A typical ferroelectric hysteresis loop is presented in the inset in (a). Inset in (b) shows a classical example of dipole frustration in the antiferrommagnetic Ising model on a 2D triangular lattice. (a) Adapted with permission from ref 154. Copyright 1971 Taylor & Francis. (b) Adapted with permission from ref 62. Copyright 2006 Springer Nature. (c) Adapted with permission from ref 153. Copyright 1996 IOP Publishing.

solutions showed that, while the effective phonon energy is almost independent of the FA content with an average value of about 5 meV, the electron−phonon coupling strength adopts two different values: about 10 meV for the end members and about 17 meV for the intermediate compositions.[88] Thus, for this system the mixing led to the increase of the electron−phonon coupling.

Improved photovoltaic performance, stability, and tunability of PL color and intensity can also be realized by doping at the B-sites with Sn^{2+}[71,89−97] or other metal cations.[98−101] The improved properties after mixing at the B-site have been attributed to change of the band gap, decrease of the electron−phonon coupling strength, increase in the material defect formation energy, and increased charge carrier lifetimes due to changes in the cation dynamics.[67,84,89,91,93−97,102] It is worth adding that band gaps of tin-based perovskites are narrower compared to lead-based analogues. Consequently, for many B-site mixed perovskites comprising divalent lead and tin, for instance $CsPb_{1-x}Sn_xBr_3$ and $FA_{0.75}Cs_{0.25}Pb_{1-x}Sn_xI_3$, the band gap exhibits gradual narrowing with increasing Sn content.[103,104] Interestingly, in some cases, the mixed lead−tin perovskites possess narrower band gaps compared to the end members, making these mixed system very attractive for photovoltaic applications. This behavior (band gap bowing) was reported for $MAPb_{1-x}Sn_xI_3$ and $FAPb_{1-x}Sn_xI_3$ solid solutions, for which the intermediate compounds showed corresponding band gaps of 1.17 eV and near 1.3 eV, whereas the band gap of $MAPbI_3$, $MASnI_3$, $FAPbI_3$, and $FASnI_3$ was 1.55, 1.30, 1.55, and 1.39 eV, respectively.[89,94] It was argued that this anomalous behavior emerges from the nonlinear mixing of Pb and Sn orbitals in the band edges.[105] In addition to tuning of the optoelectronic properties, the B-site doping is also highly desirable due to high lead toxicity.[94,98]

It is important to note that, although the photoactive black phases of $FAPbI_3$ and $CsPbI_3$ have great application potential, they are thermodynamically unstable and transform into the nonphotoactive yellow phases in an ambient humid atmosphere.[106,107] The black phases can be stabilized by preparing FA/Cs, FA/MA, or FA/Rb solid solutions,[76,108−110] by mixing $FAPbI_3$ with large organic cations,[72,79] or by mixing both the A- and X-sites.[95,111−115] In the latter case, Br^- anions are usually used at the X-sites.[111−113] Mixing at this site is also widely used to tune optical band gaps and improve photovoltaic properties.[9,116−118] The effect of the halide exchange on the band gap is much more pronounced compared to the A- or B-site mixing. In general, the band gap in Br/Cl and Br/I systems strongly narrows with increasing Br and I content, respectively, due to the increased Pb−X bond length.[85,119] As a result, the PL color is altered from UV for chlorides to near-IR for iodides.[9,116−119] Mixing at the X-site also tunes the NLO and dielectric properties.[118,120,121]

Another very important aspect of mixing in $MAPbI_3$ is the lattice symmetrization and cubic phase stabilization achieved by suppression of the structural phase transitions. In addition to lower defect density, longer carrier lifetime, larger wide absorbance range, and enhanced stability,[68,78,122] stabilization of the cubic phase below room temperature is desirable, as it prevents the phase-transition-induced accumulation of the lattice fatigue and strain, which are harmful for device operation.[123]

In the case of lower-dimensional perovskites, a partial mixing was reported only at the B- and X-sites and mainly for the A'_2PbX_4 and $A''PbX_4$ layered perovskites. Similarly to the 3D analogues, the mixing at the X-sites strongly modifies the band gap, and therefore this mixing was chosen as a strategy to tune the PL color and to obtain materials exhibiting white-light emission.[36−41] The X-site mixing may also lead to tunable dielectric properties.[124] Mixing at the B-site is less common, but it was shown that substitution of lead with tin narrows the band gap and induces broadband PL.[125−127] Replacing of lead with other metal cations like Mn^{2+} or Sb^{3+} is also a way to tailor the color and PL quantum yield.[128,129] Although partial mixing at the A′- and A″-sites of A'_2PbX_4 and $A''PbX_4$ perovskites (RP and DJ phases with $n = 1$) has not been reported, there are many reports on the formation of lead

https://doi.org/10.1021/acs.chemrev.3c00532
Chem. Rev. 2024, 124, 2281−2326

halide perovskites comprising two organic cations. For the ACI perovskites, employment of two different organic cations offers a potential way to tailor the spin-based and PL properties.[42−44] Employment of two organic cations in the DJ and RP phases has many benefits. First of all, it allows controlling the optoelectronic and PL properties,[23,46,47] but it may also induce other functional responses like ferroelectricity,[130−132] antiferroelectricity,[133] pyroelectricity,[134] or NLO properties.[133,135] Properties of DJ and RP phases with $n \geq 2$ can be further fine-tuned by mixing at the A′-,[136,137] A″-,[138,139] A-,[138,140,141] and B-sites.[142,143] Although many works reported preparation of these phases with different halide anions,[144] recent studies showed that this is not a real mixing since halide anions preferentially occupy different sites.[145]

Despite a vast number of works concentrating on the exploitation of the discussed improvements for device fabrication, mixing effects on the structural and dynamic properties of lead halide perovskites are significantly less studied and understood. It is reasonable to assume that mixing in these compounds would result in a similar behavior as observed in classical inorganic solid solutions, where the substitution effects are significantly better comprehended.

1.2. Mixing Effects in Classical Inorganic Compounds

It is well established that compositional disorder may significantly change the structural and dynamic properties of classical inorganic ferroelectrics and related materials.[58−62] A ferroelectric compound exhibits spontaneous electric polarization, which can be flipped (switched) by the external electric field, as evident from a ferroelectric hysteresis loop measurements (see inset in Figure 2a). Typically, these compounds also exhibit structural phase transitions from the paraelectric (disordered in order−disorder ferroelectrics) to the ferroelectric (ordered) state with changing temperature or pressure.[146]

In some of ferroelectric and related compounds, ion substitution introduces competing interactions, which cause a complete suppression of the structural phase transitions and frustration of electric dipoles or orientational degrees of freedom (inset in Figure 2b). As a result, the long-range dipole order is replaced by the frustrated phases such as dipolar or orientational glass (e.g., $(KBr)_{1-x}(KCN)_x$),[59−61,147,148] strain glass (e.g., $Ti_{50-x}Ni_{50+x}$),[149] or relaxor (e.g., $PbMg_{1/3}Nb_{2/3}O_3$).[58,62,150,151] The dipolar glass phase does not exhibit structural phase transitions and instead is characterized by freezing of electric dipoles at low temperature into structures, which lack long-range order.[59] The relaxors also do not show structural phase transitions, though they are more related to ferroelectrics, as in relaxor compounds, the electric polarization may be induced by application of a sufficiently strong external electric field.[62] The relaxor phenomena occurs due to random charge or bond disorder in the system, which also leads to formation of polar nanoregions, which grow and freeze with decreasing temperature, as confirmed by neutron diffraction.[152]

The frustration of electric dipoles in mixed compounds can significantly alter their dielectric response, which is typically described by the complex dielectric permittivity $\varepsilon^* = \varepsilon' - i\varepsilon''$. Here, the real part ε' corresponds to the dielectric permittivity (dielectric constant), while the dielectric losses (dissipation) are described by the imaginary part ε''. The dielectric response associated with dipolar glass and relaxor phases is usually very broad with respect to both probing frequency and temperature,[58,60] which is caused by a broad distribution of the dipolar relaxation times. This behavior is in sharp contrast to compounds exhibiting structural phase transitions, which are typically accompanied by sharp anomalies in the material properties (Figure 2a). The temperature dependence of ε^* for a canonical relaxor $PbMg_{1/3}Nb_{2/3}O_3$ (PMN) is presented in Figure 2b, showing a highly frequency-dependent peak in both real ε' and imaginary ε'' parts of the dielectric permittivity.[62] As the frequency decreases, the ε' peak becomes higher, and its position shifts toward a lower temperature. This dispersion of the dielectric permittivity covers a very wide range of frequency from mHz to GHz.[58] A dielectric response of a typical dipolar glass $(betaine−phosphate)_{0.15}(betaine−phosphite)_{0.85}$ ($BP_{0.15}PBI_{0.85}$) is presented in Figure 2c also exhibiting a broad dispersion of ε^* with a less pronounced maximum of ε'.[153] Note that the dielectric responses of ferroelectrics, relaxors, and dipolar glasses exhibit the Curie−Weiss law ($\varepsilon' \sim 1/T$) at high temperatures away from the anomalies.[62,153] Hence, to distinguish these compounds, the temperature-dependent dielectric measurements in a wide range of temperature and probing frequency are essential.

Another signature of dipolar glass and relaxor phases is divergence of the dipolar relaxation time due to freezing of electric dipoles or dipolar clusters. In such a case, the dipolar dynamics are described by the Vogel−Fulcher law[60,62,155,156] instead of the typical Arrhenius behavior. In addition, due to the frustrated nature, these phases exhibit higher entropy at low temperature, which results in excess heat capacity C_p best visible as a maximum in the C_p/T^3 representation.[148,157] In analogy with the classical inorganic compounds, similar substitution effects can be expected in the mixed lead halide perovskites and related compounds.

In addition to the fundamental interest, the frustrated phases of classical inorganic compounds have a wide range of applications.[58] For example, due to large value, slow variation with temperature, and low-loss dielectric permittivity, relaxors are used as dielectric media in ceramic capacitors and tunable microwave devices.[158] Some solid solutions of relaxors with ferroelectrics also exhibit a very large electromechanical coupling and piezoelectric response making them widely applicable in piezoelectric devices in transducers and actuators.[159] Some relaxor materials also exhibit a large electrocaloric effect that is promising for novel cooling applications.[160]

1.3. Methods to Study Mixing Effects in Lead Halide Perovskites

Here, we briefly discuss the main techniques used to study how mixing affects the structural properties and dynamics of lead halide perovskites and related compounds. Some of these techniques are summarized in detail in our recent review on molecular spectroscopy of hybrid perovskites.[161]

1.3.1. Diffraction Techniques. The conventional diffraction-based methods provide information on the long-range crystal structure, evolution of the crystal symmetry, and lattice parameters upon temperature change and mixing and thus are essential for construction of the concentration−temperature phase diagrams (see e.g. refs 162−166). The presence of complex twinning in the low-temperature phases of lead halide perovskites makes it challenging to analyze partially or completely overlapped patterns obtained from single-crystal X-ray diffraction (SCXRD) methods, resulting in a multi-domain diffraction. Furthermore, both single-crystal and

https://doi.org/10.1021/acs.chemrev.3c00532
Chem. Rev. 2024, 124, 2281−2326

powder XRD (PXRD) intensities are primarily dominated by the anionic sublattice due to the large scattering factors of lead and halide atoms in comparison to carbon and nitrogen, which makes it difficult to determine the positions of organic cations. Moreover, even in the case of pure lead halide perovskites, both methods frequently lack the requisite sensitivity to identify subtle changes in crystal symmetry, leading to a narrow separation of the diffracted peaks. The introduction of mixing introduces an additional layer of complexity. Therefore, significantly more advanced diffraction techniques that rely on highly monochromatic, bright synchrotron, and neutron radiation sources are often utilized to obtain the structural information.[74,167−172]

In general, disordered systems pose a significant challenge to crystal structure solution.[173,174] In mixed organic−inorganic materials, frustration can affect either the molecular or inorganic sublattices or both. The organic components in lead halide hybrids are anisotropic and display strong temperature-dependent dynamics. Additionally, they tend to be anchored in the inorganic framework through H-bond interactions at low temperatures experiencing off-center displacements. In these instances, the ordering of the molecular part induces distortion in the inorganic component. Similarly to dipolar glasses, the freezing of molecular motions can result in the random distribution of molecular dipole moments. It may also lead to correlated arrangements and formation of ordered nanodomains, which are somewhat similar to the relaxor behavior. Thus, another important aspect of structural analysis of hybrid lead halide perovskites concerns local order and short-range interactions.

The XRD methods that rely on the periodicity of the structure give only the time-averaged positions of molecular cations and inorganic framework over the measured sample volume. The elastic scattering results in sharp Bragg peaks, whereas static or dynamic deviations from the average long-range structure manifest as additional intensities in-between or around the main peaks and are called diffuse scattering. The diffuse scattering may originate both from static local atomic correlations or from dynamic displacements due to the lattice dynamics (thermal diffuse scattering). Insight into short-range interactions and local structural distortions can be probed via total X-ray scattering, which has recently become more viable due to the advancement of high-flux, single-crystal X-ray diffuse scattering, synchrotron wide-angle X-ray total scattering, and neutron diffuse scattering from single crystals and powders.[175−177]

The importance of the advanced scattering techniques is evident from the recent diffuse scattering experiments probing short-range order in the average high-temperature cubic phase of $MAPbI_3$, where the local structure was found to be of lower symmetry.[178] Dynamical instabilities in $MAPbI_3$ were also evidenced by high energy resolution inelastic X-ray (HERIX) scattering,[179] while total X-ray scattering revealed dynamic nanodomains of noncentrosymmetric local structure. In $CsPbI_3$ nanoparticles, the combined Debye scattering equation and pair distribution function approach based on total X-ray scattering evidenced the formation of orthorhombic subdomains in the room- and high-temperature phases,[180] whereas two-dimensional dynamical correlations in real space arising from the peculiar $CsPbBr_3$ lattice dynamics were found in the high temperature cubic structure of bulk single crystals.[181]

1.3.2. Calorimetric Techniques. Calorimetric methods such as differential scanning calorimetry (DSC) and heat capacity C_p measurements are frequently employed to detect the thermodynamic anomalies occurring due to the structural phase transitions in pure and mixed lead halide perovskites.[164−166,182−186] These experiments also yield the entropy change associated with the phase transition, which is used to characterize the degree of ordering and character (order−disorder, displacive) of the transition. In addition, the low-temperature C_p measurements of the mixed compounds may provide information on the higher entropy states originating from the dipolar glass or relaxor phase, as revealed in the C_p/T^3 representation.[148,157,163,164]

1.3.3. Spectroscopic Techniques. Various spectroscopic techniques probing vastly different time scales can be employed to study the dynamics and structural properties of mixed lead halide perovskites.[161]

The broadband dielectric spectroscopy (DS) is a method of choice to study the dynamics and ordering of electric dipoles, phase transitions, and correlated ordered (e.g., ferroelectric) and disordered (dipolar glass) phases.[59,62,148,150] These phenomena are typically imprinted in the measured frequency and temperature responses of the complex dielectric permittivity $\varepsilon^* = \varepsilon' - i\varepsilon''$ of the studied material (see e.g. Figure 2). The strength of the DS stems from the ability to probe various processes, which involve change of electric polarization. These include charge transport and accumulation, polar (e.g., ferroelectric) domain dynamics, molecular rotation, dipole relaxation, lattice (phonon) dynamics, and electronic polarization.[187] As these processes occur on vastly different time scales ranging from minutes to fs, the DS experiments typically require measurements using a broad range of probing frequency of the applied electric field. In a typical frequency spectrum for a dipolar relaxation, the real value of ε^* exhibits a decrease, while the imaginary part shows a peak, as the probing frequency crosses the frequency associated with the studied dipolar dynamics.

To probe different dipolar processes occurring in lead halide perovskites, ultra broadband dielectric experiments extending to the GHz frequency range may be necessary because of the fast reorientation of organic cations on the ns and ps time scales. This poses significant experimental challenges, as simple capacitor-type measurements are no longer suitable, and instead conceptually different and more complicated coaxial and waveguide setups must be employed.[188,189] In addition to the information on the phase transitions and dipole dynamics, the DS provides the dielectric permittivity value, which directly affects the exciton binding energy and consequently the performance of the photovoltaic devices.[53,55,56,183,190−192]

Raman and infrared (IR) spectroscopy is another versatile tool well-suited for investigation of the mixing effect in lead halide perovskites and related compounds.[69,88,118,165,193] These techniques can probe the local molecular environment, degree of disorder, symmetry, molecular vibrations, and lattice phonons,[194−199] all of which to some extent can be affected by mixing.[69,88,118,165,193,200] IR spectroscopy can also provide information on the frequency-dependent dielectric permittivity, electron−phonon coupling strength, and polaron masses.[196,201] The temperature-dependent Raman and IR measurements of the molecular cation and lattice modes typically are highly sensitive to the structural phase transitions,[88,165,185,194−199,202] complementing other techniques for construction of the phase diagrams.

Nuclear magnetic resonance (NMR) is another well-established spectroscopic technique used to probe the

https://doi.org/10.1021/acs.chemrev.3c00532
Chem. Rev. 2024, 124, 2281−2326

dynamics and phase transition in (mixed) lead halide perovskites and related compounds.[75,102,172,203−206] It is also frequently employed to determine the stoichiometry and solubility limits of the mixed compounds.[166,207,208] The basis of this method relies on the nuclear Zeeman interaction, which results in a splitting of the nuclear spin energy levels in the external magnetic field. The splitting is also affected by the local nuclear spin environment, which may reflect the local symmetry and degree of disorder introduced by mixing. Information about the molecular cation dynamics on a time scale ranging from ps to hours can be obtained from the spectra of the quadrupolar nuclei and relaxation time measurements.[102,204,209,210] A related technique used to study mixing effects in lead halide perovskites is a nuclear quadrupole resonance, which is performed in the absence of the external magnetic field.[172,203] These experiments probe the interaction of the electric field gradient with the nuclear quadrupole moment, which is very sensitivity to the changes of the local symmetry and environment of the studied nucleus, providing information on the local dynamics and structural phase transitions.

Molecular dynamics can be also studied using a quasielastic neutron scattering (QENS) technique. QENS is a limiting case of inelastic neutron scattering, in which broadening of the elastic line is due to a small energy transfer between the neutron and the atoms in the sample. QENS probes the energetically broadened signal around the elastic line and measures energy transfer down to the sub-μeV regime. This allows access to low energy collective motions, diffusional motions, relaxation processes, and molecular reorientations.[211,212] Thus, QENS is often used to provide information about the dynamics (vibrational, rotational, and translational diffusive processes at the molecular scale) on time scales from ps to μs and on length scales from 1 to 500 Å.[211−213] This technique finds application in many scientific topics, including polymers, dynamics of proteins, hydrogen dynamics, etc.[211,212] QENS proved to be a very powerful method to determine the modes, characteristic correlation times, and activation energies of the molecular cation motion in lead halide perovskites.[213−217]

1.3.4. Computational Techniques. Computational techniques such as the density functional theory (DFT), Monte Carlo (MC), and molecular dynamics (MD) simulations provide information on the microscopic origins of the molecular cation and lattice dynamics, structural phase transitions, and mixing effects.[218] The DFT calculations can yield the atomistic picture of the ordered phases[164,166,219−221] but are constrained to small system sizes and poor ability to probe entropic effects. The temperature effects and dynamics can be probed using MD,[222−226] but such simulations may also suffer from the pronounced finite-size effects, especially if *ab initio* MD is used. The MC simulations are capable of simulating large many-particle systems and temperature effects, but usually the atomistic picture must be simplified to a coarse-grained model based on the effective model Hamiltonian formalism.[164,213,227−229] Recently, significant attention was also concentrated on the machine-learning-augmented calculations, which are capable of predicting new structures, phase transitions, and properties of (mixed) lead halide perovskites, while overcoming the need for large-scale simulations.[205,206,230−237]

2. STRUCTURAL PHASE TRANSITIONS IN NONMIXED 3D LEAD HALIDE PEROVSKITES

Here, we discuss the structural phase transitions and phase symmetries of $MAPbX_3$, $FAPbX_3$, $CsPbX_3$, and $MHyPbX_3$ lead halide perovskites forming 3D structures. The commonly accepted phase diagrams of these compounds are summarized in Figure 3.

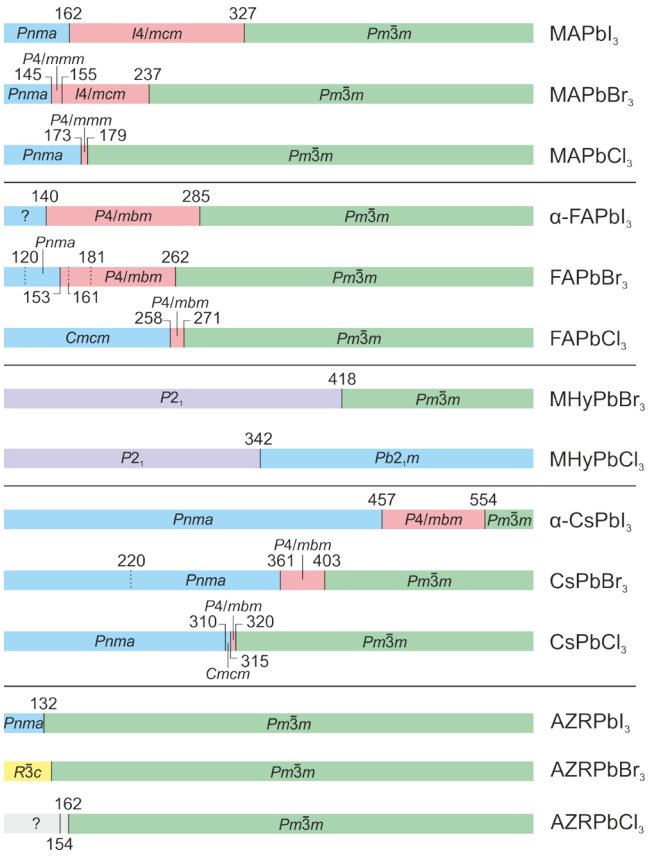

Figure 3. Summary of the structural phase transitions and symmetries of different 3D lead halide perovskites. Color coding: green - cubic, pink - tetragonal, blue - orthorhombic, yellow - trigonal, violet - monoclinic, gray - unknown.

2.1. $MAPbI_3$

$MAPbI_3$ exhibits two structural phase transitions at 327 and 162 K associated with the symmetry lowering from the cubic ($Pm\bar{3}m$) phase to tetragonal and orthorhombic symmetries. The former transition is similar to inorganic $SrTiO_3$[238] and is being driven by out of phase octahedral rotation around the cubic *c*-axis (Glazer notation:[239] $a^0a^0c^-$) followed by a partial MA cation ordering and transformation of the unit cell to body centered **b** − **a**, **a** + **b**, 2**c** superstructure. The second phase transition results in a complete ordering and orthorhombic phase with more complex tilting and distortion of the PbI_6 octahedra. Consensus has been reached in the literature regarding the change of the crystallographic system of $MAPbI_3$, yet the assignment of the tetragonal and orthorhombic space group remains a topic of debate. Initially, the orthorhombic phase was modeled in the $Pna2_1$ polar space group based on low-temperature Guinier data.[240] However, more recent powder neutron diffraction experiments have led to its reclassification to centrosymmetric *Pnma*.[167,241] Similarly, the

https://doi.org/10.1021/acs.chemrev.3c00532
Chem. Rev. 2024, 124, 2281−2326

tetragonal phase was originally discovered in the polar *I*4*cm* space group[93] and later recalculated in the centrosymmetric *I*4/*mcm* space group.[242,243] The commonly accepted centrosymmetric models of the room-temperature tetragonal and low-temperature orthorhombic phases have been called into question by numerous studies claiming ferroelectric behavior of $MAPbI_3$,[53,244−248] although no solid proof of ferroelectricity (and thus absence of centrosymmetry) was observed. Contrary, many studies claim nonferroelectric ordering in this compound,[183,227,249−252] supporting the centrosymmetric symmetry.

Several studies also revealed the presence of octahedral rotational instabilities in the cubic phase of $MAPbI_3$, which correlate with the MA cation motion and cause a local dynamic symmetry breaking.[178,179,253−258] Beecher et al.[179] estimated that the phonon lifetimes associated with such instabilities is on the ps time scale, and the size of such correlated domains is a few nm. Recently, Weadock et al.[178] observed that such local structures are two-dimensional circular regions of dynamically tilted PbI_6 octahedra that induce longer-range intermolecular MA correlations. Such lattice fluctuations cannot be observed using standard XRD techniques, which are sensitive to long-range order and thus provide an averaged-out cubic symmetry. The presence of such low-symmetry correlated octahedral distortions on the nanoscale may be related to the observed transient ferroelectric-like effects in this compound.[245−248] Note, however, that such a dynamic picture of the tetragonal domains in the cubic phase of $MAPbI_3$ was questioned in a high-resolution neutron inelastic scattering study, which instead found that the phonon scattering is consistent with the central peak phenomenon observed in classical inorganic perovskites.[259]

2.2. $MAPbBr_3$

The bromide analogue $MAPbBr_3$ exhibits an even more intricate phase situation than $MAPbI_3$. Poglitsch and Weber[240] reported four different phases, starting from the cubic $Pm\bar{3}m$, tetragonal, *I*4/*mcm*, at 234 K, tetragonal, *P*4/*mmm*, at 155 K and finally orthorhombic with polar $Pna2_1$ space group below 145 K. This sequence was further confirmed by the heat capacity studies.[182] Other studies have suggested an incommensurate intermediate phase between the tetragonal and orthorhombic structures,[260] or that only two phase transitions occur, with a phase sequence of $Pm\bar{3}m$ - *I*4/*mcm* - *Pnma* analogous to $MAPbI_3$.[168] The assignment of the centrosymmetric space groups is supported by the absence of a clear proof of ferroelectricity in this compound.

2.3. $MAPbCl_3$

Hybrid $MAPbCl_3$ also displays a diverse range of phase transitions. At room temperature, as iodide and bromide analogues, it adopts a simple cubic $Pm\bar{3}m$ structure, which transforms into a tetragonally distorted unit cell of *P*4/*mmm* symmetry, which exists within a narrow temperature range between 173 and 179 K. Below 173 K, the orthorhombic phase is stabilized. The $P222_1$ space group was proposed for this phase, with a doubled *c* lattice parameter,[240] while a $P2_12_12_1$ symmetry was observed in a 2**a**, 2**b**, 2**c** modulated superstructure in ref 261. More recently, the *Pnma* space group was reported based on the synchrotron radiation data indicating heavily distorted $PbCl_6$ octahedra.[262] The low-temperature structure of $MAPbCl_3$ appears to adopt the $a^0b^+c^-$ tilt system.

2.4. $FAPbI_3$

An even more complex behavior of the structural phase transitions is observed in the FA-based hybrid perovskites. In contrast to $MAPbI_3$, the $FAPbI_3$ system crystallizes in the hexagonal photoinactive yellow phase (δ-$FAPbI_3$), which can be transformed into the desirable metastable photoactive black phase (α-$FAPbI_3$) by thermal annealing above 150° C.[222,263] When growing from solution media, the black phase is favored above 60 °C.[93] Chen et al.[264] showed that the black to yellow phase transition is a thermally activated process between the two structures separated by an energy barrier. As a result, after quenching from 400 to 200 K over 80 min, $FAPbI_3$ was kinetically trapped in the black cubic phase and remained in this phase upon further cooling to low temperatures. Neutron and X-ray powder diffraction experiments[265] conducted on both N-deuterated and hydrogenous α-$FAPbI_3$ revealed that this material exhibits two phase transitions. At 285 K, the systems undergo a phase transition from the cubic ($Pm\bar{3}m$) to the intermediate tetragonal centrosymmetric β-phase with a primitive tetragonal **b** − **a**, **a** + **b**, **c** unit cell, characterized by in-phase rotations ($a^0a^0c^+$) similar to those found in $NaTaO_3$ at high temperature.[266] Below 140 K, a low-temperature tetragonal γ-phase of polar *P*4*bm* symmetry was claimed. SCXRD confirmed the *P*4/*mbm* tetragonal symmetry of the β-phase at 200 K.[267] The γ-phase was also reported to have the tetragonal *P*4/*mbm* space group similar to the β-phase—on the grounds of the high-resolution synchrotron diffraction data, testifying the isostructural phase transition from the β- to γ-phase.[268] Recent neutron powder diffraction experiments[222] have indicated that the γ-phase is locally disordered and that there is no long-range ordering of the FA cations. The disordered γ-phase is characterized by the geometrical frustration of the molecule-cage interaction, which seems to cause a glassy behavior at low temperatures.[209]

2.5. $FAPbBr_3$

The bromide analogue $FAPbBr_3$ exhibits less complex phase behavior with the high-temperature cubic $Pm\bar{3}m$ (above 262 K), intermediate tetragonal *P*4/*mbm* and low-temperature orthorhombic *Pnma* structure (below 153 K) determined through combined neutron powder diffraction and synchrotron X-ray diffraction.[269] These phase transitions are associated with partial and complete ordering of FA cations, which introduce lattice deformations. In addition, three additional isosymmetric phase transitions, which are not resolved crystallographically, were also observed in this system at 182, 162, and 118 K.[165,270] According to QENS and Raman scattering, the isosymmetric phase transitions relate to changes in the FA cation dynamics, which may affect the optoelectronic properties of this material.[270,271] Note that isosymmetric transitions are also observed in $CsPbBr_3$[191] and $GAPbI_3$,[272] while in $MAPbBr_3$ it can be induced by applied pressure.[273]

2.6. $FAPbCl_3$

The $FAPbCl_3$ analogue has two first-order phase transitions at about 258 and 271 K. The first transition is associated with the cubic ($Pm\bar{3}m$) to tetragonal symmetry lowering, while the low temperature phase was solved in the orthorhombic centrosymmetric *Cmcm* symmetry based on SCXRD data.[274] The recent neutron diffraction studies show that in the low-temperature orthorhombic phase, FA cations undergo a 2-fold jump reorientation about the C−H axis, which changes to an

https://doi.org/10.1021/acs.chemrev.3c00532
Chem. Rev. 2024, 124, 2281−2326

isotropic rotation in the higher temperature tetragonal and cubic phases.[275]

2.7. $CsPbI_3$

The first reports on $CsPbI_3$ crystal structure appeared in the late fifties;[276] however, the complete picture on the temperature phase behavior of $CsPbI_3$ has been documented quite recently by synchrotron powder diffraction.[277,278] The results are consistent with the formation of two low-temperature phases related to the high-temperature cubic aristo phase of α-$CsPbI_3$ ($Pm\bar{3}m$). The first transition to a primitive tetragonal cell of $P4/mbm$ occurs at about 554 K. On further cooling below 457 K, the orthorhombic $CsPbI_3$ phase of *Pnma* symmetry is stabilized. The crystal structure of $CsPbI_3$ has been also reported in refs 180, 279−281. It is noteworthy that the photoactive black phase of $CsPbI_3$ is formed at high temperature through the reconstructive phase transition from a nonperovskite yellow δ-phase, which takes place slightly above 300 °C.[276] The reconversion of the black phase to the initial yellow phase is catalyzed by humidity, and therefore, when the black phase is not exposed to humidity, it remains stable at room temperature for a matter of weeks, while in a humid environment, it transforms to the yellow phase within minutes.[107]

Similarly to hybrid lead halide perovskites, multiple studies have found that inorganic $CsPbX_3$ perovskites also exhibit short-ranged dynamic fluctuations of the PbI_6 octahedra showing that this behavior is intrinsic to the general lead-halide perovskite structure and not unique to the dipolar organic cation.[181,257,258,282] Lanigan-Atkins et al.[181] found that such correlated dynamics occur over a ps time scale and involve liquid-like damping of low-energy Br-dominated phonons, which correspond to 2D sheets of correlated octahedral rotations. In addition, a recent study[283] revealed that the transformation from the yellow to the black phase of $CsPbI_3$ is driven by the harmonic phonon entropy contribution to the Gibbs free energy, which is substantially higher in the softer black phase of $CsPbI_3$ compared to the stiffer yellow phase. The difference in the vibrational entropy arises from the differently stacked configurations of PbI_6 octahedra in both phases, which permit larger amplitudes of atomic vibrations in the black phase. Note that similar entropy arguments were used to explain the yellow to black phase transformation in the hybrid $FAPbI_3$ system.[264]

2.8. $CsPbBr_3$

A similar phase transition pathway is present in $CsPbBr_3$, where the cubic aristo phase initially distorts to the tetragonal phase at 403 K, followed by a further symmetry decrease to the orthorhombic phase at 361 K.[276,284−288]

2.9. $CsPbCl_3$

$CsPbCl_3$ also has the cubic perovskite structure above 320 K[289] and undergoes three successive phase transitions in a narrow, 10 K, temperature range.[290] The prototypic $Pm\bar{3}m$ phase I transforms at 320 K to the tetragonal phase II ($P4/mbm$) and further at 315 and 311 K to the orthorhombic phases III (*Cmcm*) and IV (*Pnma*).[291−293] The crystal structure of the *Pnma* phase has been confirmed among others by synchrotron powder diffraction[288,294] and SCXRD at 200 MPa.[295] It is worth adding that, contrary to $CsPbCl_3$, the corresponding tin analogue $CsSnCl_3$ can be trapped in the high-temperature cubic phase at room temperature by heating the sample to 100 °C and avoiding exposure to humidity.[296,297]

2.10. $MHyPbX_3$

In contrast to lead halides templated by MA and FA cations, perovskites based on MHy crystallize into well-ordered, low-symmetry structures. $MHyPbBr_3$, for instance, adopts the polar monoclinic $P2_1$ space group, which transforms to a disordered cubic structure ($Pm\bar{3}m$) above 418 K.[185] Similarly, the chloride analogue crystallizes in the same monoclinic $P2_1$ symmetry, which evolves to the orthorhombic polar structure, $Pb2_1m$, at 342 K.[184] Notably, the high-temperature phase is still ordered, and the contribution to spontaneous polarization from MHy dipoles is even larger than at room temperature, leading to stronger second-harmonic generation (SHG) in the high-temperature phase. It is worth highlighting that the MHy-based 3D perovskite structures have a tolerance factor greater than 1. This unique feature results from a significant distortion of the PbX_6 octahedra by MHy, which enters the coordination sphere of lead and forms Pb−N covalent coordinate bonds. Note, however, that despite possessing a similar tolerance factor, no one has succeeded in growing a 3D $MHyPbI_3$ analogue to date.

2.11. $AZRPbX_3$

Recently, the family of 3D hybrid perovskites expanded, as new members based on cyclic aziridinium cations were synthesized.[298] Similarly to MA and FA analogues, it was found that $AZRPbX_3$ compounds exhibit a cubic $Pm\bar{3}m$ symmetry at room temperature. A subsequent phase transition study reported by us[237] revealed that $AZRPbI_3$ exhibits a single structural phase transition at 132 K to orthorhombic *Pnma* symmetry similar to the orthorhombic polymorph of $MAPbI_3$. A single phase transition was also observed for $AZRPbBr_3$ at 145 K, but instead of the orthorhombic symmetry, an unusual trigonal $R\bar{3}c$ space group was obtained. The chloride analogue was found to exhibit two closely spaced phase transitions at 162 and 154 K, but the low-temperature symmetries were not determined due to complex twinning of the crystal structure.

3. STRUCTURAL PHASE TRANSITIONS IN LEAD HALIDE PEROVSKITES COMPRISING TWO CATIONS

Here, we briefly discuss the structural phase transitions in pure RP, DJ, and ACI lead halides, which contain only a single cation at the A-, A′-, and A″-sites. In contrast to 3D $APbX_3$ compounds, many of these structures exhibit clear ferroelectric or antiferroelectric ordering evident by the appearance of spontaneous electric polarization.

3.1. Ruddlesden−Popper Phases ($n \geq 2$)

Temperature-dependent structural phase transitions were reported for many RP lead halide phases of the general formula $A'_2A_{n-1}Pb_nX_{3n+1}$. Here, A′ denotes a spacer cation such benzylammonium (BZA), isobutylammonium (i-BA), EA, amylammonium (AM), isoamylammonium (i-AM), propylammonium (PA), isopropylammonium (i-PA), 3-bromopropylammonium (BPA), 3-chloropropylammonium (CPA), 4-aminomethyl-1-cyclohexanecarboxylate (t-ACH), allylammonium (AA), cyclohexanemethylammonium (MACH), 4-iodobutylammonium (4IBA), and $CH_3(CH_2)_nNH_3^+$ (n = 6, 7, 8, 11, 13, 15, 17), while A is a "perovskitizer" cation such as MA, Cs, FA, EA, DMA, GA, MHy, and FA (Figure 1b).[47,130,133,134,299−302,302−330] In contrast to 3D $APbX_3$ lead halides,[183,227] many of the discovered RP compounds, especially bromides, exhibit ferroelectric or antiferroelectric

https://doi.org/10.1021/acs.chemrev.3c00532
Chem. Rev. 2024, 124, 2281−2326

Table 2. List of Ferroelectric (FE) and Antiferroelectric (AFE) RP Phases

compound	ordering, transition temperature (K)	symmetry change	Reference
$BA_2MAPb_2Br_7$	FE, 352	$Cmc2_1 \rightarrow Cmca$	300
$BA_2MA_2Pb_3Br_{10}$	FE, 315	$Cmc2_1 \rightarrow Cmca$	303
$BA_2FAPb_2Br_7$	FE, 322	$Cmc2_1 \rightarrow Cmcm$	301
$BA_2FAPb_2I_7$	FE, 304	$Fmm2 \rightarrow I4/mmm$	314
$BA_2CsPb_2Br_7$	FE, 412	$Cmc2_1 \rightarrow Cmca$	331
$BA_2EA_2Pb_3Br_{10}$	FE, 380	$Cmc2_1 \rightarrow I4/mmm$	305
$BA_2EA_2Pb_3I_{10}$	AFE, 363; FE, 322	$Cmc2_1 \rightarrow Pbca \rightarrow I4/mmm$	133, 134
i-$BA_2CsPb_2Br_7$	AFE, 353	$Pmnb \rightarrow Cmca$	304
i-$BA_2EAPb_2Br_7$	FE, 326	$Cc \rightarrow I4/mmm$	313
i-$BA_2EA_2Pb_3Br_{10}$	FE, 370	$Cmc2_1 \rightarrow I4/mmm$	313
i-$BA_2FAPb_2Br_7$	AFE, 303.2	$Pnma \rightarrow I4/mmm$	315
i-$BA_2MAPb_2Cl_7$	FE, 316	$Fmm2 \rightarrow I4/mmm$	320
$EA_4Pb_3Cl_{10}$	FE, 415	$Cmc2_1 \rightarrow I4/mmm$	310
$EA_4Pb_3Br_{10}$	FE, 384	$C2cb \rightarrow I4/mmm$	306
$EA_2MA_2Pb_3Br_{10}$	FE, 375	$Cmc2_1 \rightarrow I4/mmm$	311
$EA_2MA_2Pb_3Cl_{10}$	FE, 390	$Cmc2_1 \rightarrow I4/mmm$	321
$AM_2CsPb_2Br_7$	FE, 313 and 349	$F222 \rightarrow Cmc2_1 \rightarrow I4/mmm$	322
$AM_2EA_2Pb_3I_{10}$	FE, 361 and 398	$Pmc2_1 \rightarrow Cmce \rightarrow I4/mmm$	330
i-$AM_2CsPb_2Br_7$	FE, 323 and 349	$Cmc2_1 \rightarrow Pbcm \rightarrow I4/mmm$	329
i-$AM_2Cs_3Pb_4Br_{13}$	FE, 351 and 365	$Cmc2_1 \rightarrow I4/m \rightarrow I4/mmm$	326
i-$AM_2EA_2Pb_3Br_{10}$	FE, 371	$Cmc2_1 \rightarrow I4/mmm$	307
i-$AM_2EA_2Pb_3Cl_{10}$	FE, 392	$Fmm2 \rightarrow I4/mmm$	324
-$AM_2EA_2Pb_3I_{10}$	FE, 313; AFE, 340	$Cmc2_1 \rightarrow Pmcn \rightarrow I4/mmm$	309
i-$AM_2MA_2Pb_3Br_{10}$	FE, 305	$Cmc2_1 \rightarrow I4/mmm$	323
i-$AM_2MA_2Pb_3Cl_{10}$	FE, 343 K	$Pmc2_1 \rightarrow I4/mmm$	325
$PA_2FAPb_2Br_7$	FE, 263.3	$Cmc2_1 \rightarrow Cmcm$	130
$BPA_2FAPb_2Br_7$	FE, 348.5	$Cmc2_1 \rightarrow Cmcm$	130
$CPA_2FAPb_2Br_7$	FE, 335 K	$Cmc2_1 \rightarrow Fmmm$	328
t-$ACH_2EA_2Pb_3Br_{10}$	FE, 355 and 380	$Pm \rightarrow Pmmn \rightarrow Pmmn$	308
$AA_2EA_2Pb_3Br_{10}$	FE, 378	$Cmc2_1 \rightarrow I4/mmm$	312
$C6_2Pb_2Br_7$	FE, 248, 306	$? \rightarrow Cc \rightarrow C2/c$	316
$C7_2Pb_2Br_7$	FE, 260	$? \rightarrow Cc$	316
$C7_2Pb_2Br_7$	FE, 261, 275	$? \rightarrow ? \rightarrow Cc$	316

ordering.[130,133,134,300,301,303−316,320−326,328−331] Table 2 lists RP lead halides, for which the ferroelectric or antiferroelectric phase was confirmed by observation of hysteresis loops or a pyrocurrent. The electric dipole order is usually related to ordering of the bulky A′ organic cations[301,313,322,326,329,331] or to the synergic effect of both A′ and A cation ordering and distortion of the framework.[130,133,300,303−312,314,315,320,321,323−325,328,330] As an illustration of this process, we briefly discuss the ferroelectric phase transition in $BA_2MAPb_2Br_7$. Li et al. showed that, above 352 K, this compound crystallizes in the centrosymmetric structure (space group *Cmca*).[300] In this phase, the organic MA and BA cations are highly disordered, which causes cancelation of the molecular dipole moments (Figure 4a). When the temperature decreases, the organic cations order, and the crystal symmetry changes to $Cmc2_1$. The electric polarization appears along the *c*-direction due to a specific reorientation of the organic cations (Figure 4b).[300]

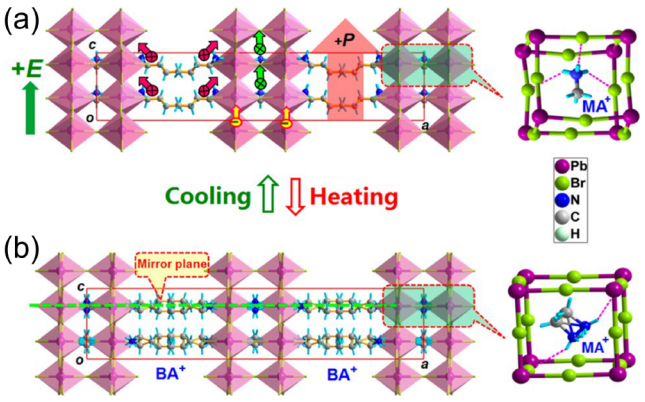

Figure 4. (a) Low-temperature (ferroelectric) structure of $BA_2MAPb_2Br_7$ viewed along the *b*-axis. Red arrow denotes the direction of electric polarization. (b) High-temperature (paraelectric) structure of $BA_2MAPb_2Br_7$. Reprinted with permission from ref 300. Copyright 2019 American Chemical Society.

3.2. Dion-Jacobson Phases ($n \geq 2$)

In contrast to the RP compounds, temperature-dependent structural phase transitions were reported only for two DJ lead halide perovskites: $(AMP)(MA)Pb_2I_7$, (where AMP = 4-(aminomethyl)piperidinium), which undergoes two order−disorder phase transitions at 367 and 449 K,[131] and $(BDA)(EA)Pb_3Br_{10}$ (BDA = 1,4-butyldiammonium), which also shows the presence of two phase transitions at 363 and 397 K.[332] $(AMP)(MA)Pb_2I_7$ exhibits ferroelectric properties, and the polar order is preserved up to the decomposition temperature,[131] while $(BDA)(EA)Pb_3Br_{10}$ undergoes ferroelectric-ferroelectric and ferroelectric-paraelectric phase transitions associated with the $Pmn2_1 \rightarrow Ama2 \rightarrow Cmcm$ symmetry change.[332] Similarly to the RP phases, the electric order in

https://doi.org/10.1021/acs.chemrev.3c00532
Chem. Rev. 2024, 124, 2281−2326

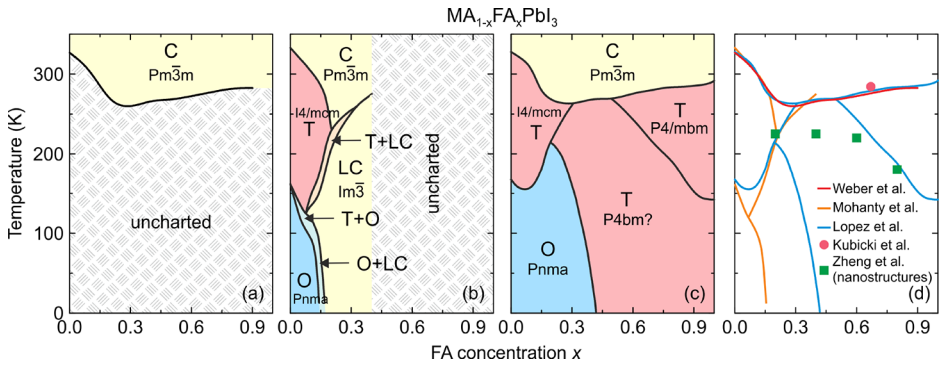

Figure 5. (a–c) Temperature–composition phase diagrams of a mixed $MA_{1-x}FA_xPbI_3$ system obtained in different studies. Symmetry notation: C - cubic, LC - large-cell cubic, T - tetragonal, O - orthorhombic. (a) Adapted with permission from ref 162. Copyright 2016 Royal Society of Chemistry. (b) Adapted with permission from ref 336. Copyright 2019 American Chemical Society. (c) Adapted with permission from ref 88. Copyright 2020 American Chemical Society. (d) Comparison of the phase boundaries presented in (a–c) together with the added data points from refs 102 and 337.

these compounds appears due to the ordering of organic cations.

3.3. ACI Perovskites

In this family of compounds, structural phase transitions were reported for (TR)(GA)$PbBr_4$ ($P2_1/c \rightarrow P2/c$)[44] and (IM)-(MHy)PbX_4 ($P2_1/c \rightarrow P2/c$, X = Br, Cl).[333] In both cases, the phase transitions were found to be of the order–disorder type. However, in the case of (TR)(GA)$PbBr_4$, the change of the space group from $P2/c$ to $P2_1/c$ occurs due to the ordering of the intralayer TR cations, whereas in (IM)(MHy)$PbBr_4$ and (IM)(MHy)$PbCl_4$ both organic cations are disordered in the high-temperature phases and well-ordered at low temperature.

4. A-SITE MIXING IN 3D PEROVSKITES

We now will start discussing the mixing effects in 3D lead halide perovskites by considering the most popular mixing recipe, which involves cation substitution at the A-site. We discuss how this mixing affects the structural and dynamic properties of these materials. The cubic 3D perovskite structure is predicted to be most stable for the tolerance factor close to 1, while for values significantly lower than 1 a lower symmetry can be expected at room temperature. For instance, $MAPbI_3$ with a tolerance factor of 0.912[334] crystallizes in the tetragonal $I4/mcm$ symmetry at room temperature. An effective way to increase the tolerance factor and stabilize the cubic phase is A-site mixing with larger cations. However, the extent of mixing highly depends on the size of the guest cation—a significant mismatch in the cation size results in a solubility limit, beyond which the phase separation typically occurs.

4.1. $MA_{1-x}FA_xPbX_3$

Mixing of MA and FA cations is among the most popular recipes to enhance the performance and stability of lead halide perovskites.[115,335] Similar radii of the cations (217 and 253 pm, Table 1)[15] and the fact that the end members have perovskite architectures result in the 3D perovskite structures for all mixing concentrations of $MA_{1-x}FA_xPbX_3$ (no solubility limit) providing an excellent system for a complete mapping of the phase diagram.

4.1.1. $MA_{1-x}FA_xPbI_3$. The first work studying mixing effects on the phase behavior in the $MA_{1-x}FA_xPbI_3$ system was reported by Weber et al.,[162] where the high-temperature phase transition was investigated using SCXRD and PXRD methods. In the low x region, a substantial lowering of the phase transition temperature was observed upon mixing, reaching a minimum value of about 260 K for $x = 0.3$ (Figure 5a). For higher values of x, the phase transition temperature recovered, as the system evolved from the MA-rich state to the FA-rich composition. The space group of the cubic phase was assigned to $Pm\bar{3}m$, which is in agreement with parent $MAPbI_3$ and α-$FAPbI_3$ compounds (Figure 3), while the XRD data below the phase transition point were indexed using either doubled cubic or tetragonal unit cell.

A following study from the Sarma group[336] reported a detailed XRD characterization and dielectric properties of the $MA_{1-x}FA_xPbI_3$ system in the MA-rich region of the phase diagram ($x \leq 0.4$) and a broad temperature range (Figure 5b). For very low values of mixing ($x < 0.07$), the authors observed a typical cubic-tetragonal-orthorhombic symmetry lowering inherited from $MAPbI_3$ perovskite. The mixing also caused the decrease of the phase transition temperatures compared to the $MAPbI_3$ system in agreement with the aforementioned study by Weber et al.[162] At the intermediate values of the studied compositions ($0.07 < x < 0.2$), the authors claim an observation of a cubic super cell ($Im\bar{3}$ space group) at low temperature instead of the orthorhombic phase, which demonstrated an unusual reentrant cubic-tetragonal-cubic behavior. For $x > 0.2$, the tetragonal phase also becomes completely suppressed at the expense of the growing boundary of this large-cell cubic phase. Eventually, only the transition between the cubic and large-cell cubic phases is observed. The authors also note that the XRD data indicate narrow phase coexistence regions at the phase boundaries as depicted in Figure 5b.

The whole FA concentration range in the $MA_{1-x}FA_xPbI_3$ system was recently explored by Francisco-López et al.[88] using the temperature-dependent Raman and PL spectroscopies. The authors relied on the available structural information on $MAPbI_3$ and α-$FAPbI_3$ perovskites to construct a complete phase diagram of the mixed system (Figure 5c). In the FA-rich region ($x > 0.5$), the authors show the presence of the tetragonal $P4/mbm$ phase inherited from α-$FAPbI_3$. In addition, it is claimed that a tetragonal-tetragonal phase transition exhibits a critical point at $x = 0.7$, as the evolution of the PL peak shows no discontinuity with decreasing temperature. However, this assignment is debatable, as the sharp transition anomaly is expected to become diffused in the highly

https://doi.org/10.1021/acs.chemrev.3c00532
Chem. Rev. 2024, 124, 2281–2326

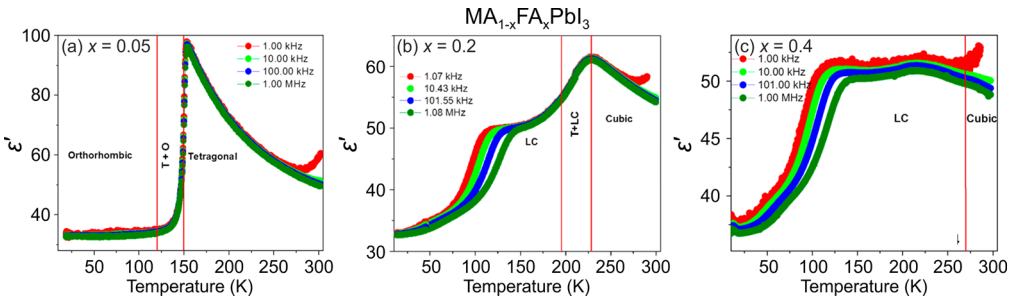

Figure 6. Temperature dependence of the real part of the complex dielectric permittivity ε' of the mixed $MA_{1-x}FA_xPbI_3$ pellet samples for x = (a) 0.05, (b) 0.2, and (c) 0.4. Reprinted with permission from ref 336. Copyright 2019 American Chemical Society.

mixed region. A comparison with the study by Weber et al.[162] reveals an almost identical phase boundary between the cubic and tetragonal phases in the whole range of mixing (summarized in Figure 5d). However, a comparison with the phase diagram provided by the Sarma group[336] shows that the phase boundary of the orthorhombic phase is substantially shifted to higher values of x (Figure 5d). This may suggest different incorporation yields of FA cations in both works, although agreement of the phase boundaries in the high temperature region is satisfactory. No conclusions regarding the discrepancy between the phase symmetries can be made, as no diffraction experiments were performed.

The tuning of the phase transition temperature by mixing was also observed in the nanostructures of $MA_{1-x}FA_xPbI_3$ using temperature-dependent PL measurements.[337] A small disagreement with other studies in transition temperatures can be observed (see Figure 5d), which may originate from a small size of the nanostructures and broadening of the anomalies in the highly mixed region.[338]

Ahmadi et al. used piezoresponse and Kelvin probe force microscopies and SHG to study the long- and short-range electric dipole and charge dynamics in $MA_{0.15}FA_{0.85}PbI_3$ composition.[339] Surprisingly, the authors reported indications of ferroelectric domains in this mixed compound; however, the domain dynamics were found to be suppressed by fast ion motion.

In addition to the structural data, the aforementioned study from the Sarma group[336] reported the temperature dependence of the real part of the complex dielectric permittivity of the $MA_{1-x}FA_xPbI_3$ ($x \leq 0.4$) pellet samples in a narrow frequency range (1 kHz - 1 MHz) (see Figure 6 for selected compositions). As pointed out by the authors, the dielectric response in this mixed system mainly originates from MA cations due to a much lower electric dipole moment of FA (2.3 D vs 0.2 D, Table 1). At a low FA concentration (Figure 6a), the main feature of the dielectric response is a sharp decrease at the tetragonal-orthorhombic phase transition point caused by the MA cation ordering, while the cubic-tetragonal phase transition is poorly visible. This behavior is in a good agreement with a number of previous DS works on pure $MAPbX_3$ perovskites.[183,340,341] Interestingly, the authors claim that the anomaly at higher values of x is related to the transition from the cubic to large-cell cubic phase (Figure 6b). The most intriguing feature of the dielectric response is the broad dipolar relaxation at low temperature, which appears for a higher FA content (Figure 6b,c). This relaxation extends from about 120 to 25 K and is assigned by the authors to the dipolar (orientational) glassy state, which indeed has some similarities with the classical dipolar glasses (see Figure 2c), although broadband DS experiments are necessary to make an unambiguous assignment.

A subsequent study from the same group used QENS experiments to investigate the dipolar glass phase and molecular cation dynamics of the mixed $MA_{0.875}FA_{0.125}PbI_3$ compound in more detail.[217] The temperature-dependent experiments allowed probing the MA and FA cation dynamics in different structural phases including the proposed large-cell cubic phase. The QENS data were best modeled using a 4-fold (C_4) reorientation for the MA cation motion in the tetragonal and cubic phases with the activation energy E_a of 83 meV in a good agreement with 82 meV observed for pure $MAPbI_3$. At a lower temperature, where the 3-fold rotation of MA around the C−N axis dominates, the mixed composition displayed a distribution of activation energies in contrast to pure $MAPbI_3$, which showed E_a = 53 meV. This result further supports the appearance of the dipolar glass phase due to different MA cation environments caused by FA incorporation. Interestingly, the analysis of the elastic incoherent structure factor revealed that FA cations are frozen even up to 340 K, indicating they exhibit a much higher activation energy, and thus the A-site dynamics are governed by MA cations. The fraction of the mobile MA cations was found to be slightly higher in the mixed composition compared to pure $MAPbI_3$, which was explained by an increase of the unit cell volume upon introduction of bigger guest cations. A fractional isotropic rotational model was used to estimate the characteristic time scales of the MA rotation at different temperatures, revealing that MA cation motion is faster in the mixed compound (e.g., 84 ps vs 188 ps at 110 K).

Similar observations and signatures of the orientational glass state were presented by Drużbicki et al.,[225] where higher mixing compositions were investigated (x = 0.6 and 0.9) by the inelastic neutron scattering experiments assisted by the harmonic lattice dynamics and *ab initio* MD simulations. In this study, a highly disordered local environment of MA cations was observed, which was assigned to weakening of the H-bonds and framework expansion induced by mixing. On the other hand, an opposite behavior was found for FA cations, as they form stronger H-bonds with the distorted inorganic cage caused by mixing.

Another interesting NMR and state-of-the-art MD study was reported by Grüninger et al.,[206] where the authors found indications of a clustering of the MA and FA cations within the mixed x = 0.25, 0.5, and 0.75 compounds. Such a local heterogeneous distribution would inevitably cause a local variation of the perovskite lattice and is likely related to the observation of the glassy phase in these compounds.

https://doi.org/10.1021/acs.chemrev.3c00532
Chem. Rev. 2024, 124, 2281−2326

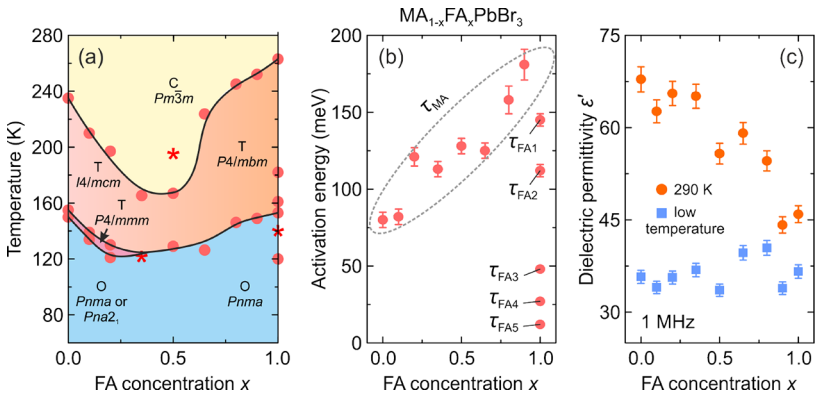

Figure 7. (a) Temperature−composition phase diagram of the mixed $MA_{1-x}FA_xPbBr_3$ system. Symmetry notation: C - cubic, T - tetragonal, O - orthorhombic. The phase boundary between the tetragonal *I*4/*mcm* and *P*4/*mbm* phases is unknown and thus not indicated in the phase diagram. FA concentration dependence of the (b) activation energy of the dipolar relaxations and (c) room-temperature and low-temperature dielectric permittivity (1 MHz). Adapted with permission from ref 165. Copyright 2021 American Chemical Society.

The MA and FA cation dynamics in the mixed deuterated $MA_{0.33}FA_{0.67}PbI_3$ system were investigated by Kubicki et al.[102] using solid-state ^2H and ^{14}N magic angle spinning (MAS) NMR spectroscopy, which allowed a simultaneous probing of both cations. Temperature-dependent measurements of the quadrupolar coupling constants of ^2H and ^{14}N nuclei demonstrated that the reorientation of the C−N bond in MA cations at 327 K is not fully isotropic in the mixed compound, which is in contrast to pure $MAPbI_3$ perovskite. The authors also observed close to isotropic motion of FA cations in the cubic phase. As temperature decreased, this motion slowed down and froze, while a substantial rotation of the N−D_3 and N−D_2 groups around the C−N bonds of FA remained even at 100 K. At room temperature, it was found that FA rotates much faster than MA (12 ps vs 133 ps), which was attributed differences in the H-bond strength between the cations and the framework. The authors also correlated much faster FA rotation to increased charge carrier lifetimes observed in $FAPbI_3$ and mixed $MA_{1-x}FA_xPbI_3$ systems compared to pure $MAPbI_3$.[102] In addition to the cation dynamics, this study also provided the phase transition temperature to the cubic phase of 285 K in a good agreement with other studies (Figure 5d). It is interesting to compare the reported results with the aforementioned QENS study.[217] Both works detected that mixing alters the MA cation motion, while the observations regarding the FA cation dynamics are in sharp contrast, as the Sarma group reported that the rotational dynamics of FA cations are entirely suppressed over the entire temperature range in the $x = 0.125$ compound. The observed differences may be explained by different studied compositions, suggesting that level of mixing can highly influence the FA cation dynamics.

A recent NMR quadrupolar relaxation study[204] from the same group indicated that the FA cation dynamics in the cubic phase of $MA_{0.3}FA_{0.7}PbI_3$ is essentially the same as in $FAPbI_3$ compound and occur on about a 1 ps time scale with activation energy close to 100 meV. On the other hand, the authors reported that the MA cation motion is about 2× faster in the mixed compound compared to $MAPbI_3$ (1.0 ps vs 1.95 ps). Note that the reported cation correlation times are about 1−2 orders of magnitude shorter compared to their previous work,[102] which was explained by difficulties in relating the measured ^{14}N line widths to the motionally induced transverse relaxation, whereas quadrupolar relaxation measurements are much more reliable. Interestingly, the authors observed that the activation energy of the MA cation motion was not affected by mixing and remained close to 150 meV. Note that Fabini et al.[209] also found very similar MA and FA cation rotation rates in nonmixed $MAPbI_3$ and $FAPbI_3$ compounds. The observation of fast FA cation dynamics in the $x = 0.7$ compound is in a sharp contrast to the aforementioned QENS results obtained by the Sarma group,[217] where frozen FA cations were observed for the $x = 0.125$ composition. This discrepancy may originate from vastly different fractions of FA cations in the studied compounds, which belong to the opposite sides of the phase diagram.

4.1.2. $MA_{1-x}FA_xPbBr_3$. Recently, we used a multitechnique approach (DSC, heat capacity, ultrasonic measurements, SCXRD, broadband DS, Raman spectroscopy) to thoroughly investigate the mixing effects on the structural phase transition, dielectric response, and cation dynamics in the bromide analogue of the mixed $MA_{1-x}FA_xPbBr_3$ ($0 \le x \le 1$) system.[165] A suite of different experimental techniques probing structural phase transitions of single crystal samples allowed us to construct the phase diagram for the whole range of FA concentrations (Figure 7a). The obtained phase diagram shows lowering of the phase transition temperatures upon mixing and thus stabilization of the desirable cubic phase.[122] We also observed disappearance of the intermediate tetragonal phase upon mixing in the MA-rich region of the phase diagram. On the other limit of mixing, the three isosymmetric transitions of $FAPbBr_3$[172,270] were also fully suppressed even at the lowest studied MA content, which may paradoxically be related to a relief of the FA cation frustration by mixing (see ref 172 for details).

A comparison of the phase diagrams of the $MA_{1-x}FA_xPbBr_3$ and $MA_{1-x}FA_xPbI_3$ systems shows a qualitative agreement for low values of x (see Figures 5d and Figure 7a). However, the central parts of the diagrams are significantly different, as higher symmetry phases were found at low temperature for the $MA_{1-x}FA_xPbI_3$ perovskites (see Figure 5).[88,336] We note that such differences between both systems are expected due to different phase behaviors of the iodide and bromide parent compounds.

In the same study,[165] we also reported the temperature-dependent broadband DS experiments (Hz-GHz frequency range) of the $MA_{1-x}FA_xPbBr_3$ single crystal samples. The most important results comparing the dielectric responses of the

https://doi.org/10.1021/acs.chemrev.3c00532
Chem. Rev. 2024, 124, 2281−2326

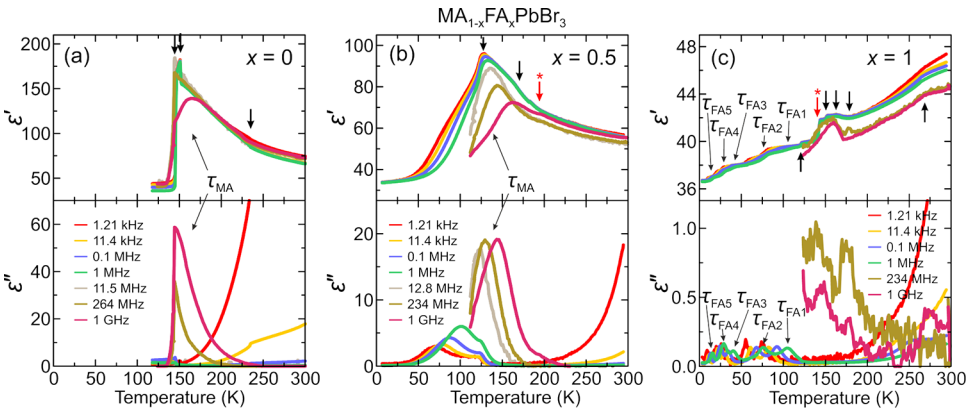

Figure 8. Temperature dependence of the complex dielectric permittivity of (a) $MAPbBr_3$, (b) $MA_{0.5}FA_{0.5}PbBr_3$, and (c) $FAPbBr_3$ single crystals presented at selected frequencies. Arrows indicate phase transition anomalies and dielectric relaxations. Adapted with permission from ref 165. Copyright 2021 American Chemical Society.

parent compounds (x = 0 and 1) and the highest mixing case (x = 0.5) are presented in Figure 8. Similarly to the iodide analogue, the complex dielectric permittivity of $MAPbBr_3$ compound exhibits an anomalous decrease at the tetragonal-orthorhombic phase transition related to the establishment of the long-range MA cation order.[183,340,341] Other phase transitions are visible as small anomalies. On the other end of the composition, the dielectric response of $FAPbBr_3$ perovskite shows several weak anomalies originating from the phase transitions (see phase diagram, Figure 7a).[274] In addition, five distinct and well-resolved dielectric relaxations of unknown origin were identified in the orthorhombic phase (best visible in the ε'' data). Interestingly, these relaxations mimic the behavior of the isosymmetric transitions, as they also disappear upon mixing even for the lowest MA concentration. The most interesting dielectric response was observed for the highly mixed $MA_{0.5}FA_{0.5}PbBr_3$ compound, where both phase transitions (cubic-tetragonal-orthorhombic) were visible as very weak anomalies (Figure 8c). In addition, a broad dielectric dispersion of MA cations reminiscent of a glassy phase was detected at low temperature in agreement with the iodide analogue (compare with Figure 6c). A strong proof of the dipolar glass phase would be observation of the Vogel–Fulcher freezing behavior of the relaxation time associated with the observed dielectric relaxation. However, it was found that the dynamics of this process follows the typical Arrhenius law preventing an unambiguous assignment of the dipolar glass phase.

The broadband DS can directly measure how mixing affects the value of the dielectric permittivity, which is a relevant parameter influencing the performance of photovoltaic devices.[53,55,56,183,190−192] We observed that the MA and FA cation mixing significantly affects the room-temperature dielectric permittivity of the $MA_{1-x}FA_xPbBr_3$ system (Figure 7c), as ε' showed a rather strong decrease with increasing x, which was assigned to the diminishing number of the MA cations.[165] Note that the permittivity value at low temperature was not affected by mixing (Figure 7c), indicating that it is originating from the inorganic part of the lattice. As discussed by Fabini et al.,[342] such a uniform and rather high value of ε' is related to the lattice polarizability invoked by the $6s^2$ lone-pair electrons and associated off-centering of lead ions.

In the same study, we also proved the dynamic effects in the $MA_{1-x}FA_xPbBr_3$ system using the broadband DS.[165] The relaxation times extracted from the dipolar relaxations were approximated using the Arrhenius law providing the activation energy E_a of the MA cation motion. More than a 2-fold increase (from 80 to 180 meV) of the E_a values with increasing x was observed, indicating that FA cations significantly raise the rotation barrier of the MA cations (Figure 7b). The increase of the activation energy with x may seem to be in contradiction with the aforementioned NMR study of the related $MA_{0.22}FA_{0.78}PbI_3$ compound,[204] where practically no change in E_a was observed upon mixing at room temperature. However, one should note that our study probed activation energies at significantly lower temperatures, where molecular cation motion was substantially hindered. Note that the dipolar dynamics observed by the DS can be extrapolated to room temperature, revealing a 2 ps dipolar relaxation time of MA in $MA_{0.2}FA_{0.8}PbBr_3$, which is in a very good agreement with the MA reorientation time of 1 ps obtained in $MA_{0.22}FA_{0.78}PbI_3$ using NMR.[204] Interestingly, the activation energies of the five low-temperature processes of $FAPbBr_3$ showed a very huge spread ranging from 145 to 12 meV (Figure 7b),[165] which may be related to the recently proposed quadrupolar geometric frustration of the FA cations.[270]

The temperature-dependent Raman data reported in the same work[165] provided information on the degree of the molecular cation ordering. For small values of x, the MA cation modes exhibited significant narrowing at the transition to the orthorhombic phase, indicating ordering of the cations. In contrast, no substantial narrowing was observed at the phase transitions points in the highly mixed and FA-rich compositions ($x \geq 0.5$) showing the absence of the MA cation ordering in agreement with the low-temperature dielectric response. For all mixed compounds, the width of the FA band decreased with decreasing temperature, indicating slowing down of the FA cation dynamics.

In a recent study, Kalita et al. investigated structural phase transitions, framework deformation, and dynamic effects in $MAPbBr_3$, $MA_{0.5}FA_{0.5}PbBr_3$, and $FAPbBr_3$ compositions.[343] The heat capacity measurements revealed that the mixed composition exhibits two structural phase transitions at 164 K (cubic-tetragonal) and 128 K (tetragonal-orthorhombic) in a very good agreement with the phase diagram reported in ref 165. Based on the synchrotron XRD measurements, the symmetry of the orthorhombic phase for the x = 0.5 solid solution was assigned to $P4/mbm$. In addition, it was observed that the Pb–Br length increases upon mixing, which was assigned to a larger radius of FA cation. It was also found that

https://doi.org/10.1021/acs.chemrev.3c00532
Chem. Rev. 2024, 124, 2281−2326

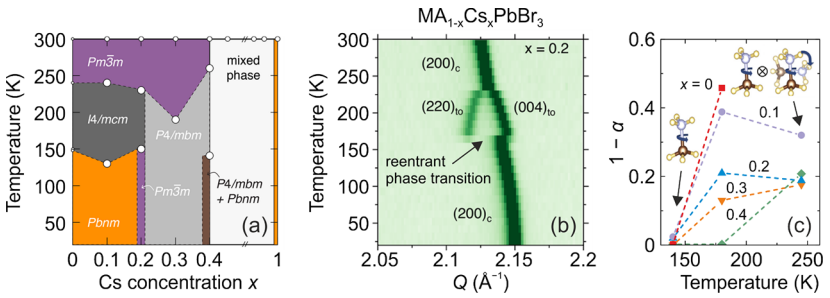

Figure 9. (a) Temperature−composition phase diagram of the mixed $MA_{1-x}Cs_xPbBr_3$ system. Phase separation occurs for $x \geq 0.4$. (b) Neutron powder diffraction data of the $x = 0.2$ composition showing the reentrant phase transition (arrow). (c) Fraction of the MA cations participating in the reorientation around the C_4 symmetry axis (inset) as extracted from the QENS data for different Cs concentrations. Reprinted (adapted) with permission from ref 163. Copyright 2017 American Chemical Society.

the $PbBr_6$ octahedral tilting in the tetragonal phase increases with an increase of x, while the highest distortion of the octahedra in the orthorhombic phase was observed for the $MAPbBr_3$ compound. The temperature-dependent Raman spectroscopy was employed to study the phonon modes in the low-frequency range (50 to 500 cm^{-1}). In agreement with the previous study,[165] it was found that the modes become well resolved in the orhothorhombic phase of $MAPbBr_3$ due to the ordering of the system. In the mixed composition, the low-frequency modes were found to be much broader, indicating disorder compared to $MAPbBr_3$.

4.2. MA-Based Compounds

Here, we review how mixing with less compatible A-site cations affects the phase transitions and dynamic properties of the $MAPbX_3$-based lead halide perovskites. Mixing with such cations results in a solubility limit, beyond which the phase separation (mixed phase) typically occurs.

4.2.1. $MA_{1-x}Cs_xPbBr_3$. Mozur et al.[163] reported a detailed multitechnique investigation of the mixing effects in the $MA_{1-x}Cs_xPbBr_3$ system. The employed advanced synchrotron and neutron diffraction methods allowed them to construct a rich phase diagram of this system (Figure 9a). Interestingly, despite both parent compounds existing in a 3D perovskite form ($MAPbBr_3$ and $CsPbBr_3$), the authors observed a solubility limit of Cs^+ cations in $MAPbBr_3$ ($x \approx 0.4$). This was explained by different octahedral tilting preferences of smaller Cs^+ cations (Table 1).

The authors also found that the $x = 0.1$ composition exhibits the same sequence of the phase transitions (cubic-tetragonal-orthorhombic) as in pure $MAPbBr_3$. The situation is different for $x = 0.2$, where, instead of the tetragonal-orthorhombic transformation, a reentrant transition back to the same $Pm\bar{3}m$ cubic phase was observed (Figure 9b). Such a surprising behavior was explained using the modified Blume−Capel model with included strain coupling. At higher Cs fraction ($x = 0.3$), the system transitioned from the cubic symmetry to the tetragonal $P4/mbm$ phase instead of $I4/mcm$ observed at lower values of mixing. Note that the $P4/mbm$ space group is also observed for pure $CsPbBr_3$ compound (Figure 3), indicating that Cs^+ ions already dictate the octahedral tilt pattern. Interestingly, the transition to the orthorhombic phase was completely suppressed for this Cs concentration. This composition also showed the maximum extent of the cubic phase reaching 200 K. The situation changed again for the $x = 0.4$ composition, where the orthorhombic phase recovered and showed coexistence with the tetragonal phase (Figure 9a).

The same study also used a suite of neutron diffraction and neutron scattering techniques to probe the MA cation arrangement and dynamics for different fractions of mixing.[163] The neutron powder diffraction data demonstrated the absence of the preferred MA cation orientation for all values of x even at low temperature. This was also supported by the inelastic neutron scattering data, which provided evidence of the heterogeneous environments of both the inorganic framework and the MA cations. In addition, the authors observed an excess of low energy modes in the heat capacity data due to the increased disorder. All these findings were attributed to the orientational glass behavior present in both organic and inorganic sublattices and caused by the local-strain induced frustration. The dynamics of the MA cations in $MA_{1-x}Cs_xPbBr_3$ compounds were probed using QENS. The mean squared displacement of hydrogen atoms revealed decreasing amplitude with increasing x and lowering of temperature. This indicated that the motion of MA cations is more hindered in the highly mixed phases. This was also supported by the measurement of the elastic incoherent structure factor, which revealed a drastic decrease in the overall MA cation reorientation around the C_4 symmetry axis upon mixing (Figure 9c). Interestingly, this observation seems to be different than detected in the $MA_{1-x}FA_xPbX_3$ system, where for high levels of mixing the MA cations exhibited substantial dynamics even in the orthorhombic phase as is evident from the dielectric response (Figures 6 and 8).[165,336]

4.2.2. $MA_{1-x}Cs_xPbI_3$. In a recent study, Gallop et al. used XRD, Raman, and 2D IR spectroscopies to investigate the structure and MA cation dynamics of the $MA_{1-x}Cs_xPbI_3$ thin film samples.[344] The authors concentrated on the $x \leq 0.3$ compositions, as for higher Cs fractions signatures of the yellow phase were observed. Note that a similar solubility limit was obtained in the discussed $MA_{1-x}Cs_xPbBr_3$ system.[163] The XRD and Raman experiments indicated shrinkage of the unit cell and a continuous tilting of the octahedral framework upon mixing due to the smaller size of the Cs^+ cation. The 2D IR spectroscopy experiments performed at room temperature revealed that the introduction of Cs^+ makes the MA cation dynamics faster. The characteristic time of the jumping dynamics increased from about 4 ps ($x = 0$) to 12 ps ($x = 0.3$), while the increase of the wobbling dynamics was less pronounced (0.5 ps vs 0.65 ps). The obtained results were correlated with the increased c/a distortion upon mixing, which was also confirmed by the MD simulations.

4.2.3. $MA_{1-x}DMA_xPbX_3$ (X = I, Br). The effective radius of DMA is only slightly larger than that of FA (Table 1), making it a highly promising alternative cation for mixing in lead halide

https://doi.org/10.1021/acs.chemrev.3c00532
Chem. Rev. 2024, 124, 2281−2326

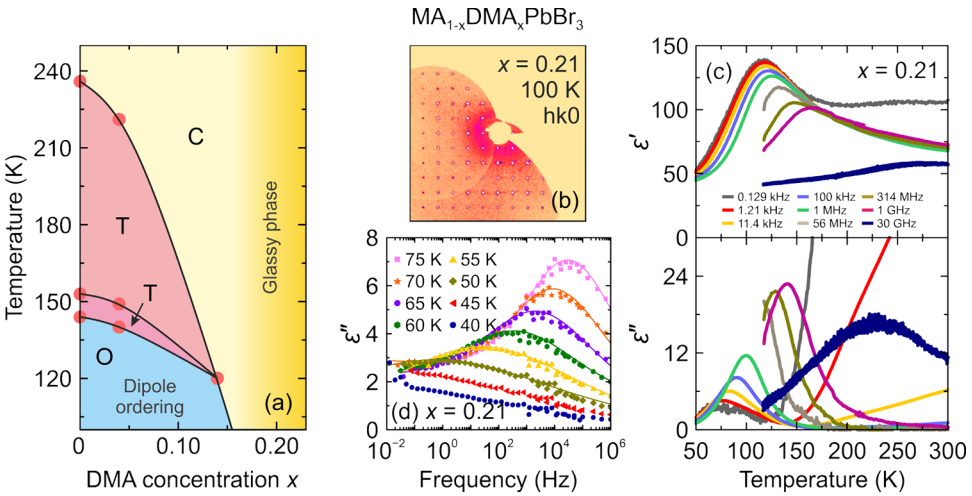

Figure 10. (a) Tentative temperature−composition phase diagram of the mixed $MA_{1-x}DMA_xPbBr_3$ system. Symmetry notation: C - cubic, T - tetragonal, O - orthorhombic. (b) Reciprocal space reconstruction (*hk*0 layer) of the $x = 0.21$ single crystal sample measured at 100 K indicating cubic symmetry. (c) Temperature dependence of the broadband dielectric response of the $x = 0.21$ single crystal sample. (d) Low-frequency dependence of ε'' at selected temperatures of the same sample. Solid curves are the best fits to the Cole−Cole relaxation model. Adapted with permission from ref 164. Copyright 2020 Springer Nature.

perovskites. However, pure $DMAPbX_3$ compounds form hexagonal structures,[345,346] making them only partially compatible with the 3D perovskites.

Shi et al. reported the first study[68] on the DMA incorporation ($x = 0.11$) in $MAPbI_3$. The authors found that mixing with DMA suppresses the tetragonal symmetry by stabilizing the cubic phase at room temperature, which provided a substantial boost in the carrier diffusion length and device stability. A similar work was reported by Shao et al.,[78] where a series of compositions up to $x = 0.25$ were investigated and also linked to the enhanced photovoltaic performance and device stability. A stabilization of the cubic phase at room temperature for DMA concentrations higher than 6% was observed. The authors claimed that the cubic space group of the mixed compounds is noncentrosymmetric $P\bar{4}3m$, which is different from that of pure $MAPbI_3$ (centrosymmetric $Pm\bar{3}m$). The absence of the centrosymmetry was not discussed or proved by the authors, making this assignment questionable. The same work also reported a rather coarse temperature dependence of the PXRD patterns of the $MA_{0.91}DMA_{0.09}PbI_3$ sample showing that the cubic-tetragonal phase transition occurs at about 273 K. Surprisingly, the authors claimed the orthorhombic symmetry already below 233 K, which is a much higher transition temperature compared to pure $MAPbI_3$ (see Figure 3).

Franssen et al.[208] reported a solid-state NMR and PXRD study of the mixed $MA_{1-x}DMA_xPbI_3$ ($x \leq 0.21$) system. The authors obtained that the DMA solubility limit in $MAPbI_3$ is 21%, above which the mixed phase was formed. In agreement with other works, stabilization of the cubic phase at room temperature was also obtained even for small levels of mixing. In addition, the authors performed ^{14}N NMR relaxation experiments of the $x = 0.21$ sample and obtained similar reorientation times for both MA and DMA cations (close to 2 ps) at room temperature. This indicates that despite its bigger size, the DMA cation is still mobile in the mixed structure at room temperature.

The structural phase transitions and cation dynamics in the single crystals of mixed $MA_{1-x}DMA_xPbBr_3$ bromide analogues were investigated by us using a suite of different experimental and theoretical techniques.[164] The incorporated DMA fractions were determined to be 4, 14, and 21% by measuring the atomic C/N ratio. Crystals with higher mixing levels were not synthesized due to the finite DMA solubility limit in $MAPbBr_3$ of about 30% reported by Anelli et al.[86] The phase transition behavior in the mixed compounds was measured using temperature-dependent DSC, ultrasonic propagation, SCXRD, and broadband DS experiments. Upon introduction of a small amount of DMA, the temperatures of all three phase transitions decreased, indicating increased stability of the cubic phase as indicated in the phase diagram of this system (Figure 10a). Such a behavior is in agreement with the results obtained for the iodide analogues.[68,78,208] For the $x = 0.14$ composition, no clear transition anomalies were observed in the DSC, ultrasonic, and DS experiments; however, the SCXRD data indicated a transition below 130 K to a phase having a similar symmetry to the orthorhombic phase observed for the $x = 0$ and 0.04 compositions. No symmetry lowering was observed for the highest mixing level ($x = 0.21$) as evident from the reciprocal space reconstruction (Figure 10b), suggesting a complete suppression of the phase transitions for this DMA concentration.

The same study[164] reported the broadband DS experiments of the $MA_{1-x}DMA_xPbBr_3$ single crystals in a vast frequency range covering more than 11 orders of magnitude in frequency (from mHz to GHz). For small mixing levels ($x = 0.04$), the temperature dependence of the dielectric response was essentially the same as for the $MAPbBr_3$ compound with the tetragonal-orthorhombic phase transition anomaly being the dominant feature. However, a drastically different situation was observed for higher mixings ($x = 0.14$ and 0.21), where the transition anomaly was replaced by a very broad and highly frequency-dependent peak spanning from room temperature to 50 K at microwave and low frequencies, respectively (Figure 10c). The additional low-temperature experiments covering the mHz frequency range revealed very slow dynamics extending to even lower frequencies and temperatures (Figure 10d). These results demonstrated a gradual slowing down of the MA cation dynamics by approximately 12 orders of magnitude and implied formation of a glassy disordered phase

https://doi.org/10.1021/acs.chemrev.3c00532
Chem. Rev. 2024, 124, 2281−2326

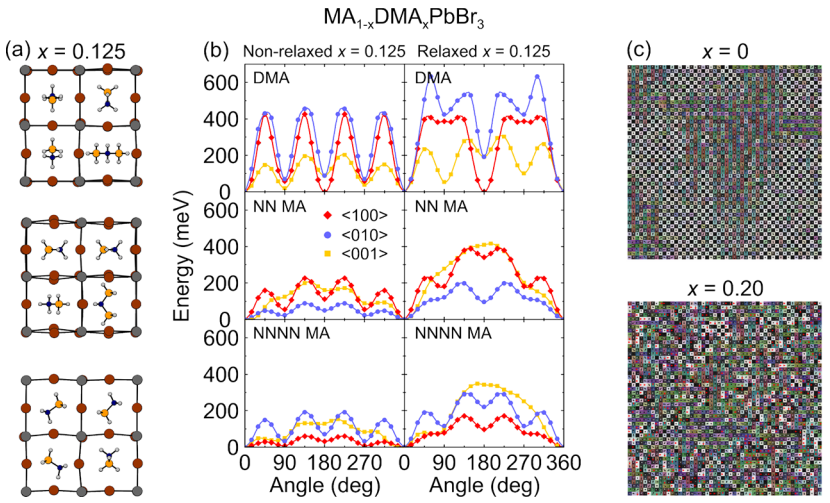

Figure 11. (a) Lowest energy structure of the $x = 0.125$ supercell obtained by DFT calculations, as seen from the <100> (top), <010> (middle), and <001> (bottom) directions. For clarity, only a 2 × 2 × 1 slab containing DMA is presented. (b) DFT calculations of the energy surfaces obtained by rotating DMA and neighboring MA cations around the <100>, < 010>, and <001> directions within the nonrelaxed and relaxed $x = 0.125$ systems. (c) Snapshots of the MC simulations for a two-dimensional slice of a three-dimensional periodic slab representing the $x = 0$ and $x = 0.2$ compositions. The orientations of the MA and DMA dipoles are depicted by gray and red arrowheads, respectively. Reprinted with permission from ref 164. Copyright 2020 Springer Nature.

(compare with Figure 2c). This behavior was also supported by the low-temperature heat capacity measurements, which revealed higher entropy states below 5 K only for the highly mixed compounds. In addition, the activation energy of the MA cation dynamics was determined from the frequency domain data, indicating close to 2-fold increase of E_a from 80 to 140 meV as the DMA content was increased. Note that a very similar behavior was also observed for the already discussed mixed $MA_{1-x}FA_xPbBr_3$ system.[165]

In the same work, we also reported DFT and MC calculations of the mixed compositions supporting the experimental results.[164] The DFT calculations revealed that the DMA cation is situated in the center of the lead−bromine cuboid cavity with two amine protons pointing to the halogens and the C−C bond directed along the <001> (or equivalent) direction (Figure 11a). The same calculations also provided rotation barriers around three orthogonal lattice directions of the DMA and two neighboring (nearest neighbor (NN) and next−next-nearest neighbor (NNNN)) MA cations (Figure 11b). A comparison was made between fully relaxed pseudotetragonal and nonrelaxed cubic (based on pure $MAPbBr_3$, where a single MA was replaced by DMA) structures in order to clarify the effect of DMA incorporation on the neighboring MA cations. The rotation barrier of the DMA cation was found to be significantly higher than that of the MA cations in both structures, indicating that the DMA motion should be significantly hindered. Second, substantially higher rotation potentials of the MA cations were obtained in the relaxed structure demonstrating that the DMA cation perturbs their rotation via the lattice deformation. Third, the energy barrier was found to decrease with increasing distance to the DMA cation reflecting that the lattice deformation is a local effect. Based on these findings, a microscopic picture of the glassy phase formation was proposed, where a random distribution of DMA cations causes different local framework distortions resulting in a multiwell potential for MA cations. This results in cation frustration followed by the glassy phase formation and suppression of the structural phase transitions. Signatures of the orientational glass phase were also obtained using the MC simulations based on the dipole−dipole interaction model developed by the Walsh group.[244] Here, the MA cation (dipole) was allowed to rotate, while the orientation of the DMA dipole was randomly fixed toward a <100> (or equivalent) lattice direction, which should be a valid approximation at low temperature. Despite a simplified nature of this mode, a long-range order emerged for low mixing levels, while no ordering was observed for $x = 0.2$ indicating that the MA dipoles experience severe competing interactions (Figure 11c).[164]

A subsequent study of the mixed $MA_{1-x}DMA_xPbBr_3$ system was published by Ray et al.,[74] where a substantially higher DMA incorporation fraction of 44% (supported by solution ^{1}H NMR) was reported using solvent acidolysis crystallization. The temperature-dependent synchrotron radiation PXRD experiments were performed to study the phase symmetry of the $x = 0.44$ composition. A symmetry lowering from cubic to the tetragonal symmetry was observed at about 205 K, and no orthorhombic phase was recorded down to 80 K. This result is in contrast with the study discussed above,[164] where the cubic phase was maintained at least down to 100 K for the $x = 0.21$ composition (Figure 10a). A likely explanation for this discrepancy is that, in contrast to high-resolution synchrotron PXRD, the conventional SCXRD was not sufficient to resolve small changes associated with this symmetry lowering. Interestingly, the authors claimed that the space group of this tetragonal phase is $P4/mbm$, while pure $MAPbI_3$ shows the $I4/mcm$ symmetry. This transformation was explained by the difference in H-bonding between the molecular cations and the inorganic framework. Note that the identical change of the tetragonal unit cell symmetry upon mixing was observed for the $MA_{1-x}Cs_xPbBr_3$ system (Figure 9a).[163]

4.2.4. $MA_{1-x}EA_xPbI_3$. The ethylammonium cation has an effective radius of 274 pm (Table 1), making it a good candidate for incorporation in lead halide perovskites. Similarly to other big cations, pure $EAPbI_3$ compound does not form a 3D perovskite and instead crystallizes into a 1D topology.[166,347−349]

https://doi.org/10.1021/acs.chemrev.3c00532
Chem. Rev. 2024, 124, 2281−2326

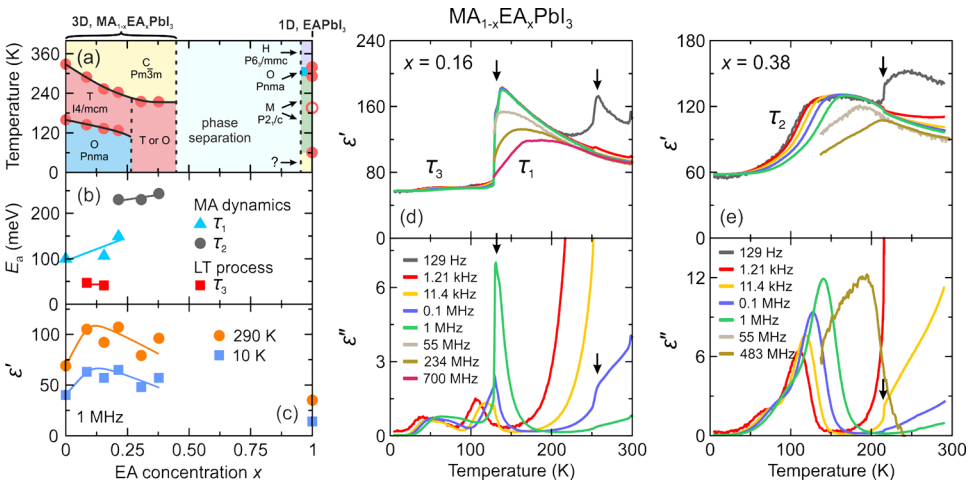

Figure 12. (a) Temperature−composition phase diagram of the mixed $MA_{1-x}EA_xPbI_3$ system. Symmetry notation: C - cubic, T - tetragonal, O - orthorhombic, M - monoclinic, H - hexagonal. EA concentration dependence of the (b) activation energies and (c) ε' (1 MHz) obtained at 290 and 10 K. (d) Temperature dependence of the complex dielectric permittivity of (d) $MA_{0.84}EA_{0.16}PbI_3$ and (e) $MA_{0.62}EA_{0.38}PbI_3$ single crystals presented at selected frequencies. Arrows indicate phase-transition anomalies, while dielectric relaxations are marked by τ_1, τ_2, and τ_3. Reprinted with permission from ref 166. Copyright 2022 American Chemical Society.

Peng et al. reported the first structural study of the mixed $MA_{0.83}EA_{0.17}PbI_3$ system,[350] where the concentration of the incorporated EA cations was determined using the C/N analysis and solution NMR spectroscopy. Using PXRD and SCXRD methods, the authors observed cubic *Pm*$\bar{3}$*m* symmetry at room temperature, indicating that EA cations also stabilize the desirable cubic phase.[122] The temperature-dependent PXRD experiments revealed that the phase transition to the tetragonal phase occurs at about 243 K, which is almost 90 K lower compared to $MAPbI_3$. Stabilization of the cubic symmetry at room temperature was also observed in two other studies[68,351] reporting very similar levels of mixing (x = 0.15 and 0.14). Surprisingly, another study[352] of $MA_{1-x}EA_xPbI_3$ thin films reported a tetragonal symmetry at room temperature up to x = 0.3 EA fraction, above which the phase separation occurred. A DFT study by Liu et al.[84] considered the whole range of mixed compositions (x = 0, 0.25, 0.5, 0.75, and 1) and found almost negligible changes of the Pb−I− Pb bond angles upon mixing with reasonable levels of EA cations ($x \leq 0.5$).

A detailed multitechnique study of the mixing effects on the structural phase transitions, cations dynamics and PL of the $MA_{1-x}EA_xPbI_3$ (x = 0, 0.09, 0.16, 0.21, 0.31, and 0.38) compounds was recently reported by us.[166] The EA concentration was determined using solution ^{1}H NMR spectroscopy, and the solubility limit of about 40% was found. A set of different experimental techniques (DSC, C_p, ultrasonic, SCXRD, broadband DS, and Raman spectroscopy) was used to construct the temperature−composition phase diagram of this system (Figure 12a). For low and intermediate levels of mixing, the temperature of the cubic-tetragonal phase transition significantly decreased with increasing x, indicating stabilization of the cubic phase. For x = 0.16, this transition occurred at 253 K in a good agreement with the temperature of 243 K reported by Peng et al. for the x = 0.17 composition.[350] The temperature of the tetragonal-orthorhombic phase transition also exhibited a decrease with increasing EA content, although the effect was slightly less pronounced (Figure 12a). The situation changed substantially for higher mixing levels (x > 0.3), where this transition became completely suppressed, and the low-temperature phase was described by a primitive tetragonal or pseudotetragonal (with very weak orthorhombic deformation) unit cell. However, due to the pseudomerohedral twinning, a reliable model of this structure was not obtained. The temperature-dependent Raman experiments of this phase revealed a substantial disorder related to the molecular cations even at low temperatures. The phase transitions of the pure 1D $EAPbI_3$ compound were also investigated providing hexagonal-orthorhombic-monoclinic symmetry lowering (also summarized in Figure 12a). Another transition was also observed at an unusually low temperature of 60 K, but the symmetry below this point was not determined.

The broadband DS was employed in the same work[166] to probe the dipolar dynamics of the mixed $MA_{1-x}EA_xPbI_3$ single crystal compounds. For the intermediate values of x, the tetragonal-orthorhombic transition anomaly became broader (Figure 12d) and shifted to a lower temperature. In addition to the expected dipolar relaxation of MA cations in the tetragonal phase (indicated by τ_1 in Figure 12d), an additional dipolar process τ_3 of undetermined origin emerged below 100 K. For x > 0.3, the transition anomaly transformed into a broad dipolar relaxation of MA cations extending to low temperatures (indicated by τ_2 in Figure 12e). The activation energies of both processes associated with the MA dynamics increased with increasing level of mixing (Figure 12b). Note that this effect was also observed in the $MA_{1-x}FA_xPbBr_3$ and $MA_{1-x}DMA_xPbBr_3$ systems suggesting universal behavior.[164,165] Upon mixing, the dielectric permittivity of the $MA_{1-x}EA_xPbI_3$ compounds also exhibited some tuning (Figure 12c), although the effect was rather small likely due to comparable electric dipole moments of both molecular cations (Table 1).

The observed broad dielectric response for the x > 0.3 compositions is similar to other highly mixed compounds (Figures 6, 8, and 10), and, as discussed above, resembles the glassy phase (compare with Figure 2c). However, a clear Vogel−Fulcher behavior of the mean relaxation time was not detected despite broadband measurements (Hz-GHz),[166] indicating that freezing of electric dipoles may occur at very low temperatures. Note that the DFT calculations of the

https://doi.org/10.1021/acs.chemrev.3c00532
Chem. Rev. 2024, 124, 2281−2326

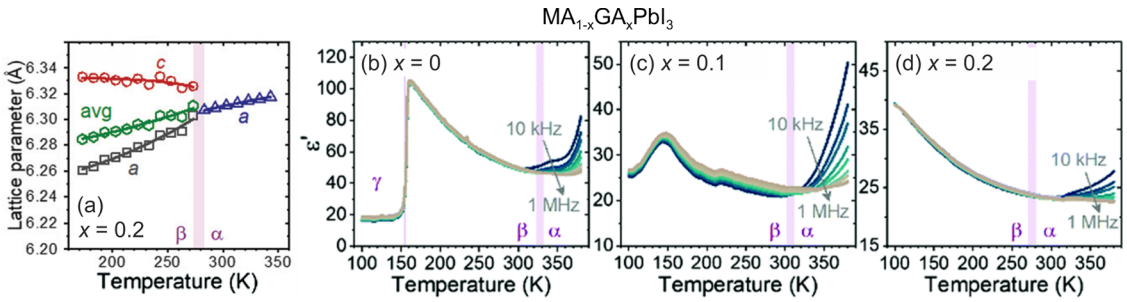

Figure 13. (a) Variation of the lattice parameters with temperature of the $MA_{0.8}GA_{0.2}PbI_3$ system as determined from the XRD data. (b−d) Temperature dependence of the real part of the complex dielectric permittivity ε' of the $MA_{1-x}GA_xPbI_3$ pellet samples at frequencies between 10 kHz and 1 MHz. Reprinted with permission from ref 355. Copyright 2022 Royal Society of Chemistry.

$MA_{0.875}EA_{0.125}PbI_3$ composition revealed about a 20% variation of the rotational barrier for crystallographically different MA cations, indicating that the MA dynamics are affected by the local lattice strains introduced by bigger EA cations.

4.2.5. $MA_{1-x}GA_xPbI_3$. Guanidinium is another highly promising molecular cation used to significantly enhance the performance of the devices based on lead halide perovskites.[69,73,75,75,77,80] The effective radius of this cation is 278 pm, which is practically the same as of DMA and EA (Table 1). For this reason, we may expect similar mixing effects on the structural and dynamic properties of lead halide perovskites.

Several studies reported contrasting solubility limits of these cations in $MAPbI_3$. Jodlowski et al.[69] reported a solubility limit of 25% in the perovskite film samples, and a similar value of 20% was claimed in another study.[353] A significantly higher solubility limit of 40% (based on ^{13}C MAS NMR measurements) was reported by Kubicki et al.[75] for powder samples obtained by mechanosynthesis. Contrary to these studies, Gao et al.[80] measured the solubility limit using NMR to be only 5% in single crystal samples. This result is also in sharp contrast to the solubility limits obtained for other similar size cations such as DMA and EA, prompting further studies to clarify this discrepancy.

Regarding structural properties, several studies reported preservation of the tetragonal symmetry at room temperature in the mixed $MA_{1-x}GA_xPbI_3$ system.[69,73,75,80,353,354] This observation is also in contrast to many other already discussed mixed-cation systems, where stabilization of the cubic phase was observed. Gao et al.[80] observed almost negligible changes of the octahedral tilting and Pb−I−Pb bond lengths and angles for the mixing compositions of $x = 0.05$ and 0.1 showing that these systems remained tetragonal at room temperature. This discrepancy was also recognized and investigated in more detail in a recent study by Minussi et al.,[355] where the phase transition and dielectric properties of the mixed $MA_{1-x}GA_xPbI_3$ ($x = 0$, 0.1, 0.2) system were reported. The authors performed temperature-dependent XRD and DSC experiments, which indeed revealed stabilization of the cubic phase for the $x = 0.2$ compound at room temperature (Figure 13a). This removed the GA cation ambiguity and placed it in the same league with other molecular cations of similar size such as DMA, EA, and FA.

The same work also reported a temperature dependence of the real part of the complex dielectric permittivity ε' of the $MA_{1-x}GA_xPbI_3$ pellet samples in a narrow frequency range (10 kHz - 1 MHz)[355] (Figure 13b−d). The obtained results for pure $MAPbI_3$ compound show an expected anomalous decrease of the permittivity at the tetragonal-orthorhombic phase transition point in agreement with other studies.[183,340,341] For the $x = 0.1$ composition, this anomaly became significantly broader, and its maximum shifted to a slightly lower temperature, suggesting that the stability of the tetragonal phase is also increased. The peak of the anomaly was not detected for the $x = 0.2$ compound likely due to the limited temperature range of the reported experiment. In addition, the authors observed a significant decrease of the dielectric permittivity upon mixing, which can be explained by a negligible electric dipole moment of GA (Table 1).

The dynamics of the molecular cations in the $MA_{1-x}GA_xPbI_3$ solid solutions was investigated by the Emsley group using MAS NMR spectroscopy. Their first study[75] reported the reorientation rates of both molecular cations for the $x = 0.25$ composition by fitting the corresponding ^{14}N NMR spectra. Such an analysis provided 113 ps and less than 18 ps reorientations rates of MA and GA cations at room temperature, respectively. The observed almost 1 order of magnitude faster GA motion was also correlated to a spectacular increase of the charge carrier lifetimes in this mixed compound. However, a recent study from the same group[204] reevaluated these findings using more reliable quadrupolar relaxation measurements, which provided much shorter reorientation times of both cations for the same mixed composition ($x = 0.25$). The MA dynamics perpendicular to the C_3 molecular axis were found to occur on the 1.3 ps time scale with the activation energy of 168 meV at room temperature. A substantially faster rate of 0.3 ps was measured around the C_3 axis with a negligible energy barrier. Note that MA cations in pure $MAPbI_3$ showed very similar reorientation rates, indicating a weak mixing effect on the MA cation motion at room temperature. The dynamics of the GA cation was also characterized by two distinct principal axes owing to its C_3 symmetry. Here, the motion perpendicular to this axis was obtained to be much faster (1.3 ps, $E_a = 121$ meV) compared to the parallel reorientation (14 ps) in line with different moments of inertia.

4.2.6. $MA_{1-x-y}GA_xFA_yPbI_3$. Recently, the Araújo group reported several studies of triple-cation $MA_{1-x-y}GA_xFA_yPbI_3$ solid solutions obtained by mechanosynthesis. In the first work,[356] the authors used PXRD, DSC, and IR spectroscopy to study the structural phase transitions and cation dynamics for the case, where the GA and FA content was equal (i.e., $x = y$) and did not exceed 30% of the total MA substitution. Upon increase of x and y, it was found that the cubic-tetragonal phase transition temperature is substantially lowered to about 270 K at the maximum mixing level ($x = y = 0.15$), indicating increased stability of the cubic phase. The IR spectroscopy

https://doi.org/10.1021/acs.chemrev.3c00532
Chem. Rev. 2024, 124, 2281−2326

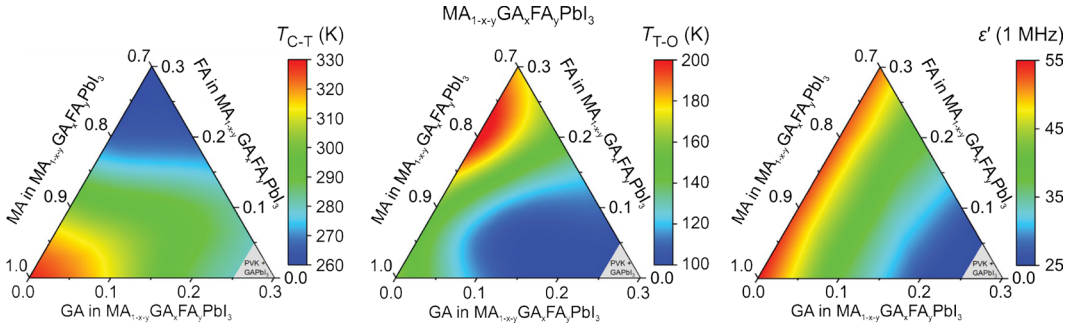

Figure 14. Phase diagrams for the (left) cubic-tetragonal and (middle) tetragonal-orthorhombic phase transitions of the $MA_{1-x-y}GA_xFA_yPbI_3$ system. (Right) Composition map for of the real part of the complex dielectric permittivity ε' obtained at room temperature and 1 MHz probing frequency. Reprinted with permission from ref 357. Copyright 2023 Wiley-VCH.

measurements revealed a gradual shift of the C−N stretching frequency for all organic cations with mixing, which was assigned to the increase of the bond strength. The intensity of the IR bands also exhibited dependence on the mixing level especially when crossing the cubic-tetragonal phase transition. This behavior was related to the degree of cation freedom within differently deformed inorganic framework in the cubic and tetragonal phases.

Subsequent XRD, DSC, and DS studies from the same group[357,358] reported a thorough investigation of the $MA_{1-x-y}GA_xFA_yPbI_3$ solid solutions for $0 \leq x \leq 0.3$ and $0 \leq y \leq 0.3$ with $x + y \leq 0.3$. The reported composition dependence of the cubic-tetragonal phase transition temperature is presented in Figure 14a, revealing that FA cations are more effective in stabilizing the cubic phase compared to GA.[357] Interestingly, the opposite behavior is observed for the tetragonal-orthorhombic phase transition, where the GA-rich compositions have significantly lower transition temperatures (Figure 14b). Both observations clearly indicate that GA cations are more efficient in stabilization of the tetragonal phase compared to FA cations.

In addition to phase transition studies, the same study reported the DS experiments of the $MA_{1-x-y}GA_xFA_yPbI_3$ pellet samples.[357] The measured values of ε' obtained at room temperature and 1 MHz probing frequency are summarized in Figure 14c, indicating that GA incorporation results in a significantly more pronounced drop of the dielectric permittivity compared to FA cations. This result is in agreement with the aforementioned DS studies of the $MA_{1-x}FA_xPbBr_3$[165] and $MA_{1-x}GA_xPbI_3$[355] solid solutions. Such a contrasting FA and GA cation effect on the dielectric response might be related to the absence of the electric dipole moment of GA, although the dipole moment of FA is also almost negligible compared to MA (see Table 1). As also pointed out by the authors, this behavior may also indicate that both cations exert a different hindering effect on the neighboring MA cations. However, this interpretation seems to contradict the recent NMR study by Mishra et al.,[204] where the effect of the incorporated GA and FA cations on the MA cation motion was found to be small in $MA_{1-x}FA_xPbI_3$ and $MA_{1-x}GA_xPbI_3$ compounds, suggesting a more intricate mechanism. We also note that the reported DS experiments were performed on the pressed pellet samples, which always introduces a degree of uncertainty in the determination of the dielectric permittivity.

4.3. FA-Based Compounds

The current best performing hybrid perovskites for photovoltaic applications are based on the mixed compositions with α-$FAPbI_3$.[8,9,11] Despite this significance, the mixing effects on the structural phase transitions and dynamics in these compounds are substantially less investigated compared to the MA-based perovskites. In this section, we review the available studies, which mostly concentrate on mixing with Cs^+ and GA cations, as mixing with MA is covered above. Note that many works report stabilization of the photoactive black α-phase of $FAPbI_3$ upon mixing (e.g., refs 11, 72, 76, 110, 359.). However, the majority of these studies fall out of scope of this review, as they concentrate on utilization of the stabilized α-$FAPbI_3$ phase for device fabrication and provide no or very little additional information about the structural and dynamic effects.

4.3.1. $FA_{1-x}Cs_xPbX_3$ (X = I, Br). Charles et al.[171] used a suite of diffraction techniques (neutron powder diffraction, SCXRD, PXRD) to thoroughly probe the phase transition behavior in the mixed $FA_{1-x}Cs_xPbI_3$ system. A solubility limit of about 15% was determined using PXRD in agreement with the magnetic resonance studies,[207,360] while a substantially higher limit close to 30% was reported for thin films.[95] To avoid phase separation into black and nonperovskite yellow components observed for higher mixing levels, the authors selected $x = 0.1$ concentration for a more detailed investigation. The room-temperature diffraction measurements revealed that the time averaged structure of this compound has a cubic $Pm\bar{3}m$ symmetry in agreement with pure $FAPbI_3$ perovskite (Figure 3). It is also noted that the local structure may contain pseudotetragonal domains due to tilted octahedra switching rapidly between preferred directions. The determined Pb−I−Pb angle in the mixed composition was found to be 162.8°, which is almost identical to the nonmixed $FAPbI_3$ compound (163.7°).[222] Interestingly, upon introduction of Cs^+, the phase transition temperature to the tetragonal $P4/mbm$ phase slightly increased (290 K), which likely occurs due to the significantly higher phase transition temperatures of $CsPbI_3$. Below 180 K, the diffraction data were indexed to either crystallographic twins in the tetragonal space group $P4/mbm$ or orthorhombic $Pnma$. A convergence to the orthorhombic $Pnma$ symmetry was obtained below 125 K with additional weak reflections attributed to glass-like disorder, which was also proposed for pure $FAPbI_3$.[209] The transition temperature to this phase was lowered upon mixing. All these results are summarized in a crude phase diagram presented in Figure 15a. Note that signatures of the glassy

https://doi.org/10.1021/acs.chemrev.3c00532
Chem. Rev. 2024, 124, 2281−2326

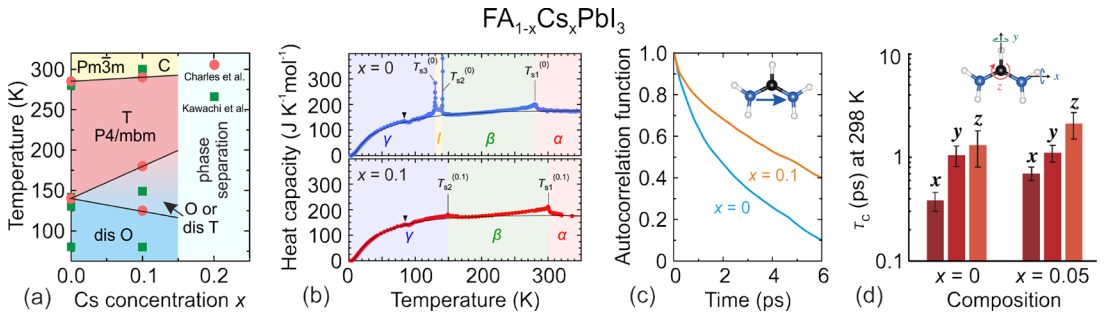

Figure 15. (a) Tentative temperature−composition phase diagram of the mixed $FA_{1-x}Cs_xPbI_3$ system. Symmetry notation: C - cubic, T - tetragonal, O - orthorhombic, disT - disordered tetragonal, disO - disordered orthorhombic. Adapted with permission from ref 171. Copyright 2020 American Chemical Society. (b) Temperature dependence of the heat capacity of the $x = 0$ and $x = 0.1$ compounds. Reprinted with permission from ref 186. Copyright 2019 American Chemical Society. (c) Vector autocorrelation function of FA cation in the $x = 0$ and $x = 0.1$ compositions showing the probability of the cation remaining in its initial orientation over time. Molecular vector is indicated in the inset. Adapted with permission from ref 226. Copyright 2017 American Chemical Society. (d) Anisotropic rotational correlation time (298 K) of FA cations in the $x = 0$ and $x = 0.05$ compounds determined using NMR. Reprinted with permission from ref 204. Copyright 2023 American Chemical Society.

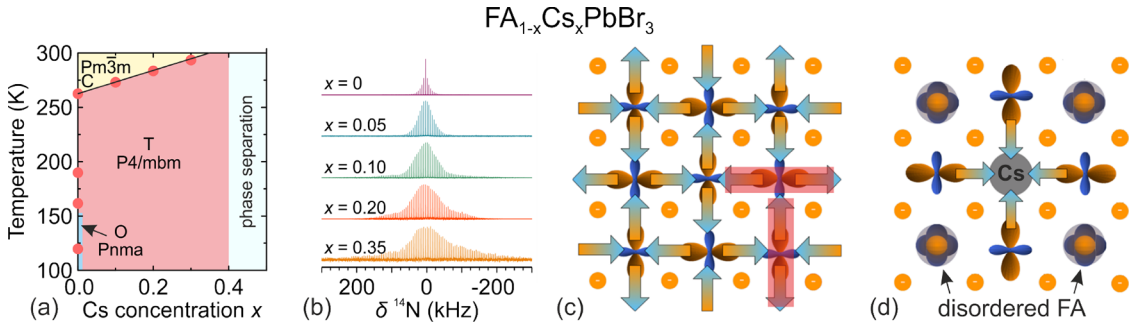

Figure 16. (a) Temperature−composition phase diagram of the mixed $FA_{1-x}Cs_xPbBr_3$ system. Symmetry notation: C - cubic, T - tetragonal, O - orthorhombic. (b) Room-temperature ^{14}N MAS NMR spectra of the $FA_{1-x}Cs_xPbBr_3$ compounds. (c) Schematic cartoon illustrating the FA cation arrangement in a pure $FAPbBr_3$ system. Such a "T"-type (red) long-range quadrupolar order is only possible in a two-dimensional plane. (d) Incorporated Cs^+ ion disrupts the "T"-type arrangement, as neighboring FA cations point to the positive charge of Cs^+ causing disordering of the next-nearest neighbor quadrupoles (black arrows). Reprinted (adapted) with permission from ref 172. Copyright 2020 American Chemical Society.

phase formation at low temperature in the $FA_{1-x}Cs_xPbI_3$ system were also observed in a recent MC study.[228]

Kawachi et al.[186] reported heat capacity measurements of the high quality $FA_{1-x}Cs_xPbI_3$ ($x = 0$ and 0.1) single crystals. For pure $FAPbI_3$ compound, a second-order transition from the cubic to tetragonal symmetry was observed at 280 K (Figure 15b) in agreement with other works (Figure 3). Interestingly, two sequential first-order transitions at 141 and 130 K were observed, as the system evolved to the low-temperature phase. The origin of this intermediate phase was not investigated. An additional weak anomaly was detected at about 80 K. The temperature dependence of the heat capacity of the mixed ($x = 0.1$) crystal revealed that the cubic-tetragonal phase transition shifted to higher temperatures (300 K) (Figure 15b). In addition, mixing resulted in a complete suppression of the intermediate phase, as a single phase transition was detected at 149 K, while the low-temperature anomaly at about 80 K was unaltered. Here we note that mixing also suppressed the intermediate phase of $MAPbBr_3$.[165] The measured transition temperature of 149 K is not in line with the results reported by Charles et al.[171] for the same mixed composition, where transitions were observed at 125 and 180 K (see Figure 15a for comparison). Further studies are needed to clarify this discrepancy.

Ghosh et al.[226] used *ab initio* MD simulations to study the microscopic dynamics in the mixed $FA_{0.9}Cs_{0.1}PbI_3$ and $FA_{0.9}Rb_{0.1}PbI_3$ perovskites. The authors reported that the introduction of smaller cations such as Cs^+ and Rb^+ (Table 1) results in a greater tilt angle of the octahedra compared to pure $FAPbI_3$. In addition, this tilting is locked, and thus the octahedra undergo much more restricted rocking dynamics. This also affects the neighboring molecular cations, which form stronger intermolecular N−H···I H-bonds. As a result, it was observed that the tumbling time scale of the FA cations slowed down more than twice from 2 ps to almost 5 ps (Figure 15c) upon introduction of 10% of Cs. For comparison, the anisotropic rotational correlation time of FA cations in the $x = 0$ and 0.05 compounds was recently measured using quadrupolar relaxation NMR experiments.[204] Slightly slower dynamics were indeed observed in the mixed system, especially around the molecular x-axis (see Figure 15d), although the uncertainties of the determined values were rather high. Note that a later study found that, in contrast to Cs^+, Rb^+ ions have no capacity to be incorporated in $FAPbI_3$.[207]

Mundt et al.[361] studied $FA_{0.83}Cs_{0.17}PbI_3$ thin films to demonstrate that nanoscale compositional heterogeneity can serve as initiation sites for more macroscale irreversible phase segregation. The degree of nanoscale heterogeneity is kinetically controlled and the well-mixed system can be reached when the sample is annealed either long enough or at sufficiently high temperature. In particular, the authors showed that the well-mixed sample, which can be achieved by annealing at 140 °C for 30 min, exhibits a sharp cubic-tetragonal phase transition at 50 °C, while the poorly mixed

https://doi.org/10.1021/acs.chemrev.3c00532
Chem. Rev. 2024, 124, 2281−2326

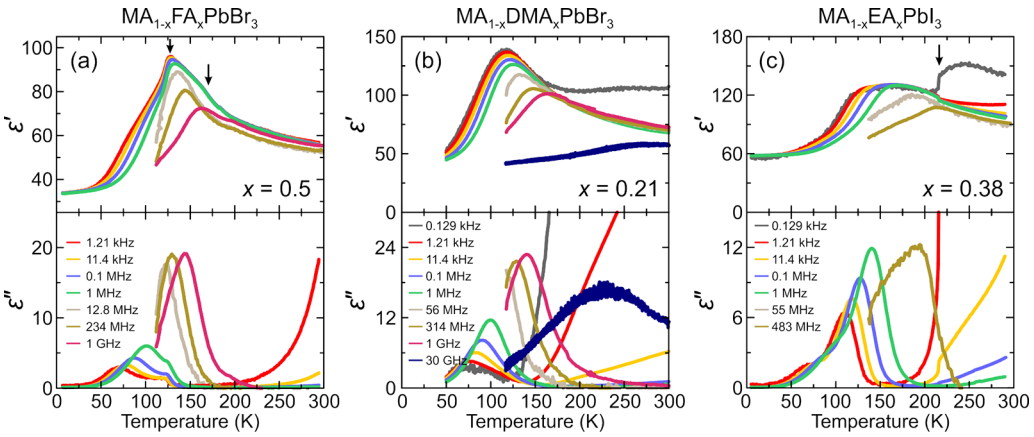

Figure 17. Comparison of the broadband DS of the highly mixed (a) $MA_{0.5}FA_{0.5}PbBr_3$, (b) $MA_{0.79}DMA_{0.21}PbBr_3$, and (c) $MA_{0.62}EA_{0.38}PbI_3$ systems. (a) Reprinted (adapted) with permission from ref 165. Copyright 2021 American Chemical Society. (b) Reprinted (adapted) with permission from ref 164. Copyright 2020 Springer Nature. (c) Reprinted (adapted) with permission from ref 166. Copyright 2022 American Chemical Society.

sample, prepared by annealing at 140 °C for 15 min, showed a smeared out phase transition, reaching the cubic phase close to 130 °C. The smeared phase transition was attributed to a higher level of nanoscale heterogeneity, since various local compositions exhibited phase transitions at various temperatures. This paper emphasized the importance of kinetics on formation of perovskite phases and consequently on the properties of the synthesized thin films.

The mixed $FA_{1-x}Cs_xPbBr_3$ bromide analogues were thoroughly investigated by Mozur et al.[172] using XRD, neutron scattering, and NMR techniques. The solubility limit of Cs in $FAPbBr_3$ was found to be about 40%, beyond which a phase separation occurred. Note that a very similar limit was also observed for the related $MA_{1-x}Cs_xPbBr_3$ and $FA_{1-x}Cs_xPbI_3$ systems.[110,163] The authors used temperature-dependent high-resolution synchrotron XRD to map the phase diagram of $FA_{1-x}Cs_xPbBr_3$ (Figure 16a). For all studied concentrations, a cubic-tetragonal phase transition was detected with its temperature shifting to higher values upon mixing. This indicates reduced stability of the cubic phase in agreement with the phase diagram of the $FA_{1-x}Cs_xPbI_3$ system (Figure 15a). More importantly, a complete suppression of all other (tetragonal-orthorhombic and three isosymmetric[270]) phase transitions was observed even for the lowest mixing level (x = 0.05). However, as stated by the authors, the orthorhombic phase of pure $FAPbBr_3$ already exhibits features of low intensity, which may be even more difficult to resolve in the mixed compositions. Note that a complete disappearance of the isosymmetric transformations of $FAPbBr_3$ was also observed upon incorporation of a small amount of MA cations, indicating that these transitions are very sensitive to small perturbations.[165]

In the same study, the mechanism behind the suppression of the transitions was investigated in more detail.[172] The room-temperature ^{14}N NMR spectra of different compositions indicated increased disorder, i.e., the presence of a larger distribution of local FA environments upon mixing (Figure 16b). The same behavior was also observed for the inorganic framework using the ^{79}Br nuclear quadrupole resonance spectroscopy. However, inelastic neutron scattering data revealed that mixing has only minimal influence on the internal vibrational modes of the FA cations. The ^{1}H NMR relaxation time measurements supported this result by showing that the cation reorientation rates and activation energies are also relatively weakly affected by mixing. Based on these observations, the authors concluded that the incorporated Cs^+ disrupts the FA cation ordering on the longer range, while their local degrees of freedom are retained. In the previous work,[270] the same group proposed that the crystallographically unresolvable isosymmetric phase transitions of $FAPbBr_3$ are caused by the long-range dynamics of the FA cations. This behavior is enabled by the electrostatic quadrupolar interactions between the cations (quadrupole moment $|Q_{11}|$ = 18.3 DÅ), which highly prefer the "T"-type (perpendicular) arrangement (Figure 16c). However, such long-range dynamics do not lead to a long-range order in the system, as it is not possible to form an ordered "T"-type structure in three dimensions, meaning that FA cations are already geometrically frustrated in pure $FAPbBr_3$. Incorporation of Cs^+ ions causes local alignment of the neighboring quadrupole moments disrupting the local "T"-type ordering (Figure 16d) and interrupting the cooperative dynamics associated with these transitions.

4.3.2. $FA_{1-x}GA_xPbI_3$. Mixing of GA in the structure of $FAPbI_3$ was briefly studied by Kubicki et al.[75] using room-temperature ^{13}C and ^{14}N MAS NMR spectroscopy of FA cations. The authors showed that incorporation of GA (x = 0.25) causes a significant broadening of the FA spectral envelope compared to pure α-$FAPbI_3$. This indicates decreased reorientation dynamics of FA cations upon mixing with GA cations. Interestingly, it was also observed that the mixed $FA_{1-x}GA_xPbI_3$ compounds are thermodynamically unstable and become yellow within hours after annealing, meaning that GA cations do not fully stabilize the desirable black phase.

4.4. Summary

Several general observations can be made regarding the A-site mixing effects on the structural and dynamic properties of $MAPbX_3$ and $FAPbX_3$ systems. As expected from the tolerance factor arguments, the size of the guest cation is related to the solubility limit, which ranges from 100% for compatible cations (MA/FA systems) to 20−40% for substantially bigger or smaller guests (DMA, EA, GA, Cs^+). The mismatch in the cation size also greatly affects the structural and dynamic properties of the mixed compounds.

https://doi.org/10.1021/acs.chemrev.3c00532
Chem. Rev. 2024, 124, 2281−2326

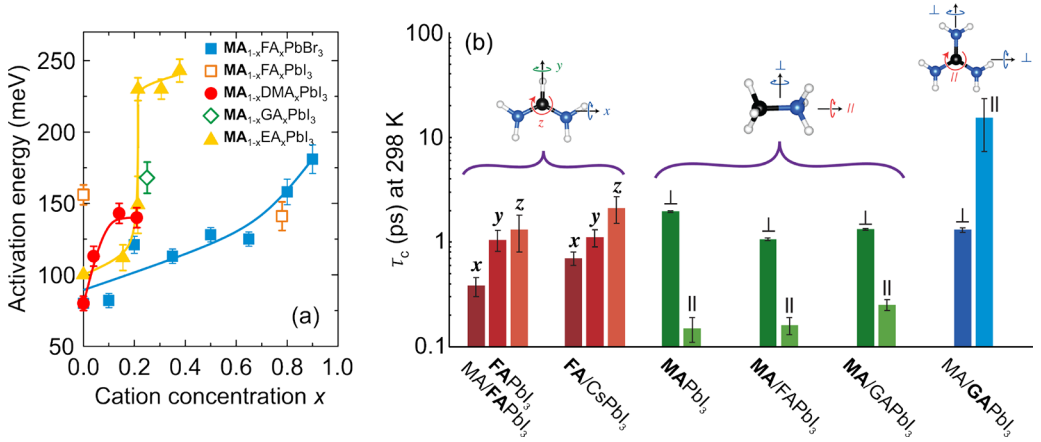

Figure 18. (a) Activation energy of MA cation motion vs guest cation concentration for different MA-based mixed systems determined using the dielectric (solid) and NMR (open points) spectroscopies. Solid curves are a guide for the eye. Data taken from refs 164−166, 204. (b) Rotational correlation times at room temperature of FA, MA, and GA molecular cations in different mixed perovskites obtained by NMR. Reprinted with permission from ref 204. Copyright 2023 American Chemical Society.

The A-site mixing with molecular cations is an effective recipe to suppress the structural phase transitions and thus symmetrize the lattice by stabilizing the desirable cubic phases.[122] This does not hold for mixing with smaller Cs^+ ions, which tend to stabilize the tetragonal phase likely inherited from pure $CsPbX_3$ perovskites. The extent of transition suppression also depends on the cation size - mixing of relatively well compatible MA and FA cations results in a weak suppression, while introduction of big cations (low solubility limit) can cause a complete disappearance of the transitions. This behavior originates from a significant lattice deformation introduced by more bulky molecular cations, which disrupt the H-bonding and octahedral tilt patterns and thus prevent the cooperative long-range ordering.

Similarly to classical inorganic systems, the highly mixed lead halide perovskites also show very broad dielectric responses both in temperature and frequency domains. A comparison of different mixed systems ($MA_{0.5}FA_{0.5}PbBr_3$, $MA_{0.79}DMA_{0.21}PbBr_3$, and $MA_{0.62}EA_{0.38}PbI_3$) is presented in Figure 17 revealing a broad dipolar dispersion of MA cations ranging from almost room temperature at the GHz band to very low temperatures at mHz frequencies (see also Figure 10d). Note that this dispersion is weakly affected by the incompletely suppressed structural phase transitions (e.g., in $MA_{0.5}FA_{0.5}PbBr_3$). The main features of the observed dielectric response resemble the dipolar (orientational) glass (Figure 2c). A likely origin of this phase is frustrated interactions between the molecular cations, which are mediated by the lattice deformations introduced by mixing. It should also be noted that dipolar glass should exhibit freezing dynamics following the Vogel−Fulcher law, but no such behavior was detected for the mixed lead halide perovskites. A possible explanation for this discrepancy is that freezing actually happens, but at low temperatures, where the dipolar relaxation is already shifted to very low frequencies (sub mHz) making the DS experiments infeasible during a reasonable amount of time.

The activation energy of the MA motion in different mixed systems determined by the broadband DS is summarized in Figure 18a.[164−166] An increase of E_a with increasing x is evident, indicating that guest cations raise the rotational barrier for MA cations. In contrast to DS, the activation energy of the MA reorientation at room temperature determined by NMR shows a negligible change upon mixing with FA and GA (Figure 18a), which is likely related to different temperature ranges probed by both techniques.

Here, we also show a summary of the room-temperature rotational correlation times of MA, FA, and GA cations in different mixed compounds determined in a recent NMR study (Figure 18b).[204] Interestingly, all cations exhibit dynamics on a similar few ps time scale. For example, MA and FA reorientation times seem to be only weakly affected by mixing. Note that a very similar time scale in the range of few ps can be obtained by extrapolating the MA relaxation times obtained from the broadband DS (Figure 17). This shows that both techniques essentially probe the same type of dynamics.

5. X-SITE MIXING IN 3D PEROVSKITES

Here, we survey how halide mixing at the X-site affects the structural, phase transition, and dynamic properties of the 3D lead halide perovskites. The majority of works, which fall within the scope of this review, describe the MA- and Cs-based compounds with an exception of MHy-based compositions.

5.1. MA-Based Compounds

5.1.1. $MAPb(I_{1-x}Br_x)_3$. Noh et al. claimed a complete solubility of I^- and Br^- anions (effective radii 220 pm vs 196 pm[362]) at the X-site in the mixed $MAPb(I_{1-x}Br_x)_3$ system.[363] The authors also observed that the room-temperature crystal symmetry changes from tetragonal to cubic for bromine concentration $x \geq 0.2$. A solubility limit was also not considered in more recent works, where the $x = 1/3$ and $2/3$ compositions were investigated.[364,365] However, as demonstrated by the Walsh group using DFT and free energy calculations, the $MAPb(I_{1-x}Br_x)_3$ solid solution should exhibit a very wide miscibility gap ($0.19 \leq x \leq 0.68$) at room temperature, where the phase separation occurs.[366]

The latter result was also confirmed experimentally by Lehmann et al.[367] using synchrotron PXRD, where an even wider miscibility gap of $0.29 \leq x \leq 0.92$ was determined. In the iodine rich phase, a partial solubility of bromine was observed as revealed by a continuous shift of lattice parameters. In contrast, iodine formed cluster-like regions in the bromine-rich phase showing a very poor solubility.

https://doi.org/10.1021/acs.chemrev.3c00532
Chem. Rev. 2024, 124, 2281−2326

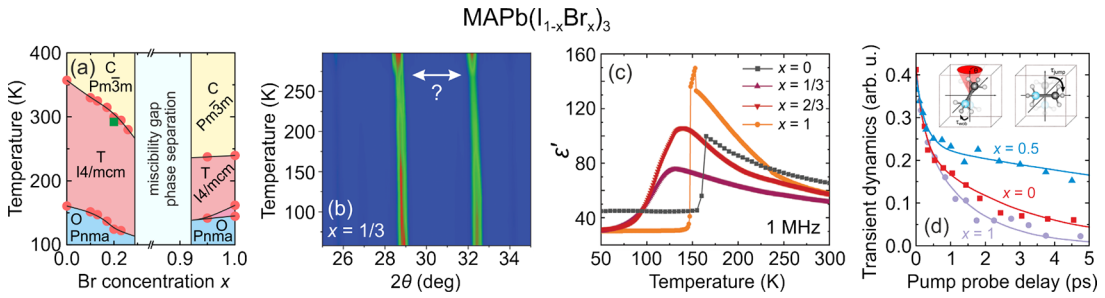

Figure 19. (a) Temperature−composition phase diagram of the $MAPb(I_{1-x}Br_x)_3$ system. Symmetry notation: C - cubic, T - tetragonal, O - orthorhombic. Reprinted (adapted) with permission from ref 367. Copyright 2019 The Royal Society of Chemistry. Green square data point taken from refs 363, 368. (b) PXRD patterns of $MAPbI_2Br$ at different temperatures. (c) Temperature dependence of the real part of the dielectric permittivity of the x = 0, 1/3, 2/3, and 1 compounds measured 1 MHz frequency. Reprinted (adapted) with permission from ref 365. Copyright 2022 Wiley-VCH. (d) Transient anisotropy dynamics of MA cations in the x = 0, 0.5, and 1 compounds. Solid curves show the fits using the wobbling-in-a-cone relaxation model (inset). Adapted with permission from ref 369. Copyright 2017 American Chemical Society.

Based on the temperature-dependent PXRD experiments, the authors also mapped the temperature−composition phase diagram of the $MAPb(I_{1-x}Br_x)_3$ system (Figure 19a).[367] A clear decrease of both phase transition temperatures was observed upon mixing up to the miscibility gap in the iodine-rich region, indicating stabilization of the cubic phase. This behavior is analogous to mixing of molecular cations at the A-site. On the other end of the phase diagram, the cubic-tetragonal phase transition was found to be barely affected by mixing. However, the intermediate tetragonal phase of $MAPbBr_3$ was suppressed indicating that, despite low solubility and tendency to cluster, iodine still perturbs the long-range order in the system.

Interestingly, Tang et al. found that the miscibility gap in the $MAPb(I_{1-x}Br_x)_3$ system could be avoided using the mechanochemical synthesis instead of a typical solvent synthesis.[368] In such a way, the authors synthesized the whole series of compositions and observed no signatures of phase separation. In addition, it was found that the system changes room-temperature symmetry from tetragonal to cubic at $x \approx 0.2$ in agreement with other works.[363,367] For comparison, the authors also prepared $MAPb(I_{1-x}Br_x)_3$ films using the wet chemical route and observed a wide miscibility gap ($0.1 < x < 0.8$) in line with other studies.[366,367] No phase separation was also observed in a recent NMR and MD work by Fykouras et al.,[205] where mixed compositions with x = 1/3, 1/2, and 2/3 were synthesized by mechanochemical synthesis. In this study, the authors also demonstrated that iodine and bromine ions are randomly dispersed and that reorientation of the MA cations within the inorganic cage highly depends on a local halide distribution. Note that Askar et al. also found no miscibility gap and a homogeneous halide distribution in the related mixed $FAPb(I_{1-x}Br_x)_3$ and $FAPb(Br_{1-x}Cl_x)_3$ systems using ^{207}Pb NMR.[370]

A recent study by Shahrokhi et al.[365] reported a more detailed multitechnique investigation of the phase transitions in $MAPbI_2Br$ (x = 1/3) and $MAPbIBr_2$ (x = 2/3) single crystal compounds obtained using solvent synthesis. As discussed above, while the former compound could be considered to be on the edge of the miscibility gap, the latter composition should result in phase separation and iodide clustering. However, this issue was not addressed, as full solubility was assumed. The authors claimed no anomalies in the DSC and PXRD data for both compounds, indicating a complete suppression of the phase transitions and stabilization of the cubic phase. This result is also not in line with the phase diagram provided by Lehmann et al.,[367] where transitions at about 270 and 115 K can be expected at the lower edge of the miscibility gap $x \approx 0.3$ (Figure 19a). Indeed, a closer look at the PXRD data reported by Shahrokhi et al.[365] seems to show some change of the diffraction patterns at 275 K (Figure 19b), suggesting that the phase transitions may actually be not fully suppressed. Interestingly, a substantial contribution of unusual monoclinic phase was also employed to better fit the PXRD data of both compounds, which may again be related to the unaccounted phase separation at these mixed compositions. Note that López et al.[371] also did not observe any symmetry lowering in the synchrotron XRD data down to 120 K for the x = 1/3 sample, which was obtained using mechanochemical synthesis.

The same work by Shahrokhi et al.[365] also reported the dielectric properties of the x = 0, 1/3, 2/3, and 1 compounds (Figure 19c). As expected, pure $MAPbI_3$ and $MAPbBr_3$ perovskites demonstrated a sudden decrease of the dielectric permittivity related to the MA cation ordering, as the materials transitioned into the orthorhombic phase.[183,340,341] In contrast, the temperature dependence of the dielectric permittivity of the mixed compositions revealed a broad featureless peak extending below 100 K (Figure 19c). Note that a very similar dielectric response was also obtained for the A-site mixing (see Figure 17), indicating that both approaches affect the MA cation dynamics in a similar way. In addition, as pointed by the authors, such a dielectric response might be a signature of a dipolar (orientational) glass phase.

The MA cation dynamics in the mixed $MAPb(I_{0.4}Br_{0.6})_3$ film were investigated by Selig et al.[369] using 2D IR spectroscopy and classical MD simulations. Note that the studied x = 0.6 composition should be deep within the miscibility gap (Figure 19a), which was not discussed by the authors. As found by Lehmann et al.,[367] such a bromine concentration should result in phase clustering with partial mixing. The 2D IR spectroscopy of pure $MAPbI_3$ and $MAPbBr_3$ perovskites revealed wobbling and reorientation dynamics of the MA cations occurring on the 0.3 ps and 1.5−3 ps time scale, respectively. In the mixed compound, the wobbling dynamics remained the same, while the time scale of the cation reorientation increased significantly up to 15 ps. This indicates hindering of the MA cation motion in the mixed halide system likely caused by the local distortions of the inorganic framework. The experimental results were also supported by the MD simulations, which also revealed partial suppression of the MA dynamics in the mixed compound. Similar MD simulation results were also obtained

https://doi.org/10.1021/acs.chemrev.3c00532
Chem. Rev. 2024, 124, 2281−2326

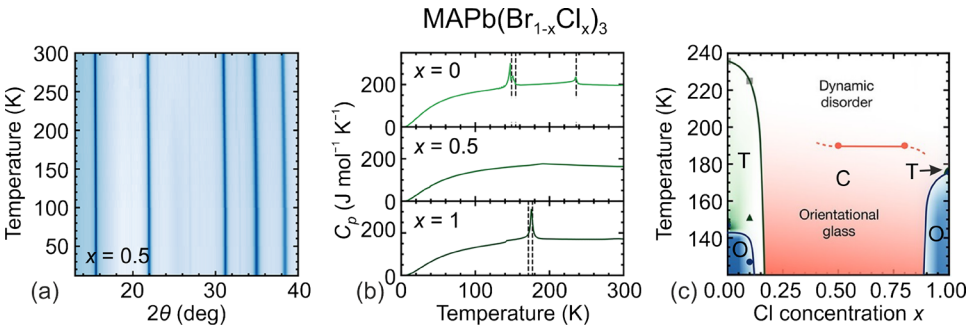

Figure 20. (a) PXRD pattern of the $MAPb(Br_{0.5}Cl_{0.5})_3$ composition showing a complete suppression of the phase transitions. (b) Temperature dependence of the heat capacity for the x = 0, 0.5, and 1 compositions. (c) Temperature−composition phase diagram of the $MAPb(Br_{1-x}Cl_x)_3$ system. Symmetry notation: C - cubic, T - tetragonal, O - orthorhombic. Reprinted with permission from ref 381. Copyright 2021 American Chemical Society.

for the x = 1/3 and 2/3 compositions in the aforementioned study by Shahrokhi et al.,[365] while Grüninger et al.[206] observed restriction in the cation mobility due to halide mixing for the $MA_{0.15}FA_{0.85}Pb(I_{0.85}Br_{0.15})_3$ composition. Note that the 2D IR spectroscopy of the $MA_{1-x}Cs_xPbI_3$ ($x \leq 0.3$) mixture revealed a very similar change of the wobbling and jumping dynamics of the MA cations upon introduction of Cs^+ ions.[344]

5.1.2. $MAPb(I_{1-x}Cl_x)_3$. Due to an even larger difference in the ionic radii of I^- and Cl^- anions (220 pm vs 181 pm),[362] an even wider miscibility gap is expected for the mixed $MAPb(I_{1-x}Cl_x)_3$ system. Among the first studies of these compounds, Colella et al.[372] reported a maximum chlorine content of x = 0.04, while somewhat higher incorporation up to x = 0.1 was stated by Unger et al.[373] (both solvent synthesis). Pistor et al. reported the miscibility gap of $0.05 < x < 0.5$.[374] In a more recent work published by the Schorr group,[375] the miscibility gap was refined using high-resolution synchrotron PXRD to be $0.03 < x < 0.99$. Note that no deviation of symmetry from the parent compounds was observed in these weakly mixed compositions.

The same group also used inelastic and quasielastic neutron scattering to study the MA dynamics in the x = 0.02 compound.[376] Upon introduction of chlorine, a significantly faster C_3 reorientation around the C−N bond of the MA cations in the orthorhombic phase was observed compared to pure $MAPbI_3$ (485 ps vs 1635 ps). In addition, mixing also decreased the activation energy of this motion from 41 to 22 meV. As discussed by the authors, these findings indicate that even a minute amount of chlorine is sufficient to substantially weaken the H-bonds between the MA cations and inorganic framework. In a recent study, the same group also reported that the temperature of the tetragonal-orthorhombic phase transition is lowered in the mixed composition (x = 0.02) by about 5 K compared to $MAPbI_3$, indicating that a small amount of mixing also affects the structural phase transitions.[377]

5.1.3. $MAPb(Br_{1-x}Cl_x)_3$. In contrast to mixing with iodine, no evidence of the miscibility gap was found for the mixed $MAPb(Br_{1-x}Cl_x)_3$ perovskites due to more similar radii of Br^- and Cl^- anions (196 pm vs 181 pm).[362364,368,369,377−382] Several studies observed cubic symmetry at room temperature for different compositions covering the whole mixing interval[364,380,381,383] in agreement with the symmetry of the end members (see Figure 3).

A cubic symmetry of the x = 1/3, 1/2, 2/3 mixed compositions at room temperature was also observed by López et al. using neutron powder diffraction.[379] In addition, the authors also determined the preferred MA cation orientation in the inorganic cage, which was found to change from the [110] to [111] and finally to the [100] direction, as the chlorine content increased, and the size of the unit cell shrunk. The change of preferred directions also indicates the reduction in the degrees of freedom of MA cation, as the delocalization along the [110], [111], and [100] axis involves 6, 4, and 3 possible orientations, respectively.

The phase transitions in the mixed $MAPb(Br_{1-x}Cl_x)_3$ system were first investigated by Alvarez-Galván et al. using synchrotron XRD.[380] The authors observed a complete suppression of the phase transitions for the studied highly mixed compositions (x = 1/2 and 2/3) and stabilization of the cubic $Pm\bar{3}m$ phase.

A similar behavior was also obtained in a recent multitechnique study by van de Goor,[381] where a series of mixed compounds was investigated covering the whole range of compositions. A complete suppression of the phase transitions was obtained for the $0.2 < x < 0.8$ compositions as evident from the PXRD and heat capacity measurements (Figure 20a,b). The authors also determined the phase diagram of this mixed system using the temperature dependence of the lattice microstrain extracted from the PXRD results (Figure 20c). Interestingly, for the highly mixed compositions, the microstrain value remained constant throughout the measured temperature range. This was attributed to the formation of the orientational glass phase caused by the halide disorder, which in turn distorts the octahedra and affects the MA cation motion. In a recent study, Naqvi et al. also observed local inhomogeneous environments of the MA cations in the mixed compositions of $MAPb(Br_{1-x}Cl_x)_3$ using Raman spectroscopy.[377] Note that a similar mechanism of the glassy phase formation was also proposed for the mixed A-site systems such as $MA_{1-x}DMA_xPbBr_3$.[164]

The MA cation dynamics in the mixed $MAPb(Br_{0.4}Cl_{0.6})_3$ compound was also studied in the aforementioned work by Selig et al.[369] using the 2D IR spectroscopy and classical MD simulations. Similarly to the mixed $MAPb(I_{0.4}Br_{0.6})_3$ composition (Figure 19d), the $MAPb(Br_{0.4}Cl_{0.6})_3$ film sample also showed a substantial increase of the MA cation reorientation time to 5 ps in contrast to much shorter time scales observed for the end members (1.5 ps for x = 0, and 1.2 ps for x = 1).

5.2. Cs-Based Compounds

5.2.1. $CsPb(I_{1-x}Br_x)_3$. Several studies revealed no miscibility gap in the mixed inorganic $CsPb(I_{1-x}Br_x)_3$ perovskite

https://doi.org/10.1021/acs.chemrev.3c00532
Chem. Rev. 2024, 124, 2281−2326

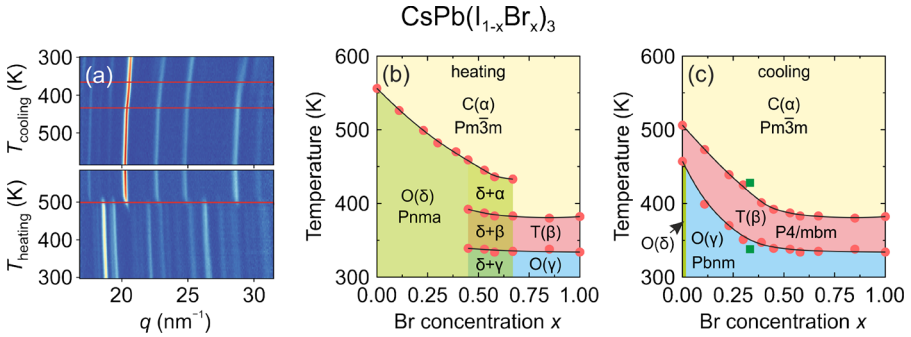

Figure 21. (a) Grazing-incidence wide-angle X-ray scattering pattern of the printed $CsPb(I_{0.77}Br_{0.23})_3$ thin film sample obtained on heating and then subsequent cooling runs. Red lines indicate the phase transitions. Temperature−composition phase diagram of the $CsPb(I_{1-x}Br_x)_3$ system obtained on (b) heating and (c) subsequent cooling. Symmetry notation: C - cubic, T - tetragonal, O - orthorhombic. Green data points in (c) are taken from ref 388. Reprinted (adapted) with permission from ref 384. Copyright 2020 The Royal Society of Chemistry.

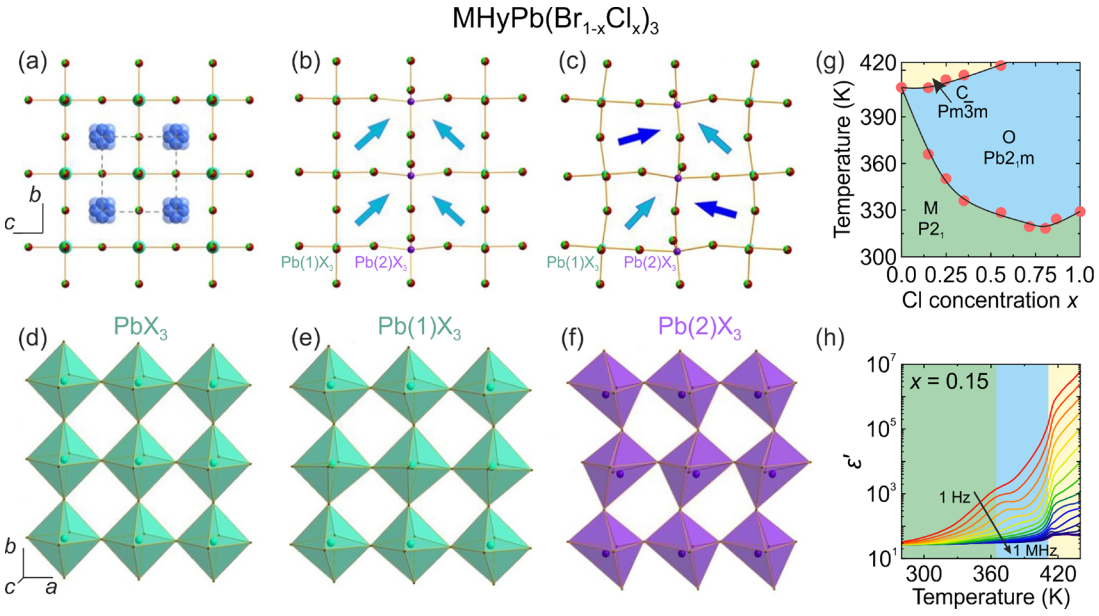

Figure 22. Crystal structure of the mixed $MHyPb(Br_{1-x}Cl_x)_3$ system in the (a) cubic, (b) orthorhombic, and (c) monoclinic phases. Arrows represent electric dipole moments of MHy cations. (d) Single [100] layer of the PbX_6 octahedra in the cubic phase. [100] layers of (e) less-distorted $Pb(1)X_6$ and (f) highly distorted $Pb(2)X_6$ octahedra in both polar orthorhombic and monoclinic phases. (g) Temperature−composition phase diagram of the $MHyPb(Br_{1-x}Cl_x)_3$ system. Symmetry notation: C - cubic, O - orthorhombic, M - monoclinic. (h) Temperature dependence of the real part ε' of the complex dielectric permittivity of the $MHyPb(Br_{0.85}Cl_{0.15})_3$ pellet sample. The dielectric response is dominated by the conductivity effects. Reprinted (adapted) with permission from ref 118. Copyright 2022 American Chemical Society.

system,[232,384−386] although Wang et al. reported the onset of phase segregation under light illumination.[387] Many works also reported that introduction of bromine suppresses the yellow phase and stabilizes the photoactive black phase of $CsPbI_3$.[232,384−386,388,389]

Näsström et al.[384] used in situ grazing-incidence wide-angle X-ray scattering and X-ray fluorescence experiments to investigate structural phase transitions and phase diagrams for a broad range of compositions of the $CsPb(I_{1-x}Br_x)_3$ thin films obtained by inkjet printing and ordinary coating (for Br-rich compositions). The compositions containing up to moderate amounts of bromine ($x \leq 0.45$) were found to form the orthorhombic (*Pnma*) yellow δ-phase at room temperature. This phase was converted to the cubic ($Pm\bar{3}m$) black α-phase upon heating to high temperatures (Figure 21a), and the temperature of this transition decreased significantly with increasing x, indicating stabilization of the cubic phase (Figure 21b). A subsequent cooling of the mixed compounds showed a contrasting behavior compared to heating, as, instead of the yellow phase formation, a phase transition sequence (cubic-tetragonal-orthorhombic) of the black polymorph was observed (Figure 21c). Note that pure $CsPbI_3$ perovskite was an exception exhibiting an immediate conversion back to the yellow phase (Figure 21c). On the opposite side of the phase diagram, Br-rich compositions ($x \geq 0.85$) already crystallized into the orthorhombic (*Pbnm*) black γ-phase (Figure 21b) resulting in the same behavior during heating and cooling. Interestingly, for the intermediate values of mixing, the coexistence of the yellow and black phases was observed at room temperature prior the heating run (Figure 21b). Note that similar phase transition temperatures of the black polymorph were also observed for the $CsPb(I_{2/3}Br_{1/3})_3$ thin film by Breniaux et al.[388] (Figure 21c). A gradual evolution of the phase transitions with varying composition is in a sharp contrast to the MA-based systems, where phase transitions are typically suppressed.[164−166,336,381]

https://doi.org/10.1021/acs.chemrev.3c00532
Chem. Rev. 2024, 124, 2281−2326

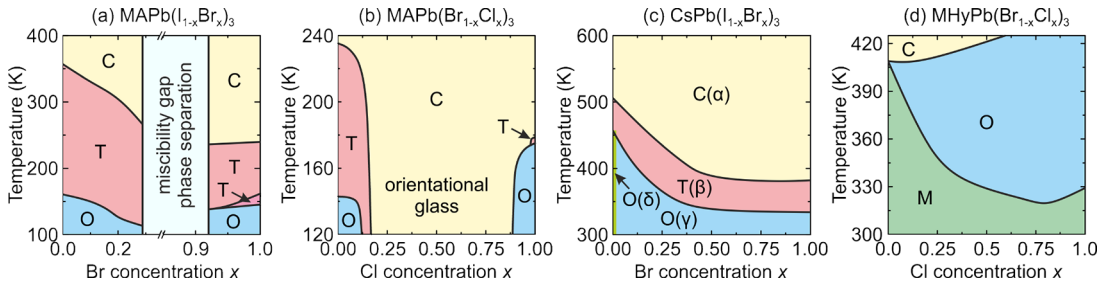

Figure 23. Comparison of the temperature−composition phase diagrams of the mixed-halide (a) $MAPb(I_{1-x}Br_x)_3$, (b) $MAPb(Br_{1-x}Cl_x)_3$, (c) $CsPb(I_{1-x}Br_x)_3$ (black phase except for $x = 0$), and (d) $MHyPb(Br_{1-x}Cl_x)_3$ systems. Symmetry notation: C - cubic, T - tetragonal, O - orthorhombic, M - monoclinic. (a) Adapted with permission from ref 367. Copyright 2019 The Royal Society of Chemistry. (b) Adapted with permission from ref 381. Copyright 2021 American Chemical Society. (c) Adapted with permission from ref 384. Copyright 2020 The Royal Society of Chemistry. (d) Adapted with permission from ref 118. Copyright 2022 American Chemical Society.

5.2.2. $CsPb(Br_{1-x}Cl_x)_3$. This mixed system was investigated in the already discussed study by van de Goor et al.[381] using PXRD and heat capacity measurements assisted by DFT calculations. In contrast to the hybrid $MAPb(Br_{1-x}Cl_x)_3$ system (Figure 20), the authors did not observe lattice stabilization and formation of the orientational glass phase even for the highest mixing level ($x = 0.5$), as the system remained in the orthorhombic (*Pnma*) symmetry inherited from the end member compositions. The DFT calculations also revealed orthorhombic distortion and a narrow distribution of the Pb−halide−Pb angle, indicating preservation of the long-range order.

This may be related to the fact that in both $CsPbBr_3$ and $CsPbCl_3$, end members' discernible octahedral distortions are evident within the orthorhombic *Pnma* structures, as indicated by the Pb−X−Pb angles distributed in the range of 157−165° and 160−169°, respectively.[287,288] This observation stands in contrast to $MAPb(Br_{1-x}Cl_x)_3$, wherein the energetically favored structural configuration is an average cubic one, characterized by a broad Pb−halide−Pb angle distribution that is also shifted toward the theoretically ideal cubic value of 180°. A contributing factor to the absence of long-range order may be attributed to the disparate degrees of distortion observed in nonmixed compositions. In $MAPbBr_3$, for instance, all Pb−Br−Pb angles demonstrate a near-equivalence, fluctuating between 166.8° and 167.3°,[269] while Pb−Cl−Pb angles in $MAPbCl_3$ exhibit a widespread distribution in the range of 155−170°.[390]

5.3. MHy-Based Compounds

Unlike archetypal $MAPbX_3$ and $FAPbX_3$ compounds, $MHyPbX_3$ (X = Br, Cl) 3D perovskites show exceptionally distorted and noncentrosymmetric framework consisting of alternating weakly and strongly distorted PbX_6 octahedra.[184,185] The $MHyPbBr_3$ compound exhibits a single structural phase transition from the cubic to monoclinic phase at 418 K, while $MHyPbCl_3$ also shows a single transition from the orthorhombic to monoclinic symmetry at 342 K (Figure 3). Note that the iodide analogue does not form a 3D perovskite and instead crystallizes into a 2D layered structure.[391]

5.3.1. $MHyPb(Br_{1-x}Cl_x)_3$. Halide mixing effects in the MHy-based hybrid perovskites were recently studied by some of us using a suite of different experimental techniques including SCXRD, DSC, SHG, and DS.[118] No evidence of the miscibility gap was observed in the whole range of mixing in agreement with the related $MAPb(Br_{1-x}Cl_x)_3$ system.[381] The SCXRD experiments of $MHyPb(Br_{1-x}Cl_x)_3$ revealed that mixing does not change the polar symmetry, MHy cation arrangement, and framework distortions of the corresponding structural phases (see Figure 22a−f). The DSC experiments were used to follow the phase transition temperatures with mixing as summarized in the phase diagram presented in Figure 22g. Upon an increase of x, the stability region of the orthorhombic $Pb2_1m$ phase gradually increased at the expense of the cubic $Pm\bar{3}m$ and monoclinic $P2_1$ phases.

Note that no lattice symmetrization (phase transition suppression) was observed in the mixed compositions of $MHyPb(Br_{1-x}Cl_x)_3$ in contrast to the MA-based system (Figure 20c), where signatures of the glassy behavior were detected. In addition, no substantial broadening of the transition anomalies was observed in $MHyPb(Br_{1-x}Cl_x)_3$ upon mixing. These results indicate that introduction of Cl^- anions did not destroy the long-range order in this system, and thus lattice symmetrization and formation of the dipolar glass phase cannot be expected. This was also evident in the dielectric responses of the mixed compounds, which were dominated by the conductivity processes (Figure 22h). The absence of the lattice symmetrization may be explained by the already significantly deformed and rigid inorganic framework at room temperature. Note that a similar behavior was also observed for the related $CsPb(Br_{1-x}Cl_x)_3$ system.[381]

5.3.2. $MHyPb(Br_{1-x}I_x)_3$. In the same study,[118] an attempt was made to incorporate iodine in the structure of $MHyPbBr_3$ perovskite using solvent synthesis. A $MHyPb(Br_{0.93}I_{0.07})_3$ composition of 3D perovskite was obtained as revealed by energy-dispersive X-ray spectroscopy analysis. SCXRD and DSC experiments showed that this compound undergoes a structural phase transition at 390 K from the cubic $Pm\bar{3}m$ to monoclinic $P2_1$ phase, both inherited from pure $MHyPbBr_3$.

5.4. Summary

Several important observations can be made from the reviewed results of mixed-halide lead halide perovskites. The mixed compositions with iodine, which has the largest ionic radius, may result in a miscibility gap, which is especially pronounced for the MA-based compounds obtained using the solvent synthesis. Interestingly, it seems that this gap can be reduced or fully suppressed using mechanochemical synthesis. There is no miscibility gap for the mixed Br/Cl compounds allowing one to fully chart the phase diagrams.

The temperature−composition phase diagrams of the mixed $MAPb(I_{1-x}Br_x)_3$, $MAPb(Br_{1-x}Cl_x)_3$, $CsPb(I_{1-x}Br_x)_3$, and $MHyPb(Br_{1-x}Cl_x)_3$ systems are summarized in Figure 23 revealing vastly different behaviors. $MAPb(I_{1-x}Br_x)_3$ compounds obtained using solvent synthesis exhibited a wide

https://doi.org/10.1021/acs.chemrev.3c00532
Chem. Rev. 2024, 124, 2281−2326

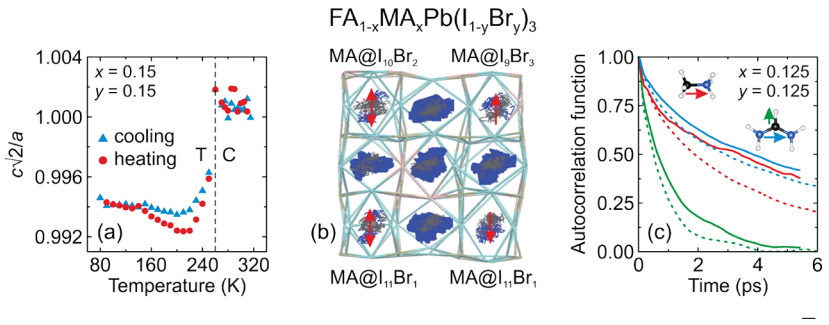

Figure 24. (a) Temperature dependence of the reduced lattice parameter ratio $c\sqrt{2}/a$ of the mixed $FA_{0.85}MA_{0.15}Pb(I_{0.85}Br_{0.15})_3$ system obtained on cooling and heating. (b) Trajectories of the MA and FA cations in the mixed $FA_{0.875}MA_{0.125}Pb(I_{0.875}Br_{0.125})_3$ perovskite obtained by the *ab initio* MD. Arrows indicate average direction of the MA cations. (c) Simulated vector autocorrelation functions of the MA and FA cations (insets) in the same solid solution (solid curves) compared with simulations obtained in the parent $MAPbBr_3$ and $FAPbI_3$ compounds (dashed curves). (a) Adapted with permission from ref 392. Copyright 2020 Wiley-VCH. (b, c) Reprinted (adapted) with permission from ref 393. Copyright 2022 The Royal Society of Chemistry.

region of phase separation, while well-mixed compositions outside this gap showed a significant lowering of the transition temperatures upon mixing[367] (Figure 23a). This indicates increased stability of the cubic phase due to the disorder induced by random halide distribution, while the dielectric response obtained for the high levels of mixing showed signatures of the glassy phase formation.[365] The phase diagram of the $MAPb(Br_{1-x}Cl_x)_3$ system, which has no miscibility gap, revealed a complete suppression of the phase transitions and symmetrization of the lattice for the highly mixed compounds (Figure 23b).[381] For these compositions, the formation of the orientational glass phase was also observed.

The phase diagrams and effects of mixing are qualitatively different when mixed compositions are obtained from the end members, which exhibit distorted lower symmetry structures already at room temperature such as Cs-based (orthorhombic) and MHy-based (monoclinic) compounds. In both cases, no suppression of the phase transitions and lattice symmetrization were observed, as systems gradually evolved with halide mixing maintaining sharp phase transition anomalies (Figure 23c,d). This indicates preservation of the long-range order and absence of the glassy phase. Such a behavior may be explained by a much higher stability of the distorted phases (much higher transition temperatures) compared to the MA-based perovskites.

6. SIMULTANEOUS A- AND X-SITE MIXING IN 3D PEROVSKITES

Here, we discuss how simultaneous mixing at the A- and X-sites affects the structural phase transitions and cations dynamics in 3D lead halide perovskites. The reported studies concentrate on the highly promising $FA_{1-x}MA_xPb(I_{1-y}Br_y)_3$ and $FA_{1-x}Cs_xPb(I_{1-y}Br_y)_3$ systems, where FA is the dominant molecular cation.

6.1. $FA_{1-x}MA_xPb(I_{1-y}Br_y)_3$

Greenland et al. used temperature-dependent PXRD to study the structural phase transitions in the $FA_{0.85}MA_{0.15}Pb(I_{0.85}Br_{0.15})_3$ thin film sample.[392] The phase transition from the cubic ($Pm\bar{3}m$) to tetragonal ($P4/mbm$) symmetry was observed at 260 K (Figure 24a), which is about 15 K lower compared to pure $FAPbI_3$ (Figure 3). In addition, the lowering of the phase transition temperature seems to be more pronounced compared to the $FA_{0.85}MA_{0.15}PbI_3$ composition, where mixing was done only at the A-site (see phase diagram in Figure 5). The authors also claim observation of the phase transition to the γ-phase, which occurred at 90 K instead of about 150 K observed for pure $FAPbI_3$. Interestingly, upon heating, the PXRD peaks of this low-temperature phase persisted up to 220 K, indicating a very broad hysteresis (also visible in Figure 24a).

Menéndez-Proupin et al. employed *ab initio* MD to study molecular cation dynamics in the $FA_{0.875}MA_{0.125}Pb(I_{0.875}Br_{0.125})_3$ perovskite.[393] The density maps of the C and N atoms revealed that the FA cations rotate freely in the lattice, while the MA cations have a unique orientation during the calculated trajectory (Figure 24b), which seems to be independent of the number of neighboring Br^- anions. The authors also calculated the vector autocorrelation function for both molecular cations showing that in the highly mixed composition the dynamics of both cations are slower (Figure 24c). Note that the same behavior was obtained in the mixed $FA_{0.9}Cs_{0.1}PbI_3$ (Figure 15c)[226] and $MAPb(I_{0.5}Br_{0.5})_3$ systems (Figure 19d).[369]

Johnston et al. used QENS to study molecular cation dynamics in the highly mixed $FA_{0.8}MA_{0.15}Cs_{0.05}Pb(I_{1-y}Br_y)_3$ (y = 0, 0.1, 0.15, and 0.2) system with an addition of a small amount of Cs^+ cations at the A-site.[394] The temperature-dependent mean-squared displacement data revealed a phase transition to the low-temperature phase at about 100 K independent of the halide mixing. This result does not agree with the phase diagram of the mixed $MA_{1-x}FA_xPbI_3$ system (y = 0) (Figure 5), suggesting that Cs^+ cations may significantly affect the phase transitions. The authors also observed the strongest suppression of the molecular cation dynamics (particularly FA) for the y = 0.15 composition.

Xie et al.[395] grew high-quality single crystals of $(FAPbI_3)_{1-x}(MAPbBr_3)_x$. They observed that the best composition for a black phase without segregation is x = 0.1−0.15 and that the incorporation of MA is essential for stabilization of the black phase from the thermodynamics point of view. Namely, incorporation of MA tunes the tolerance factor toward the ideal value of 1 and lowers the Gibbs free energy via unit cell contraction and cation disorder. On the other hand, Br incorporation also stabilizes the black phase but from the kinetics point of view, because this anion controls the crystallization kinetics and reduces defect density.

https://doi.org/10.1021/acs.chemrev.3c00532
Chem. Rev. 2024, 124, 2281−2326

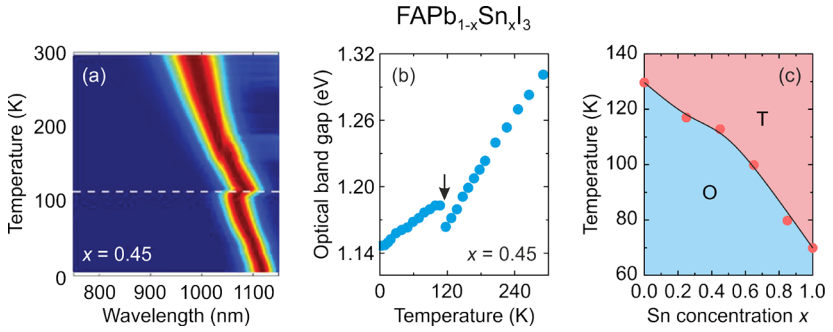

Figure 25. (a) Temperature dependence of the PL signal of $FAPb_{0.55}Sn_{0.45}I_3$ perovskite. (b) Temperature dependence of the optical band gap determined from the PL data of the same sample. Arrow marks the phase transition point. (c) Temperature−composition phase diagram of the tetragonal−orthorhombic phase transition in $FAPb_{1-x}Sn_xI_3$ system. Reprinted (adapted) with permission from ref 89. Copyright 2018 Wiley-VCH.

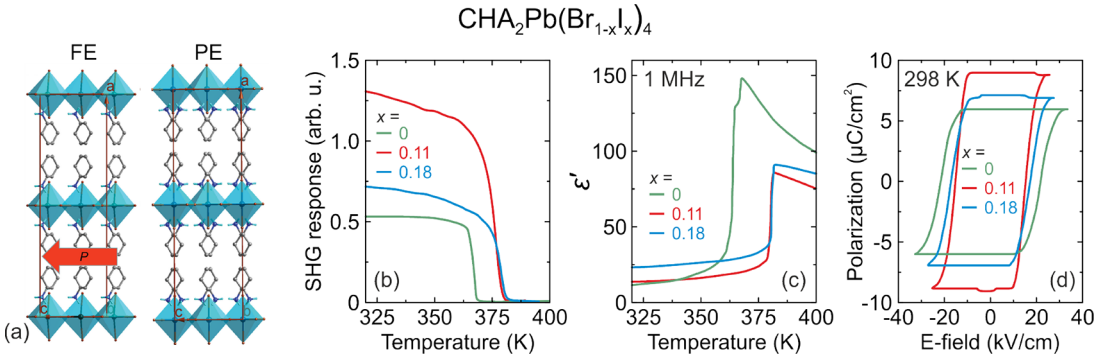

Figure 26. (a) Crystal structure of pure CHA_2PbBr_4 compound in the ferroelectric (FE) and paraelectric (PE) phases. Cation disorder is present in the PE phase. (b) Temperature dependence of the (b) SHG response and (c) real part ε' of the complex dielectric permittivity (1 MHz) of the mixed $CHA_2Pb(Br_{1-x}I_x)_4$ system (x = 0, 0.11, and 0.18). (d) Ferroelectric hysteresis loops of the same compounds obtained at room temperature. Reprinted (adapted) with permission from ref 397. Copyright 2016 Wiley-VCH.

6.2. $FA_{1-x}Cs_xPb(I_{1-y}Br_y)_3$

Barrier et al.[396] used synchrotron X-ray diffraction to probe the evolution of crystal structure across the tetragonal-cubic phase transition for $FA_{1-x}Cs_xPb(I_{1-y}Br_y)_3$ thin films with x = 0.17−0.4 and y = 0.05−0.3. By analysis of the octahedral tilt angle, they observed that the cubic-tetragonal phase transition occurred over temperature range on the order of 40 °C. This behavior proved that the samples were poorly mixed and contained coexisting cubic and tetragonal regions. It has been discussed that the compositional heterogeneity can have two origins. The first one is due to the thermodynamic separation of the mixed perovskite into two or more distinct phases driven by minimization of the free energy, whereas the second one likely results from kinetics due to the solution-processing methods used to fabricate thin films. The authors have made no attempt to distinguish between these components but emphasized that it is important to take into account the presence of heterogeneity, since it may lead to chemical, structural, and electronic property heterogeneity on multiple length scales.

7. B-SITE MIXING IN 3D PEROVSKITES

The number of works reporting on how the B-site mixing affects the structural and dynamic properties of hybrid perovskites is highly limited. Here, we discuss two $MAPbI_3$ and $FAPbI_3$ perovskite systems, where lead is partially replaced by tin.

7.1. $MAPb_{1-x}Sn_xI_3$

The room-temperature structural properties of the mixed $MAPb_{1-x}Sn_xI_3$ system were investigated by Kanatzidis group in two subsequent studies.[93,94] The authors observed a full compatibility of both parent compounds, as no solubility limit in the mixed perovskites was detected. For all compositions, the room-temperature crystal structure adopted tetragonal symmetry. For the Sn-rich compositions ($x \geq 0.5$), the *P4mm* space group was obtained, while the $x < 0.5$ compounds including $MAPbI_3$ were indexed using the noncentrosymmetric *I4cm* space group instead of the expected centrosymmetric *I4/mcm*. The absence of the centrosymmetry was not discussed or proved by the authors making this assignment questionable.

7.2. $FAPb_{1-x}Sn_xI_3$

Parrott et al.[89] reported a more detailed investigation of the mixing effects in the related $FAPb_{1-x}Sn_xI_3$ perovskites, where no solubility limit was also observed. The authors used temperature-dependent PL and light absorption experiments to probe how introduction of tin affects the phase transitions (Figure 25a) and optical properties such as optical band gap (Figure 25b). Clear anomalies were observed in the measured data at the low-temperature phase transition point allowing construction of the phase diagram (Figure 25c). The observed transition likely corresponds to the tetragonal-orthorhombic symmetry change based on the symmetry of the parent compounds at such temperatures (Figure 3).[170]

In the aforementioned piezoresponse force microscopy study by Ahmadi et al.,[339] the authors observed that, similarly to $MA_{0.15}FA_{0.85}PbI_3$, the $FAPb_{0.85}Sn_{0.15}I_3$ compound also

https://doi.org/10.1021/acs.chemrev.3c00532
Chem. Rev. 2024, 124, 2281−2326

exhibits ferroelectric domain-like structures, however, much weaker than expected for classical ferroelectric domains.

Further studies with the emphasis on the structural phase transitions and dynamics are necessary to provide a more detailed picture of the B-site mixing effects.

8. HALIDE, METAL, AND CATION (A-, A′-, A″-SITE) MIXING IN LOWER-DIMENSIONAL PEROVSKITES AND RELATED COMPOUNDS

Here, we discuss how mixing affects the structural and dynamic properties of low dimensional lead halide perovskites. Note that the number of works reporting on these effects is significantly lower compared to the 3D $APbX_3$ compounds.

8.1. $CHA_2Pb(Br_{1-x}I_x)_4$

Ye et al.[397] used DSC, SHG, light absorption, dielectric and hysteresis loop measurements to probe how introduction of iodine up to $x = 0.18$ affects the phase transitions, band gap, ferroelectric and NLO properties of 2D layered perovskite comprising cyclohexylammonium (CHA) cations (Figure 26a). On cooling, pure CHA_2PbBr_4 undergoes a ferroelectric phase transition from the *Cmca* to the $Cmc2_1$ phase at 363 K. The authors showed that mixing increased the phase transition temperature to 378 and 380 K for the $x = 0.11$ and 0.18 compositions, respectively. In addition, mixing also increased intensity of the SHG signal (Figure 26b) and narrowed the band gap from 3.05 eV for CHA_2PbBr_4 to 2.74 eV for $CHA_2Pb(Br_{0.82}I_{0.18})_4$ while maintaining the phase transition. Interestingly, the dielectric anomaly associated with the phase transitions showed no broadening upon mixing (Figure 26c) in contrast to the majority of the 3D $APbX_3$ perovskites (see e.g. Figure 19c). In addition, the ferroelectric properties also remained in the mixed compositions (Figure 26d) showing that the CHA cation ordering is decoupled from the halide mixing.

A full range of compositions ($0 \le x \le 1$) of the same system was studied by Yangui et al.[37] It was shown that a composition-induced phase transition from the $Cmc2_1$ to *Pbca* phase occurs for $0.5 < x < 0.6$ at room temperature. The change in composition also led to the appearance of white-light emission for $x < 0.5$.

8.2. $(C_9H_{19}NH_3)_2PbI_2Br_2$

Abid et al.[398] studied phase transition in $(C_9H_{19}NH_3)_2PbI_2Br_2$ solid solution, which crystallizes in a 2D perovskite structure. Using DSC, PXRD, and IR spectroscopy, they showed that the phase transition occurs around 230 K. The crystal structure below 230 K was not solved, but spectroscopic studies revealed that the phase transition is related to a decreased conformational disorder of the methylene units in the alkyl chains.

8.3. Br-$PEA_2Pb(Br_xCl_{1-x})_4$

Pareja-Rivera et al.[40] studied the effect of mixing at the X-site on the PL properties of 2D perovskite comprising 4-bromophenethylammonium (Br-PEA) cation. No solubility limit was observed, and the crystal structure of this system was found to be orthorhombic *Fmm*2 in the whole range of mixing. Analysis of the structural data revealed a much larger distortion of the inorganic layers for $x = 0$ compared to $x = 1$. Lattice parameters *b* and *c* increased with increasing Br content, whereas an opposite behavior was observed for the *a* parameter. Mixing at the X-site had a pronounced effect on the band gap and PL, as the band gap narrowed with increasing *x*, while PL for the $x = 1$ composition was dominated by a sharp violet emission with the peak maximum near 420 nm. This emission shifted to the UV range with decreasing *x*. When *x* decreased to about 0.6, a new broadband emission appeared near 500 nm, and its intensity increased on further lowering of *x*.

8.4. $PEA_2Pb(Br_xCl_{1-x})_4$ and $PEA_2Pb(Br_xI_{1-x})_4$

Mixing effects at the X-sites were also reported for 2D perovskites comprising the phenethylammoium (PEA) cation.[39,399,400] Similarly to the Br-PEA analogue discussed above, Cai et al. claimed no solubility limit in the $PEA_2Pb(Br_xCl_{1-x})_4$ system, but the crystal symmetry was lower, triclinic $P\bar{1}$.[39]

The XRD and DFT calculations revealed phase separation for the $x = 0.25$ composition of the mixed $PEA_2Pb(Br_xI_{1-x})_4$ analogue, while no phase separation was observed for $x \ge 0.5$.[399] For $x = 0.75$, two PL bands were observed and only one for $x = 0.25$ and 0.5, which was attributed to different crystal configurations simultaneously present in the prepared film. Another study of $PEA_2Pb(Br_xI_{1-x})_4$ system showed the presence of two (002) diffraction peaks for the $x = 0.79$ composition, suggesting an immiscible system with two discrete halide phases.[400]

8.5. $HA_2Pb(Br_xI_{1-x})_4$ and $HA_2FAPb_2(Br_xI_{1-x})_7$

A mixing effect at the X-sites was also reported for $HA_2Pb(Br_xI_{1-x})_4$ and $HA_2FAPb_2(Br_xI_{1-x})_7$ compounds (HA = *n*-hexylammonium).[400] The situation for these systems is very similar to that observed for $PEA_2Pb(Br_xI_{1-x})_4$,[400] as these halides do not show full solubility, and there is a clear crossover from near-pure-I to near-pure-Br phases for $x = 0.84-0.88$.[400] The authors also showed that these systems may show photoinduced phase separation over hundreds of ms for focused laser beam and over minutes under the diffuse UV light.

8.6. $Et_3PrNPb(Br_{1-x}I_x)_3$

Shao et al.[124] reported investigation of the mixing effects at the X-site of 1D hybrid lead halide comprising globular-shaped triethylpropylammonium (Et_3PrN) cations. The authors found no solubility limit for this mixed halide system.

The DSC experiments showed that the phase transition is weakly affected by mixing as its temperature gradually decreased from 480 K for $x = 0$ to 445 K for $x = 1$. The entropy associated with the phase transition was the largest for pure $Et_3PrNPbBr_3$ (43.54 J mol^{-1} K^{-1}) and decreased to 32.36 J mol^{-1} K^{-1} for $Et_3PrNPbI_3$ indicating a lower degree of ordering. The mixing with iodine also results in the shift of the band gap from 3.50 eV for $x = 0$ to 2.93 eV for $x = 1$.

8.7. t-$BA_2Pb(Br_{1-x}I_x)_4$

The mixed halide system containing *tert*-butylammonium (t-BA) branched spacer cation was recently studied by Ovčar et al.[36] The authors showed that the end members crystallize into the polar $P2_1$ structures: 1D for the iodide (t-$BAPbI_3$), and layered 2D nonperovskite for the bromide (t-$BAPb_2Br_5$). Interestingly, the perovskite architecture was found to be stabilized in the mixed halide t-$BA_2PbBr_2I_2$ system (2D layered perovskite structure, monoclinic $P2_1/c$ space group), however, at the expense of the polar symmetry.

8.8. $(3AMP)_x(4AMP)_{1-x}(FA)_y(MA)_{1-y}Pb_2Br_7$

Mixing of organic cations in a DJ type structure of $(3AMP)_x(4AMP)_{1-x}(FA)_y(MA)_{1-y}Pb_2Br_7$ (3AMP = 3-(aminomethyl)piperidinium, 4AMP = 4-(aminomethyl)-piperidinium) was studied by Mao et al.[138] This system

https://doi.org/10.1021/acs.chemrev.3c00532
Chem. Rev. 2024, 124, 2281−2326

showed a composition-induced phase transition from the monoclinic *Cm* symmetry for $x = 1$ and $y = 1$ to the monoclinic *Pc* phase for the $(3AMP)_{0.5}(4AMP)_{0.5}FAPb_2Br_7$, $(3AMP)_{0.5}(4AMP)_{0.5}FA_{0.5}MA_{0.5}Pb_2Br_7$, $(4AMP)FA_{0.5}MA_{0.5}Pb_2Br_7$, $(4AMP)FAPb_2Br_7$, and $(3AMP)MAPb_2Br_7$ compositions. The monoclinic *Cc* symmetry was reported for $x = 0$ and $y = 0$ as well as for $x = 0.5$ and $y = 0$. It was found that these structural changes have a significant impact on the Pb−Br−Pb bond angle and the band gap.

8.9. $(BA_{0.5}PEA_{0.5})_2MAPb_2Br_7$

Mixing of organic spacer cations was also studied in an RP type structure of $(BA_{0.5}PEA_{0.5})_2MAPb_2Br_7$.[136] The structure of $BA_2MAPb_2Br_7$ was refined in the orthorhombic *Ama*2 space group, and $PEA_2MAPb_2Br_7$ was reported to be isostructural to $PEA_2MAPb_2I_7$[136] with the triclinic space group $P\bar{1}$.[401] The XRD results showed that $(BA_{0.5}PEA_{0.5})_2MAPb_2Br_7$ has a distinct structure from its parent compounds (triclinic *P*1).

8.10. $[AA_xIdPA_{1-x}]_2MA_{n-1}Pb_nI_{3n+1}$ ($n = 2-4$)

Another reported RP system with mixing at the A′-sites is $[AA_xIdPA_{1-x}]_2MA_{n-1}PbnI_{3n+1}$ ($n = 2-4$) family of compounds (AA = allylammonium, IdPA = iodopropylammonium).[402] The most important conclusion from studies of this system is that, whereas the end members crystallize in the centrosymmetric structures, the mixed A′ phases are acentric. For instance, $AA_2MA_2Pb_3I_{10}$ and $IdPA_2MA_2Pb_3I_{10}$ crystallize in the $P2_1/c$ and $P2/c$ structure, respectively, while $[AA_xIdPA_{1-x}]_2MA_2Pb_3I_{10}$ phases are described by the noncentrosymmetric *Pc* space group.[402]

8.11. $(BA)_2(MA_{1-x}EA_x)_2Pb_3I_{10}$

Mixing of organic cations in RP phases can also be realized at the "perovskitizer" sites, as demonstrated by Fu et al. in a study of $(BA)_2(MA_{1-x}EA_x)_2Pb_3I_{10}$.[140] The end members $BA_2EA_2Pb_3I_{10}$ and $BA_2MA_2Pb_3I_{10}$ crystallize in the $Cmc2_1$ and *C*2*cb* space groups, respectively, and, due to larger ionic radius of EA, $BA_2EA_2Pb_3I_{10}$ feature a higher degree of structural deformation. The authors showed that the symmetry of the mixed cation phases decreased to monoclinic *Cc*, and the average equatorial Pb−I−Pb bond angle of the inner layers strongly decreased with increasing EA fraction indicating higher structural distortion.

8.12. $(PEA)_2(MA_{1-x}GA_x)_2Pb_3I_{10}$

Another example of the RP phase with mixed cations at the "perovskitizer" sites is the $(PEA)_2(MA_{1-x}GA_x)_2Pb_3I_{10}$ system studied by Ramos-Terrón et al.[141] In this work, thin films up to $x = 0.5$ were prepared, which is a much higher incorporation fraction compared to the 3D analogues (e.g., 25% in $MA_{1-x}GA_xPbI_3$[69]). The authors observed shifts of diffraction peaks with increasing x due to enlargement of the unit cell. When the GA content approached 30%, a clear change in the width of the diffraction peaks was observed. This behavior was attributed to a sudden change in the arrangement of the mixed cations. To obtain information on the degree of lattice distortion induced by incorporation of GA, the DFT calculations were performed for the $x = 0.25$ and $x = 0.5$ compositions. The obtained results revealed low distortion of the inorganic layers on GA incorporation, even for a high GA content.

8.13. $(BA)_2(MA_{1-x}Cs_x)Pb_2Br_7$

Mixing at the "perovskitizer" sites was also reported by Ma et al. for $(BA)_2(MA_{1-x}Cs_x)Pb_2Br_7$.[403] The authors grew single crystals for $x = 1$, 0.93, 0.79, and 0.66 and showed that incorporation of MA led to a decrease of the phase transition temperature from 411 K for $x = 1$ to 399, 383, and 379 K for $x = 0.93$, 0.79, and 0.66, respectively. For all solid solutions, the ferroelectricity of the low-temperature phase was confirmed by observation of the polarization hysteresis loops. The incorporation of MA led to narrowing of the band gap from 2.7 eV for $x = 1$ to 2.43 eV for $x = 0.66$. Most interestingly, the introduction of MA also resulted in a very large, at least 10-fold, enhancement of the photoactivity of this layered perovskite. This effect was attributed to the reduction of the exciton binding energy and enhanced ferroelectric polarization. As a result, the photoelectric activity of the mixed-cation crystals ($x = 0.66$) exceeded that of previously reported self-driven detectors based on hybrid lead halide perovskites.

8.14. $PEA_2Pb_{1-x}Sn_xBr_4$

Sui et al.[127] reported investigation of the mixing effects at the B-site of 2D hybrid lead halide comprising aromatic PEA cations. This system shows a full solubility, while maintaining the same triclinic *P*1 crystal structure with decreased lattice parameters due to smaller ionic radius of Sn^{2+} (93 pm) compared to Pb^{2+} (120 pm). The smaller ionic radius of Sn^{2+} was also shown to be responsible for a shift of the band gap and PL peak to lower energies with increasing x.

In summary, literature data show that ion mixing in low-dimensional perovskites may significantly tune optoelectronic properties and lead to new symmetry of the mixed phases and loss of the inversion center.

9. CONCLUSIONS AND OUTLOOK

In this review, we provided a systematic and comprehensive picture of the mixing effects on the structural and dynamic properties of 3D and low-dimensional lead halide perovskites. The following important generalizations can be drawn from the reviewed studies:

(i) Frequently, the extent of mixing is limited by phase separation, which is especially pronounced, if the parent compounds have structures of different topologies. The phase separation directly affects the phase diagrams and material properties and thus must be carefully considered and determined. In general, for lead halide perovskites, kinetics often have a strong impact on the phases that form. This problem is especially important in the fabrication of thin films, since the spin-coating process often leads to pronounced heterogeneity.[361,395,396] The presence of nanoscale local compositional variations may lead to structural and optoelectronic property heterogeneity on multiple length scales.[361,396] It also complicates the phase transition behavior since slight variations in chemical composition can result in a different crystallographic phase being thermodynamically favorable and shift the transition temperature, leading to smearing of the transition anomaly.[361,396] It has been shown that the A-site segregation can be often mitigated by annealing the samples either long enough or at a sufficiently high temperature.[361,396] Another way is to perform rapid crystallization by antisolvent dripping.[404,405] Trapping of the metastable phases can also be done by fast quenching.[264]

(ii) The mixing tends to partially or completely suppress the structural phase transitions resulting in the stabilization of the cubic phase and thus symmetrization of the crystal lattice, which is related to the improved stability, performance, and functionality of the mixed compounds.

https://doi.org/10.1021/acs.chemrev.3c00532
Chem. Rev. 2024, 124, 2281−2326

(iii) Symmetrization of the lattice is frequently accompanied by signatures of the orientational (dipolar) glass phase, which occurs due to the multivalley potentials and frustrated interactions introduced by mixing and mediated by the local lattice deformations.

(iv) The symmetrization effect seems to be less pronounced or absent, if parent compounds exhibit highly stable low-symmetry phases at room temperature (e.g., Cs- and MHy-based perovskites). In this case, the evolution of the phase transitions with mixing is continuous, and signatures of the glassy phase are absent.

(v) The dynamics of molecular cations typically become slower upon mixing. This is especially pronounced at low temperature, where more bulky guest cations tend to freeze (e.g., DMA) and cause local deformation of the crystal lattice, which in turn increases the rotation barrier and hinders the dynamics of the smaller cations (e.g., MA).

(vi) Mixing in low-dimensional lead halide perovskites shows interesting behavior related to the occurrence of new crystal symmetries and loss of the inversion center. However, mixing in these compounds is significantly less studied compared to the 3D perovskites and therefore requires more attention. This is especially important in the context of ferroelectric low-dimensional perovskites, which upon mixing may form a ferroelectric relaxor phase instead of the dipolar glass.

Lastly, we identify other new promising systems and directions for further studies of the mixing effects on the structural and dynamic properties of lead halide and related perovskites. Such systems include hollow perovskites,[72] deficient perovskites,[406] and quasi 3D perovskites,[407] all of which exhibit a substantial degree of disruption of the inorganic framework. It can be expected that in such compounds the molecular cation frustration would be even higher, as both organic and inorganic sublattices would significantly contribute to disorder.

Mixing in the newly discovered aziridinium-based 3D perovskites[237,298,408,409] is also of high interest, especially from the stability point of view. As these perovskites have a 3D topology and high stability of the cubic phase, their solid solutions with high fractions of MA and FA should be feasible.

The B-site mixing in 3D perovskites is also significantly understudied compared to the A- and X-site mixing despite seemingly interesting effects on the structural phase transitions. In addition, mixing at the B-site should also significantly affect the off-centering dynamics of the inorganic framework,[342,410] which should be directly visible in the low-temperature dielectric response of these materials. This is also related to lattice fluctuations resulting in low-symmetry correlated octahedral distortions observed in lead halide perovskites. It is very likely that mixing (especially at the B-site) would significantly affect such octahedral rotational instabilities. However, due to the requirement of advanced structural characterization techniques, such studies of the mixed systems are very rare.

As discussed, a major area of research in lead halide perovskites is related to the stabilization of the black photoactive phases of $FAPbI_3$ and $CsPbI_3$ compounds by utilizing several strategies including ion mixing—a topic which is out of scope for this review. However, the stabilization by mixing should inevitably affect the structural phase transitions and dynamics in the stabilized black phases of $FAPbI_3$ and $CsPbI_3$. One could expect a connection between the induced phase stability and suppression of the structural phase transitions in the black phases of these compounds. For example, Marshall et al. demonstrated a successful stabilization of the black phase of $CsPbI_3$ by DMA cations reaching incorporation fractions up to 25%,[411] while similar values of DMA proved to be sufficient to fully stabilize the cubic phase in the $MA_{1-x}DMA_xPbBr_3$ system.[164] Interestingly, a recent NMR study found that the mixed $Cs_{1-x}DMA_xPbI_3$ perovskite phases only form when they are kinetically trapped by rapid antisolvent-induced crystallization.[404] Of potential interest is also doping with Rb, which can be incorporated into the $CsPbBr_3$, the black phase of $CsPbI_3$, and $CsPb(I/Br)_3$ solid solutions.[412]

As interesting example of the black phase stabilization was also recently reported by Duijnstee et al., where a small amount (x = 0.005) of tetrahydrotriazinium (THTZ-H) molecular cation was incorporated in the structure of $FAPbI_3$.[413] The samples were obtained from solutions containing methylenediammonium dichloride or hexamethylenetetramine, which then formed THTZ-H during the subsequent reactions with FA. Remarkably, the authors reported that such a mixing leads to an impressive enhancement of the black phase stability of $FAPbI_3$ lasting for more than one year under ambient conditions. It can be expected that such a pronounced effect of THTZ-H on the black phase stabilization could also significantly alter the structural phase transitions and FA cation dynamics in α-$FAPbI_3$.

The mixing effects and the dielectric response are also significantly understudied in the related lead-free families of hybrid materials such as tin halides,[297,414,415] antimony halides,[416,417] bismuth halides,[417−421] tellurium halides,[422] and double (e.g., Ag/Bi) perovskites.[423−427] Many of these compounds undergo structural phase transitions related to the ordering-disordering phenomena and ferroelectric properties. Thus, one can expect a formation of similar frustrated phases in these materials upon mixing.

We note that, apart from dipolar glass, mixing-induced frustration may also lead to other exotic disordered phases. From the applications point of view, of particular interest is the relaxor phase,[58] which is rather common in the mixed classical inorganic compounds. However, the formation of the relaxor phase requires mixing of ferroelectrics, while the ferroelectricity in 3D lead halide perovskites is questionable.[183] On the other hand, numerous lower-dimensional perovskites are ferroelectric and antiferroelectric (see Table 2), and thus their mixing holds a significant potential for formation of relaxor and other complex frustrated phases.

There is presently a lot of interest in chiral layered lead halides, in which employment of a chiral organic cation leads to transfer of the chirality into the achiral inorganic framework.[428−435] Due to the intrinsic noncentrosymmetry of chiral cations, chiral lead halides show unique and highly attractive features such as optical rotation, circular dichroism, circularly polarized PL, polarization-dependent SHG, ferroelectricity, bulk photovoltaic effect, chirality-induced spin selectivity, and topological quantum properties.[428−434] Furthermore, the strong spin−orbit coupling of metal and halide ions imparts significant Rashba-Dresselhaus spin-splitting of otherwise 2-fold spin-degenerate electronic bands.[430,431,436] We are not aware of any report on the mixing effect on phase transitions and lattice dynamics in chiral lead halides. However, there are some examples of mixed chiral hybrid perovskites reporting a significant tuning of optical properties

https://doi.org/10.1021/acs.chemrev.3c00532
Chem. Rev. 2024, 124, 2281−2326

upon mixing at the B- and X-sites.[433,437,438] Thus, a substantial effect on the structural phase transitions and dynamics can be also expected.

Another intriguing feature of certain mixed inorganic ferroelectrics is the presence of a morphotropic phase boundary, where the crystal structure changes abruptly upon mixing, and the electromechanical (piezoelectric) properties become maximized.[439] The observation of such a phase boundary in mixed lead halide perovskites would undoubtedly open new research and application frontiers of these materials.

AUTHOR INFORMATION

Corresponding Author

Mantas Simenas − *Faculty of Physics, Vilnius University, LT-10257 Vilnius, Lithuania;* orcid.org/0000-0002-2733-2270; Email: mantas.simenas@ff.vu.lt

Authors

Anna Gagor − *Institute of Low Temperature and Structure Research, Polish Academy of Sciences, PL-50-422 Wroclaw, Poland*

Juras Banys − *Faculty of Physics, Vilnius University, LT-10257 Vilnius, Lithuania*

Miroslaw Maczka − *Institute of Low Temperature and Structure Research, Polish Academy of Sciences, PL-50-422 Wroclaw, Poland;* orcid.org/0000-0003-2978-1093

Complete contact information is available at: https://pubs.acs.org/10.1021/acs.chemrev.3c00532

Notes

The authors declare no competing financial interest.

Biographies

Mantas Šimėnas received his Ph.D. degree in Physics from Vilnius University (Lithuania). Afterwards, he was a research fellow in magnetic resonance at University College London (UK). Currently, he is a professor in physics at the Faculty of Physics at Vilnius University focusing, among other topics, on the solid state physics, structural phase transitions, dielectric response, and dynamic phenomena of hybrid perovskites and related materials.

Anna Gągor received her Ph.D. degree in Physics from the Institute of Low Temperature and Structure Research, Polish Academy of Sciences (Poland). Since then, she has been associated with the Institute, where she currently holds the position of Associate Professor and serves as the Head of the Structure Research Department. She is a member of the Polish Crystallographic Society and the Commission on Inorganic and Mineral Structures associated with the International Union of Crystallography. Her research focuses on the structural analysis of crystalline materials using X-ray diffraction, including the investigation of phase transitions, structure−property relationships in organic−inorganic hybrids, and ferroic and multiferroic materials.

Jūras Banys obtained his Ph.D. degree at the Faculty of Physics at Vilnius University (Lithuania). He completed his postdoc training in solid state physics at Oxford University and Leipzig University. Currently, he is a professor in physics at Vilnius University. Jūras is the world-leading expert in the dielectric characterization of the structural phase transitions, relaxor and dipolar glass phases, and lattice dynamics in mixed inorganic perovskites. He is best known for the development and application of the ultrabroadband dielectric spectroscopy to characterize different perovskite systems.

Mirosław Mączka received his Chemistry diploma from the Wrocław University of Science and Technology (Poland) and his Ph.D. degree in Chemistry from the Institute of Low Temperature and Structure Research, Polish Academy of Sciences (Poland). He is currently a Professor in Chemistry at the Institute of Low Temperature and Structure Research. His research focuses broadly on hybrid perovskites, optoelectronic materials, synthesis science, and vibrational spectroscopy.

ACKNOWLEDGMENTS

This project has been funded by the Research Council of Lithuania (LMTLT) (Agreement No. S-MIP-22-73). The authors thank the anonymous reviewers for insightful suggestions.

ABBREVIATIONS

AA	allylammonium
i-AM	isoamylammonium
ACE	acetamidinium cation
i-BA	isobutylammonium
AM	amylammonium
IM	imidazolium cation
AZR	aziridinium
i-PA	isopropylammonium
BA	butylammonium
MA	methylammonium cation
BPA	3-bromopropylammonium
MACH	cyclohexanemethylammonium
Br-PEA	4-bromophenethylammonium
MHy	methylhydrazinium cation
BZA	benzylammonium
PA	propylammonium
CHA	cyclohexylammonium
PEA	phenethylammoium
CPA	3-chloropropylammonium
t-ACH	4-aminomethyl-1-cyclohexanecarboxylate
DMA	dimethylammonium cation
t-BA	*tert*-butylammonium
EA	ethylammonium cation
TEA	thioethylammonium cation
Et_3PrN	triethylpropylammonium
THTZ-H	tetrahydrotriazinium cation
FA	formamidinium cation
TZ	1,2,4-triazolium
GA	guanidinium cation
3AMP	3-(aminomethyl)piperidinium
HA	*n*-hexylammonium
4AMP	4-(aminomethyl)piperidinium
HY	hydrazinium cation
4IBA	4-iodobutylammonium
HEA	hydroxyethylammonium cation
ACI	alternating cations in the interlayer space
NMR	nuclear magnetic resonance
DFT	density functional theory
PL	photoluminescence
DJ	Dion−Jacobson
PXRD	powder X-ray diffraction
DS	dielectric spectroscopy
QENS	quasi elastic neutron scattering
DSC	differential scanning calorimetry
RP	Ruddlesden−Popper
IR	infrared

https://doi.org/10.1021/acs.chemrev.3c00532
Chem. Rev. 2024, 124, 2281−2326

SCXRD	single crystal X-ray diffraction
MD	molecular dynamics
SHG	second-harmonic generation
MC	Monte Carlo
XRD	X-ray diffraction
NLO	nonlinear optical

REFERENCES

(1) Kojima, A.; Teshima, K.; Shirai, Y.; Miyasaka, T. Organometal Halide Perovskites as Visible-Light Sensitizers for Photovoltaic Cells. *J. Am. Chem. Soc.* **2009**, *131*, 6050−6051.

(2) Liu, M.; Johnston, M. B.; Snaith, H. J. Efficient Planar Heterojunction Perovskite Solar Cells by Vapour Deposition. *Nature* **2013**, *501*, 395−398.

(3) Park, N.-G. Organometal Perovskite Light Absorbers Toward a 20% Efficiency Low-Cost Solid-State Mesoscopic Solar Cell. *J. Phys. Chem. Lett.* **2013**, *4*, 2423−2429.

(4) Shang, Y.; Liao, Y.; Wei, Q.; Wang, Z.; Xiang, B.; Ke, Y.; Liu, W.; Ning, Z. Highly Stable Hybrid Perovskite Light-Emitting Diodes Based on Dion-Jacobson Structure. *Sci. Adv.* **2019**, *5*, No. eaaw8072.

(5) Zhang, X.; Liu, H.; Wang, W.; Zhang, J.; Xu, B.; Karen, K. L.; Zheng, Y.; Liu, S.; Chen, S.; Wang, K.; Sun, X. W. Hybrid Perovskite Light-Emitting Diodes Based on Perovskite Nanocrystals with Organic-Inorganic Mixed Cations. *Adv. Mater.* **2017**, *29*, No. 1606405.

(6) Kim, Y.-H.; Cho, H.; Lee, T.-W. Metal Halide Perovskite Light Emitters. *Proc. Natl. Acad. Sci. U. S. A.* **2016**, *113*, 11694−11702.

(7) Quan, L. N.; García de Arquer, F. P.; Sabatini, R. P.; Sargent, E. H. Perovskites for Light Emission. *Adv. Mater.* **2018**, *30*, No. 1801996.

(8) Jeong, J.; Kim, M.; Seo, J.; Lu, H.; Ahlawat, P.; Mishra, A.; Yang, Y.; Hope, M. A.; Eickemeyer, F. T.; Kim, M.; et al. Pseudo-Halide Anion Engineering for α-$FaPbI_3$ Perovskite Solar Cells. *Nature* **2021**, *592*, 381−385.

(9) Yoo, J. J.; Seo, G.; Chua, M. R.; Park, T. G.; Lu, Y.; Rotermund, F.; Kim, Y.-K.; Moon, C. S.; Jeon, N. J.; Correa-Baena, J.-P.; et al. Efficient Perovskite Solar Cells via Improved Carrier Management. *Nature* **2021**, *590*, 587−593.

(10) Zhou, Y.; Zhou, Z.; Chen, M.; Zong, Y.; Huang, J.; Pang, S.; Padture, N. P. Doping and Alloying for Improved Perovskite Solar Cells. *J. Mater. Chem. A* **2016**, *4*, 17623−17635.

(11) Ono, L. K.; Juarez-Perez, E. J.; Qi, Y. Progress on Perovskite Materials and Solar Cells with Mixed Cations and Halide Anions. *ACS Appl. Mater. Interfaces* **2017**, *9*, 30197−30246.

(12) Lin, H.; Zhou, C.; Tian, Y.; Siegrist, T.; Ma, B. Low-Dimensional Organometal Halide Perovskites. *ACS Energy Lett.* **2018**, *3*, 54−62.

(13) Hong, K.; Le, Q. V.; Kim, S. Y.; Jang, H. W. Low-Dimensional Halide Perovskites: Review and Issues. *J. Mater. Chem. C* **2018**, *6*, 2189−2209.

(14) Goldschmidt, V. M. Die Gesetze der Krystallochemie. *Naturwissenschaften* **1926**, *14*, 477−485.

(15) Kieslich, G.; Sun, S.; Cheetham, A. K. Solid-State Principles Applied to Organic-Inorganic Perovskites: New Tricks for an Old Dog. *Chem. Sci.* **2014**, *5*, 4712−4715.

(16) Travis, W.; Glover, E. N. K.; Bronstein, H.; Scanlon, D. O.; Palgrave, R. G. On the Application of the Tolerance Factor to Inorganic and Hybrid Halide Perovskites: A Revised System. *Chem. Sci.* **2016**, *7*, 4548−4556.

(17) Breternitz, J.; Lehmann, F.; Barnett, S. A.; Nowell, H.; Schorr, S. Role of the Iodide-Methylammonium Interaction in the Ferroelectricity of $CH_3NH_3PbI_3$. *Angew. Chem., Int. Ed.* **2020**, *59*, 424−428.

(18) Quan, L. N.; Rand, B. P.; Friend, R. H.; Mhaisalkar, S. G.; Lee, T.-W.; Sargent, E. H. Perovskites for Next-Generation Optical Sources. *Chem. Rev.* **2019**, *119*, 7444−7477.

(19) Han, Y.; Yue, S.; Cui, B.-B. Low-Dimensional Metal Halide Perovskite Crystal Materials: Structure Strategies and Luminescence Applications. *Adv. Sci.* **2021**, *8*, No. 2004805.

(20) Maczka, M.; Drozdowski, D.; Stefanska, D.; Gagor, A. Zero-Dimensional Mixed-Cation Hybrid Lead Halides with Broadband Emissions. *Inorg. Chem. Front.* **2023**,.107222

(21) Elleuch, S.; Lusson, A.; Pillet, S.; Boukheddaden, K.; Abid, Y. White Light Emission from a Zero-Dimensional Lead Chloride Hybrid Material. *ACS Photonics* **2020**, *7*, 1178−1187.

(22) Akkerman, Q. A.; Manna, L. What Defines a Halide Perovskite? *ACS Energy Lett.* **2020**, *5*, 604−610.

(23) Shao, S.; Cui, X.; Li, Z. Recent Progress in Understanding the Structural, Optoelectronic, and Photophysical Properties of Lead Based Dion-Jacobson Perovskites as Well as Their Application in Solar Cells. *ACS Mater. Lett.* **2022**, *4*, 891−917.

(24) Niu, T.; Xue, Q.; Yip, H.-L. Advances in Dion-Jacobson Phase Two-Dimensional Metal Halide Perovskite Solar Cells. *Nanophotonics* **2021**, *10*, 2069−2102.

(25) Gao, X.; Zhang, X.; Yin, W.; Wang, H.; Hu, Y.; Zhang, Q.; Shi, Z.; Colvin, V. L.; Yu, W. W.; Zhang, Y. Ruddlesden-Popper Perovskites: Synthesis and Optical Properties for Optoelectronic Applications. *Adv. Sci.* **2019**, *6*, No. 1900941.

(26) Siwach, P.; Sikarwar, P.; Halpati, J. S.; Chandiran, A. K. Design of Above-Room-Temperature Ferroelectric Two-Dimensional Layered Halide Perovskites. *J. Mater. Chem. A* **2022**, *10*, 8719−8738.

(27) Cortecchia, D.; Yin, J.; Petrozza, A.; Soci, C. White Light Emission in Low-Dimensional Perovskites. *J. Mater. Chem. C* **2019**, *7*, 4956−4969.

(28) Dohner, E. R.; Jaffe, A.; Bradshaw, L. R.; Karunadasa, H. I. Intrinsic White-Light Emission from Layered Hybrid Perovskites. *J. Am. Chem. Soc.* **2014**, *136*, 13154−13157.

(29) Wang, Y.; Song, L.; Chen, Y.; Huang, W. Emerging New-Generation Photodetectors Based on Low-Dimensional Halide Perovskites. *ACS Photonics* **2020**, *7*, 10−28.

(30) Chen, X.-G.; Song, X.-J.; Zhang, Z.-X.; Li, P.-F.; Ge, J.-Z.; Tang, Y.-Y.; Gao, J.-X.; Zhang, W.-Y.; Fu, D.-W.; You, Y.-M.; et al. Two-Dimensional Layered Perovskite Ferroelectric with Giant Piezoelectric Voltage Coefficient. *J. Am. Chem. Soc.* **2020**, *142*, 1077−1082.

(31) Xie, A.; Maddalena, F.; Witkowski, M. E.; Makowski, M.; Mahler, B.; Drozdowski, W.; Springham, S. V.; Coquet, P.; Dujardin, C.; Birowosuto, M. D.; et al. Library of Two-Dimensional Hybrid Lead Halide Perovskite Scintillator Crystals. *Chem. Mater.* **2020**, *32*, 8530−8539.

(32) Han, K.; Wei, Z.; Ye, X.; Li, B.; Wang, P.; Cai, H. A Lead Bromide Organic-Inorganic Hybrid Perovskite Material Showing Reversible Dual Phase Transition and Robust SHG Switching. *Dalton Trans* **2022**, *51*, 8273−8278.

(33) Yang, M.; Cheng, H.; Xu, Y.; Li, M.; Ai, Y. A Hybrid Organic-Inorganic Perovskite with Robust SHG Switching. *Chin. Chem. Lett.* **2022**, *33*, 2143−2146.

(34) Lun, M.-M.; Zhou, F.-L.; Fu, D.-W.; Ye, Q. Multi-Functional Hybrid Perovskites with Triple-Channel Switches and Optical Properties. *J. Mater. Chem. C* **2022**, *10*, 11371−11378.

(35) Li, H.-J.; Liu, Y.-L.; Chen, X.-G.; Gao, J.-X.; Wang, Z.-X.; Liao, W.-Q. High-Temperature Dielectric Switching and Photoluminescence in a Corrugated Lead Bromide Layer Hybrid Perovskite Semiconductor. *Inorg. Chem.* **2019**, *58*, 10357−10363.

(36) Ovčar, J.; Leung, T. L.; Grisanti, L.; Skoko, Z.; Vrankić, M.; Low, K.-H.; Wang, S.; You, P.-Y.; Ahn, H.; Lončarić, I.; et al. Mixed Halide Ordering as a Tool for the Stabilization of Ruddlesden-Popper Structures. *Chem. Mater.* **2022**, *34*, 4286−4297.

(37) Yangui, A.; Pillet, S.; Lusson, A.; Bendeif, E.-E.; Triki, S.; Abid, Y.; Boukheddaden, K. Control of the White-Light Emission in the Mixed Two-Dimensional Hybrid Perovskites $(C_6H_{11}NH_3)_2[PbBr_{4-x}I_x]$. *J. Alloys Compd.* **2017**, *699*, 1122−1133.

(38) Ma, D.; Fu, Y.; Dang, L.; Zhai, J.; Guzei, I. A.; Jin, S. Single-Crystal Microplates of Two-Dimensional Organic-Inorganic Lead Halide Layered Perovskites for Optoelectronics. *Nano Res.* **2017**, *10*, 2117−2129.

https://doi.org/10.1021/acs.chemrev.3c00532
Chem. Rev. 2024, 124, 2281−2326

(39) Cai, P.; Wang, X.; Seo, H. J.; Yan, X. Bluish-White-Light-Emitting Diodes Based on Two-Dimensional Lead Halide Perovskite $(C_6H_5C_2H_4NH_3)_2PbCl_2Br_2$. *Appl. Phys. Lett.* **2018**, *112*, No. 153901.
(40) Pareja-Rivera, C.; Morán-Muñoz, J. A.; Gómora-Figueroa, A. P.; Jancik, V.; Vargas, B.; Rodríguez-Hernández, J.; Solis-Ibarra, D. Optimizing Broadband Emission in 2D Halide Perovskites. *Chem. Mater.* **2022**, *34*, 9344−9349.
(41) Lin, Y. L.; Johnson, J. C. Interlayer Triplet Energy Transfer in Dion-Jacobson Two-Dimensional Lead Halide Perovskites Containing Naphthalene Diammonium Cations. *J. Phys. Chem. Lett.* **2021**, *12*, 4793−4798.
(42) Yan, L.; Jana, M. K.; Sercel, P. C.; Mitzi, D. B.; You, W. Alkyl-Aryl Cation Mixing in Chiral 2D Perovskites. *J. Am. Chem. Soc.* **2021**, *143*, 18114−18120.
(43) Guo, Y.-Y.; Yang, L.-J.; Biberger, S.; McNulty, J. A.; Li, T.; Schötz, K.; Panzer, F.; Lightfoot, P. Structural Diversity in Layered Hybrid Perovskites, A_2PbBr_4 or AA$'$PbBr4, Templated by Small Disc-Shaped Amines. *Inorg. Chem.* **2020**, *59*, 12858−12866.
(44) Guo, Y.-Y.; McNulty, J. A.; Mica, N. A.; Samuel, I. D. W.; Slawin, A. M. Z.; Bühl, M.; Lightfoot, P. Structure-Directing Effects in (110)-Layered Hybrid Perovskites Containing Two Distinct Organic Moieties. *Chem. Commun.* **2019**, *55*, 9935−9938.
(45) Stoumpos, C. C.; Cao, D. H.; Clark, D. J.; Young, J.; Rondinelli, J. M.; Jang, J. I.; Hupp, J. T.; Kanatzidis, M. G. Ruddlesden-Popper Hybrid Lead Iodide Perovskite 2D Homologous Semiconductors. *Chem. Mater.* **2016**, *28*, 2852−2867.
(46) Li, X.; Hoffman, J. M.; Kanatzidis, M. G. The 2D Halide Perovskite Rulebook: How the Spacer Influences Everything from the Structure to Optoelectronic Device Efficiency. *Chem. Rev.* **2021**, *121*, 2230−2291.
(47) Li, D.; Wu, W.; Han, S.; Liu, X.; Peng, Y.; Li, X.; Li, L.; Hong, M.; Luo, J. A Reduced-Dimensional Polar Hybrid Perovskite for Self-Powered Broad-Spectrum Photodetection. *Chem. Sci.* **2021**, *12*, 3050−3054.
(48) Li, X.; Dong, H.; Volonakis, G.; Stoumpos, C. C.; Even, J.; Katan, C.; Guo, P.; Kanatzidis, M. G. Ordered Mixed-Spacer 2D Bromide Perovskites and the Dual Role of 1,2,4-Triazolium Cation. *Chem. Mater.* **2022**, *34*, 6541−6552.
(49) Stoumpos, C. C.; Mao, L.; Malliakas, C. D.; Kanatzidis, M. G. Structure-Band Gap Relationships in Hexagonal Polytypes and Low-Dimensional Structures of Hybrid Tin Iodide Perovskites. *Inorg. Chem.* **2017**, *56*, 56−73.
(50) Zhang, Y.; Liu, Y.; Liu, S. F. Composition Engineering of Perovskite Single Crystals for High-Performance Optoelectronics. *Adv. Funct. Mater.* **2023**, *33*, No. 2210335.
(51) Kim, J. Y.; Lee, J.-W.; Jung, H. S.; Shin, H.; Park, N.-G. High-Efficiency Perovskite Solar Cells. *Chem. Rev.* **2020**, *120*, 7867−7918.
(52) Jin, R.-J.; Lou, Y.-H.; Wang, Z.-K. Doping Strategies for Promising Organic-Inorganic Halide Perovskites. *Small* **2023**, *19*, No. 2206581.
(53) Frost, J. M.; Butler, K. T.; Brivio, F.; Hendon, C. H.; van Schilfgaarde, M.; Walsh, A. Atomistic Origins of High-Performance in Hybrid Halide Perovskite Solar Cells. *Nano Lett.* **2014**, *14*, 2584−2590.
(54) Egger, D. A.; Rappe, A. M.; Kronik, L. Hybrid Organic-Inorganic Perovskites on the Move. *Acc. Chem. Res.* **2016**, *49*, 573−581.
(55) Herz, L. M. How Lattice Dynamics Moderate the Electronic Properties of Metal-Halide Perovskites. *J. Phys. Chem. Lett.* **2018**, *9*, 6853−6863.
(56) Frost, J. M.; Walsh, A. What Is Moving in Hybrid Halide Perovskite Solar Cells? *Acc. Chem. Res.* **2016**, *49*, 528−535.
(57) Liu, S.; Guo, R.; Xie, F. The Effects of Organic Cation Rotation in Hybrid Organic-Inorganic Perovskites: A Critical Review. *Mater. Des.* **2022**, *221*, No. 110951.
(58) Cowley, R. A.; Gvasaliya, S. N.; Lushnikov, S. G.; Roessli, B.; Rotaru, G. M. Relaxing with Relaxors: A Review of Relaxor Ferroelectrics. *Adv. Phys.* **2011**, *60*, 229−327.
(59) Vugmeister, B. E.; Glinchuk, M. D. Dipole Glass and Ferroelectricity in Random-Site Electric Dipole Systems. *Rev. Mod. Phys.* **1990**, *62*, 993−1026.
(60) Loidl, A. Orientational Glasses. *Annu. Rev. Phys. Chem.* **1989**, *40*, 29−60.
(61) Samara, G. A. The Relaxational Properties of Compositionally Disordered ABO_3 Perovskites. *J. Phys.: Condens. Matter* **2003**, *15*, R367.
(62) Bokov, A. A.; Ye, Z.-G. Recent Progress in Relaxor Ferroelectrics with Perovskite Structure. *J. Mater. Sci.* **2006**, *41*, 31−52.
(63) Ellis, C. L. C.; Javaid, H.; Smith, E. C.; Venkataraman, D. Hybrid Perovskites with Larger Organic Cations Reveal Autocatalytic Degradation Kinetics and Increased Stability under Light. *Inorg. Chem.* **2020**, *59*, 12176−12186.
(64) Hsiao, K.-C.; Jao, M.-H.; Tian, K.-Y.; Lin, T.-H.; Tran, D.-P.; Liao, H.-C.; Hou, C.-H.; Shyue, J.-J.; Wu, M.-C.; Su, W.-F. Acetamidinium Cation to Confer Ion Immobilization and Structure Stabilization of Organometal Halide Perovskite Toward Long Life and High-Efficiency p-i-n Planar Solar Cell via Air-Processable Method. *Solar RRL* **2020**, *4*, No. 2000197.
(65) Singh, P.; Mukherjee, R.; Avasthi, S. Acetamidinium-Substituted Methylammonium Lead Iodide Perovskite Solar Cells with Higher Open-Circuit Voltage and Improved Intrinsic Stability. *ACS Appl. Mater. Interfaces* **2020**, *12*, 13982−13987.
(66) Kim, J.; Hwang, T.; Lee, B.; Lee, S.; Park, K.; Park, H. H.; Park, B. An Aromatic Diamine Molecule as the A-Site Solute for Highly Durable and Efficient Perovskite Solar Cells. *Small Methods* **2019**, *3*, No. 1800361.
(67) Wang, Q.; Lin, F.; Chueh, C.-C.; Zhao, T.; Eslamian, M.; Jen, A. K.-Y. Enhancing Efficiency of Perovskite Solar Cells by Reducing Defects Through Imidazolium Cation Incorporation. *Mater. Today Energy* **2018**, *7*, 161−168.
(68) Shi, Z.; Zhang, Y.; Cui, C.; Li, B.; Zhou, W.; Ning, Z.; Mi, Q. Symmetrization of the Crystal Lattice of $MAPbI_3$ Boosts the Performance and Stability of Metal-Perovskite Photodiodes. *Adv. Mater.* **2017**, *29*, No. 1701656.
(69) Jodlowski, A. D.; Roldán-Carmona, C.; Grancini, G.; Salado, M.; Ralaiarisoa, M.; Ahmad, S.; Koch, N.; Camacho, L.; de Miguel, G.; Nazeeruddin, M. K. Large Guanidinium Cation Mixed with Methylammonium in Lead Iodide Perovskites for 19% Efficient Solar Cells. *Nat. Energy* **2017**, *2*, 972−979.
(70) Akbulatov, A. F.; Frolova, L. A.; Anokhin, D. V.; Gerasimov, K. L.; Dremova, N. N.; Troshin, P. A. Hydrazinium-Loaded Perovskite Solar Cells with Enhanced Performance and Stability. *J. Mater. Chem. A* **2016**, *4*, 18378−18382.
(71) Peng, W.; Miao, X.; Adinolfi, V.; Alarousu, E.; El Tall, O.; Emwas, A.-H.; Zhao, C.; Walters, G.; Liu, J.; Ouellette, O.; et al. Engineering of $CH_3NH_3PbI_3$ Perovskite Crystals by Alloying Large Organic Cations for Enhanced Thermal Stability and Transport Properties. *Angew. Chem., Int. Ed.* **2016**, *55*, 10686−10690.
(72) Leblanc, A.; Mercier, N.; Allain, M.; Dittmer, J.; Pauporté, T.; Fernandez, V.; Boucher, F.; Kepenekian, M.; Katan, C. Enhanced Stability and Band Gap Tuning of α-$[HC(NH_2)_2]PbI_3$ Hybrid Perovskite by Large Cation Integration. *ACS Appl. Mater. Interfaces* **2019**, *11*, 20743−20751.
(73) Kumar, G. S.; Sarkar, P. K.; Pradhan, B.; Hossain, M.; Rao, K. D. M.; Acharya, S. Large-Area Transparent Flexible Guanidinium Incorporated $MAPbI_3$ Microstructures for High-Performance Photodetectors with Enhanced Stability. *Nanoscale Horiz* **2020**, *5*, 696−704.
(74) Ray, A.; Martin-Garcia, B.; Moliterni, A.; Casati, N.; Boopathi, K. M.; Spirito, D.; Goldoni, L.; Prato, M.; Giacobbe, C.; Giannini, C.; Di Stasio, F.; Krahne, R.; Manna, L.; Abdelhady, A. L. Mixed Dimethylammonium/Methylammonium Lead Halide Perovskite Crystals for Improved Structural Stability and Enhanced Photodetection. *Adv. Mater.* **2022**, *34*, No. 2106160.
(75) Kubicki, D. J.; Prochowicz, D.; Hofstetter, A.; Saski, M.; Yadav, P.; Bi, D.; Pellet, N.; Lewiński, J.; Zakeeruddin, S. M.; Grätzel, M.; et al. Formation of Stable Mixed Guanidinium-Methylammonium

https://doi.org/10.1021/acs.chemrev.3c00532
Chem. Rev. 2024, 124, 2281−2326

Phases with Exceptionally Long Carrier Lifetimes for High-Efficiency Lead Iodide-Based Perovskite Photovoltaics. *J. Am. Chem. Soc.* **2018**, *140*, 3345−3351.
(76) Pellet, N.; Gao, P.; Gregori, G.; Yang, T.-Y.; Nazeeruddin, M. K.; Maier, J.; Grätzel, M. Mixed-Organic-Cation Perovskite Photovoltaics for Enhanced Solar-Light Harvesting. *Angew. Chem., Int. Ed.* **2014**, *53*, 3151−3157.
(77) Wu, S.; Li, Z.; Zhang, J.; Liu, T.; Zhu, Z.; Jen, A. K.-Y. Efficient Large Guanidinium Mixed Perovskite Solar Cells with Enhanced Photovoltage and Low Energy Losses. *Chem. Commun.* **2019**, *55*, 4315−4318.
(78) Shao, F.; Qin, P.; Wang, D.; Zhang, G.; Wu, B.; He, J.; Peng, W.; Sum, T. C.; Wang, D.; Huang, F. Enhanced Photovoltaic Performance and Thermal Stability of $CH_3NH_3PbI_3$ Perovskite through Lattice Symmetrization. *ACS Appl. Mater. Interfaces* **2019**, *11*, 740−746.
(79) Kim, G.; Min, H.; Lee, K. S.; Lee, D. Y.; Yoon, S. M.; Seok, S. I. Impact of Strain Relaxation on Performance of α-Formamidinium Lead Iodide Perovskite Solar Cells. *Science* **2020**, *370*, 108−112.
(80) Gao, L.; Li, X.; Liu, Y.; Fang, J.; Huang, S.; Spanopoulos, I.; Li, X.; Wang, Y.; Chen, L.; Yang, G.; et al. Incorporated Guanidinium Expands the $CH_3NH_3PbI_3$ Lattice and Enhances Photovoltaic Performance. *ACS Appl. Mater. Interfaces* **2020**, *12*, 43885−43891.
(81) Huang, Y.; Qiao, L.; Jiang, Y.; He, T.; Long, R.; Yang, F.; Wang, L.; Lei, X.; Yuan, M.; Chen, J. A-site Cation Engineering for Highly Efficient $MAPbI_3$ Single-Crystal X-ray Detector. *Angew. Chem., Int. Ed.* **2019**, *58*, 17834−17842.
(82) Zhang, X.; Xiao, S.; Li, R.; He, T.; Xing, G.; Chen, R. Influence of Mixed Organic Cations on the Nonlinear Optical Properties of Lead Tri-Iodide Perovskites. *Photon. Res.* **2020**, *8*, A25−A30.
(83) Choi, H.; Jeong, J.; Kim, H.-B.; Kim, S.; Walker, B.; Kim, G.-H.; Kim, J. Y. Cesium-Doped Methylammonium Lead Iodide Perovskite Light Absorber for Hybrid Solar Cells. *Nano Energy* **2014**, *7*, 80−85.
(84) Liu, D.; Li, Q.; Wu, K. Ethylammonium as an Alternative Cation for Efficient Perovskite Solar Cells from First-Principles Calculations. *RSC Adv.* **2019**, *9*, 7356−7361.
(85) Gholipour, S.; Ali, A. M.; Correa-Baena, J.-P.; Turren-Cruz, S.-H.; Tajabadi, F.; Tress, W.; Taghavinia, N.; Gratzel, M.; Abate, A.; De Angelis, F.; Gaggioli, C. A.; Mosconi, E.; Hagfeldt, A.; Saliba, M. Globularity-Selected Large Molecules for a New Generation of Multication Perovskites. *Adv. Mater.* **2017**, *29*, No. 1702005.
(86) Anelli, C.; Chierotti, M. R.; Bordignon, S.; Quadrelli, P.; Marongiu, D.; Bongiovanni, G.; Malavasi, L. Investigation of Dimethylammonium Solubility in $MAPbBr_3$ Hybrid Perovskite: Synthesis, Crystal Structure, and Optical Properties. *Inorg. Chem.* **2019**, *58*, 944−949.
(87) Huang, J.; Xu, P.; Liu, J.; You, X.-Z. Sequential Introduction of Cations Deriving Large-Grain $Cs_xFA_{1-x}PbI_3$ Thin Film for Planar Hybrid Solar Cells: Insight into Phase-Segregation and Thermal-Healing Behavior. *Small* **2017**, *13*, No. 1603225.
(88) Francisco-López, A.; Charles, B.; Alonso, M. I.; Garriga, M.; Campoy-Quiles, M.; Weller, M. T.; Goñi, A. R. Phase Diagram of Methylammonium/Formamidinium Lead Iodide Perovskite Solid Solutions from Temperature-Dependent Photoluminescence and Raman Spectroscopies. *J. Phys. Chem. C* **2020**, *124*, 3448−3458.
(89) Parrott, E. S.; Green, T.; Milot, R. L.; Johnston, M. B.; Snaith, H. J.; Herz, L. M. Interplay of Structural and Optoelectronic Properties in Formamidinium Mixed Tin-Lead Triiodide Perovskites. *Adv. Funct. Mater.* **2018**, *28*, No. 1802803.
(90) Wang, C.; Song, Z.; Li, C.; Zhao, D.; Yan, Y. Low-Bandgap Mixed Tin-Lead Perovskites and Their Applications in All-Perovskite Tandem Solar Cells. *Adv. Funct. Mater.* **2019**, *29*, No. 1808801.
(91) Tong, J.; Song, Z.; Kim, D. H.; Chen, X.; Chen, C.; Palmstrom, A. F.; Ndione, P. F.; Reese, M. O.; Dunfield, S. P.; Reid, O. G.; et al. Carrier Lifetimes of > 1μs in Sn-Pb Perovskites Enable Efficient All-Perovskite Tandem Solar Cells. *Science* **2019**, *364*, 475−479.
(92) Savill, K. J.; Ulatowski, A. M.; Herz, L. M. Optoelectronic Properties of Tin-Lead Halide Perovskites. *ACS Energy Lett.* **2021**, *6*, 2413−2426.
(93) Stoumpos, C. C.; Malliakas, C. D.; Kanatzidis, M. G. Semiconducting Tin and Lead Iodide Perovskites with Organic Cations: Phase Transitions, High Mobilities, and Near-Infrared Photoluminescent Properties. *Inorg. Chem.* **2013**, *52*, 9019−9038.
(94) Hao, F.; Stoumpos, C. C.; Chang, R. P. H.; Kanatzidis, M. G. Anomalous Band Gap Behavior in Mixed Sn and Pb Perovskites Enables Broadening of Absorption Spectrum in Solar Cells. *J. Am. Chem. Soc.* **2014**, *136*, 8094−8099.
(95) Prasanna, R.; Gold-Parker, A.; Leijtens, T.; Conings, B.; Babayigit, A.; Boyen, H.-G.; Toney, M. F.; McGehee, M. D. Band Gap Tuning via Lattice Contraction and Octahedral Tilting in Perovskite Materials for Photovoltaics. *J. Am. Chem. Soc.* **2017**, *139*, 11117−11124.
(96) Senanayak, S. P.; Dey, K.; Shivanna, R.; Li, W.; Ghosh, D.; Zhang, Y.; Roose, B.; Zelewski, S. J.; Andaji-Garmaroudi, Z.; Wood, W.; et al. Charge Transport in Mixed Metal Halide Perovskite Semiconductors. *Nat. Mater.* **2023**, *22*, 216−224.
(97) Zhao, D.; Yu, Y.; Wang, C.; Liao, W.; Shrestha, N.; Grice, C. R.; Cimaroli, A. J.; Guan, L.; Ellingson, R. J.; Zhu, K.; Zhao, X.; Xiong, R.-G.; Yan, Y. Low-Bandgap Mixed Tin-Lead Iodide Perovskite Absorbers with Long Carrier Lifetimes for All-Perovskite Tandem Solar Cells. *Nat. Energy* **2017**, *2*, No. 17018.
(98) Elsayed, M. R. A.; Elseman, A. M.; Abdelmageed, A. A.; Hashem, H. M.; Hassen, A. Green and Cost-Effective Morter Grinding Synthesis of Bismuth-Doped Halide Perovskites as Efficient Absorber Materials. *J. Mater. Sci.: Mater. Electron* **2023**, *34*, 194.
(99) Wieghold, S.; Luo, Y.; Bieber, A. S.; Lackner, J.; Shirato, N.; VanOrman, Z. A.; Rosenmann, D.; Nienhaus, K.; Lai, B.; Nienhaus, G. U.; et al. Impact of Transition Metal Doping on the Structural and Optical Properties of Halide Perovskites. *Chem. Mater.* **2021**, *33*, 6099−6107.
(100) Zhou, Y.; Chen, J.; Bakr, O. M.; Sun, H.-T. Metal-Doped Lead Halide Perovskites: Synthesis, Properties, and Optoelectronic Applications. *Chem. Mater.* **2018**, *30*, 6589−6613.
(101) Swarnkar, A.; Mir, W. J.; Nag, A. Can B-Site Doping or Alloying Improve Thermal- and Phase-Stability of All-Inorganic $CsPbX_3$ (X = Cl, Br, I) Perovskites? *ACS Energy Lett.* **2018**, *3*, 286−289.
(102) Kubicki, D. J.; Prochowicz, D.; Hofstetter, A.; Péchy, P.; Zakeeruddin, S. M.; Grätzel, M.; Emsley, L. Cation Dynamics in Mixed-Cation $(MA)_x(FA)_{1-x}PbI_3$ Hybrid Perovskites from Solid-State NMR. *J. Am. Chem. Soc.* **2017**, *139*, 10055−10061.
(103) Liu, F.; Zhang, Y.; Ding, C.; Kawabata, K.; Yoshihara, Y.; Toyoda, T.; Hayase, S.; Minemoto, T.; Wang, R.; Shen, Q. Trioctylphosphine Oxide Acts as Alkahest for SnX_2/PbX_2: A General Synthetic Route to Perovskite $ASn_xPb_{1-x}X_3$ (A = Cs, FA, MA; X = Cl, Br, I) Quantum Dots. *Chem. Mater.* **2020**, *32*, 1089−1100.
(104) Eperon, G. E.; Leijtens, T.; Bush, K. A.; Prasanna, R.; Green, T.; Wang, J. T.-W.; McMeekin, D. P.; Volonakis, G.; Milot, R. L.; May, R.; et al. Perovskite-Perovskite Tandem Photovoltaics with Optimized Band Gaps. *Science* **2016**, *354*, 861−865.
(105) Bush, K. A.; Palmstrom, A. F.; Yu, Z. J.; Boccard, M.; Cheacharoen, R.; Mailoa, J. P.; McMeekin, D. P.; Hoye, R. L. Z.; Bailie, C. D.; Leijtens, T.; Peters, I. M.; Minichetti, M. C.; Rolston, N.; Prasanna, R.; Sofia, S.; Harwood, D.; Ma, W.; Moghadam, F.; Snaith, H. J.; Buonassisi, T.; Holman, Z. C.; Bent, S. F.; McGehee, M. D. 23.6%-Efficient Monolithic Perovskite/Silicon Tandem Solar Cells with Improved Stability. *Nat. Energy* **2017**, *2*, No. 17009.
(106) Koh, T. M.; Fu, K.; Fang, Y.; Chen, S.; Sum, T. C.; Mathews, N.; Mhaisalkar, S. G.; Boix, P. P.; Baikie, T. Formamidinium-Containing Metal-Halide: An Alternative Material for Near-IR Absorption Perovskite Solar Cells. *J. Phys. Chem. C* **2014**, *118*, 16458−16462.
(107) Eperon, G. E.; Paternò, G. M.; Sutton, R. J.; Zampetti, A.; Haghighirad, A. A.; Cacialli, F.; Snaith, H. J. Inorganic Caesium Lead Iodide Perovskite Solar Cells. *J. Mater. Chem. A* **2015**, *3*, 19688−19695.

https://doi.org/10.1021/acs.chemrev.3c00532
Chem. Rev. 2024, 124, 2281−2326

(108) Binek, A.; Hanusch, F. C.; Docampo, P.; Bein, T. Stabilization of the Trigonal High-Temperature Phase of Formamidinium Lead Iodide. *J. Phys. Chem. Lett.* **2015**, *6*, 1249−1253.
(109) Merten, L.; Hinderhofer, A.; Baumeler, T.; Arora, N.; Hagenlocher, J.; Zakeeruddin, S. M.; Dar, M. I.; Grätzel, M.; Schreiber, F. Quantifying Stabilized Phase Purity in Formamidinium-Based Multiple-Cation Hybrid Perovskites. *Chem. Mater.* **2021**, *33*, 2769−2776.
(110) Li, Z.; Yang, M.; Park, J.-S.; Wei, S.-H.; Berry, J. J.; Zhu, K. Stabilizing Perovskite Structures by Tuning Tolerance Factor: Formation of Formamidinium and Cesium Lead Iodide Solid-State Alloys. *Chem. Mater.* **2016**, *28*, 284−292.
(111) Jeon, N. J.; Noh, J. H.; Yang, W. S.; Kim, Y. C.; Ryu, S.; Seo, J.; Seok, S. I. Compositional Engineering of Perovskite Materials for High-Performance Solar Cells. *Nature* **2015**, *517*, 476−480.
(112) Baumeler, T.; Arora, N.; Hinderhofer, A.; Akin, S.; Greco, A.; Abdi-Jalebi, M.; Shivanna, R.; Uchida, R.; Liu, Y.; Schreiber, F.; et al. Minimizing the Trade-Off between Photocurrent and Photovoltage in Triple-Cation Mixed-Halide Perovskite Solar Cells. *J. Phys. Chem. Lett.* **2020**, *11*, 10188−10195.
(113) McMeekin, D. P.; Sadoughi, G.; Rehman, W.; Eperon, G. E.; Saliba, M.; Hörantner, M. T.; Haghighirad, A.; Sakai, N.; Korte, L.; Rech, B.; et al. A Mixed-Cation Lead Mixed-Halide Perovskite Absorber for Tandem Solar Cells. *Science* **2016**, *351*, 151−155.
(114) Min, H.; Kim, M.; Lee, S.-U.; Kim, H.; Kim, G.; Choi, K.; Lee, J. H.; Seok, S. I. Efficient, Stable Solar Cells by using Inherent Bandgap of α-Phase Formamidinium Lead Iodide. *Science* **2019**, *366*, 749−753.
(115) Schmidt-Mende, L.; Dyakonov, V.; Olthof, S.; Unlu, F.; Le, K. M. T.; Mathur, S.; Karabanov, A. D.; Lupascu, D. C.; Herz, L. M.; Hinderhofer, A.; Schreiber, F.; Chernikov, A.; Egger, D. A.; Shargaieva, O.; Cocchi, C.; Unger, E.; Saliba, M.; Byranvand, M. M.; Kroll, M.; Nehm, F.; Leo, K.; Redinger, A.; Hocker, J.; Kirchartz, T.; Warby, J.; Gutierrez-Partida, E.; Neher, D.; Stolterfoht, M.; Wurfel, U.; Unmussig, M.; Herterich, J.; Baretzky, C.; Mohanraj, J.; Thelakkat, M.; Maheu, C.; Jaegermann, W.; Mayer, T.; Rieger, J.; Fauster, T.; Niesner, D.; Yang, F.; Albrecht, S.; Riedl, T.; Fakharuddin, A.; Vasilopoulou, M.; Vaynzof, Y.; Moia, D.; Maier, J.; Franckevicius, M.; Gulbinas, V.; Kerner, R. A.; Zhao, L.; Rand, B. P.; Gluck, N.; Bein, T.; Matteocci, F.; Castriotta, L. A.; Di Carlo, A.; Scheffler, M.; Draxl, C. Roadmap on Organic-Inorganic Hybrid Perovskite Semiconductors and Devices. *APL Mater.* **2021**, *9*, No. 109202.
(116) Eperon, G. E.; Stranks, S. D.; Menelaou, C.; Johnston, M. B.; Herz, L. M.; Snaith, H. J. Formamidinium Lead Trihalide: a Broadly Tunable Perovskite for Efficient Planar Heterojunction Solar Cells. *Energy Environ. Sci.* **2014**, *7*, 982−988.
(117) Rybin, N.; Ghosh, D.; Tisdale, J.; Shrestha, S.; Yoho, M.; Vo, D.; Even, J.; Katan, C.; Nie, W.; Neukirch, A. J.; et al. Effects of Chlorine Mixing on Optoelectronics, Ion Migration, and Gamma-Ray Detection in Bromide Perovskites. *Chem. Mater.* **2020**, *32*, 1854−1863.
(118) Drozdowski, D.; Gagor, A.; Stefanska, D.; Zareba, J. K.; Fedoruk, K.; Maczka, M.; Sieradzki, A. Three-Dimensional Methylhydrazinium Lead Halide Perovskites: Structural Changes and Effects on Dielectric, Linear, and Nonlinear Optical Properties Entailed by the Halide Tuning. *J. Phys. Chem. C* **2022**, *126*, 1600−1610.
(119) Chen, Y.; Motti, S. G.; Oliver, R. D. J.; Wright, A. D.; Snaith, H. J.; Johnston, M. B.; Herz, L. M.; Filip, M. R. Optoelectronic Properties of Mixed Iodide-Bromide Perovskites from First-Principles Computational Modeling and Experiment. *J. Phys. Chem. Lett.* **2022**, *13*, 4184−4192.
(120) Wang, H.; Ling, F.; Luo, C.; Li, D.; Xiao, Y.; Chang, Z.; Xu, Z.; Zeng, Y.; Wang, W.; Yao, J. Active Terahertz Modulator Based on Optically Controlled Organometal Halide Perovskite $MAPbI_2Br$. *Appl. Opt.* **2022**, *61*, 1171−1176.
(121) Suárez, I.; Vallés-Pelarda, M.; Gualdrón-Reyes, A. F.; Mora-Seró, I.; Ferrando, A.; Michinel, H.; Salgueiro, J. R.; Pastor, J. P. M. Outstanding Nonlinear Optical Properties of Methylammonium- and Cs− PbX_3 (X = Br, I, and Br-I) Perovskites: Polycrystalline Thin Films and Nanoparticles. *APL Mater.* **2019**, *7*, No. 041106.
(122) Wei, Q.; Liang, H.; Haruta, Y.; Saidaminov, M.; Mi, Q.; Saliba, M.; Cui, G.; Ning, Z. From Tetragonal to Cubic: Perovskite Phase Structure Evolution for High-Performance Solar Cells. *Sci. Bull.* **2023**, *68*, 141−145.
(123) He, J.; Li, T.; Liu, X.; Su, H.; Ku, Z.; Zhong, J.; Huang, F.; Peng, Y.; Cheng, Y.-B. Influence of Phase Transition on Stability of Perovskite Solar Cells under Thermal Cycling Conditions. *Sol. Energy* **2019**, *188*, 312−317.
(124) Shao, D.-S.; Sang, L.; Kong, Y.-R.; Deng, Z.-R.; Luo, H.-B.; Tian, Z.-F.; Ren, X.-M. Tunable Thermotropic Phase Transition Triggering Large Dielectric Response and Superionic Conduction in Lead Halide Perovskites. *Inorg. Chem. Front.* **2022**, *9*, 5653−5662.
(125) Yu, J.; Kong, J.; Hao, W.; Guo, X.; He, H.; Leow, W. R.; Liu, Z.; Cai, P.; Qian, G.; Li, S.; Chen, X.; Chen, X. Broadband Extrinsic Self-Trapped Exciton Emission in Sn-Doped 2D Lead-Halide Perovskites. *Adv. Mater.* **2019**, *31*, No. 1806385.
(126) Li, T.; Chen, X.; Wang, X.; Lu, H.; Yan, Y.; Beard, M. C.; Mitzi, D. B. Origin of Broad-Band Emission and Impact of Structural Dimensionality in Tin-Alloyed Ruddlesden-Popper Hybrid Lead Iodide Perovskites. *ACS Energy Lett.* **2020**, *5*, 347−352.
(127) Sui, S.; Zhou, J.; Wang, A.; Hu, G.; Meng, W.; Wang, C.; Liu, Y.; Wu, J.; Deng, Z. Synthesis of Two-Dimensional Phenylethylamine Tin-Lead Halide Perovskites with Bandgap Bending Behavior. *Nanoscale Adv.* **2021**, *3*, 3875−3880.
(128) Biswas, A.; Bakthavatsalam, R.; Kundu, J. Efficient Exciton to Dopant Energy Transfer in Mn^{2+}-Doped $(C_4H_9NH_3)_2PbBr_4$ Two-Dimensional (2D) Layered Perovskites. *Chem. Mater.* **2017**, *29*, 7816−7825.
(129) Liao, J.-F.; Zhang, Z.; Wang, B.; Tang, Z.; Xing, G. Full-Color-Tunable Phosphorescence of Antimony-Doped Lead Halide Single Crystal. *npj Flexible Electron* **2022**, *6*, 57.
(130) Wu, Z.; Zhang, W.; Ye, H.; Yao, Y.; Liu, X.; Li, L.; Ji, C.; Luo, J. Bromine-Substitution-Induced High-Tc Two-Dimensional Bilayered Perovskite Photoferroelectric. *J. Am. Chem. Soc.* **2021**, *143*, 7593−7598.
(131) Park, I.-H.; Kwon, K. C.; Zhu, Z.; Wu, X.; Li, R.; Xu, Q.-H.; Loh, K. P. Self-Powered Photodetector Using Two-Dimensional Ferroelectric Dion-Jacobson Hybrid Perovskites. *J. Am. Chem. Soc.* **2020**, *142*, 18592−18598.
(132) Zhang, Q.; Solanki, A.; Parida, K.; Giovanni, D.; Li, M.; Jansen, T. L. C.; Pshenichnikov, M. S.; Sum, T. C. Tunable Ferroelectricity in Ruddlesden-Popper Halide Perovskites. *ACS Appl. Mater. Interfaces* **2019**, *11*, 13523−13532.
(133) Han, S.; Liu, X.; Liu, Y.; Xu, Z.; Li, Y.; Hong, M.; Luo, J.; Sun, Z. High-Temperature Antiferroelectric of Lead Iodide Hybrid Perovskites. *J. Am. Chem. Soc.* **2019**, *141*, 12470−12474.
(134) Tang, L.; Han, S.; Ma, Y.; Liu, Y.; Hua, L.; Xu, H.; Guo, W.; Wang, B.; Sun, Z.; Luo, J. Giant Near-Room-Temperature Pyroelectric Figures-of-Merit Originating from Unusual Dielectric Bistability of Two-Dimensional Perovskite Ferroelectric Crystals. *Chem. Mater.* **2022**, *34*, 8898−8904.
(135) Ko, B. A.; Berry, K.; Qin, Z.; Sokolov, A. V.; Hu, J.; Scully, M. O.; Bao, J.; Zhang, Z. Resonant Degenerate Four-Wave Mixing at the Defect Energy Levels of 2D Organic-Inorganic Hybrid Perovskite Crystals. *ACS Appl. Mater. Interfaces* **2021**, *13*, 57075−57083.
(136) Leung, T. L.; Tam, H. W.; Liu, F.; Lin, J.; Ng, A. M. C.; Chan, W. K.; Chen, W.; He, Z.; Loncaric, I.; Grisanti, L.; Ma, C.; Wong, K. S.; Lau, Y. S.; Zhu, F.; Skoko, Z.; Popovic, J.; Djurisic, A. B. Mixed Spacer Cation Stabilization of Blue-Emitting n = 2 Ruddlesden-Popper Organic-Inorganic Halide Perovskite Films. *Adv. Opt. Mater.* **2020**, *8*, No. 1901679.
(137) Shi, J.; Jin, X.; Wu, Y.; Shao, M. Mixed Bulky Cations for Efficient and Stable Ruddlesden-Popper Perovskite Solar Cells. *APL Mater.* **2020**, *8*, No. 101102.
(138) Mao, L.; Guo, P.; Kepenekian, M.; Spanopoulos, I.; He, Y.; Katan, C.; Even, J.; Schaller, R. D.; Seshadri, R.; Stoumpos, C. C.; et al. Organic Cation Alloying on Intralayer A and Interlayer A' sites

https://doi.org/10.1021/acs.chemrev.3c00532
Chem. Rev. 2024, 124, 2281−2326

in 2D Hybrid Dion-Jacobson Lead Bromide Perovskites (A')(A)-Pb2Br7. *J. Am. Chem. Soc.* **2020**, *142*, 8342−8351.
(139) Qin, X.; Liu, F.; Leung, T. L.; Sun, W.; Chan, C. C. S.; Wong, K. S.; Kanižaj, L.; Popović, J.; Djurišić, A. B. Compositional Optimization of Mixed Cation Dion-Jacobson Perovskites for Efficient Green Light Emission. *J. Mater. Chem. C* **2021**, *10*, 108−114.
(140) Fu, Y.; Jiang, X.; Li, X.; Traore, B.; Spanopoulos, I.; Katan, C.; Even, J.; Kanatzidis, M. G.; Harel, E. Cation Engineering in Two-Dimensional Ruddlesden-Popper Lead Iodide Perovskites with Mixed Large A-Site Cations in the Cages. *J. Am. Chem. Soc.* **2020**, *142*, 4008−4021.
(141) Ramos-Terrón, S.; Jodlowski, A. D.; Verdugo-Escamilla, C.; Camacho, L.; de Miguel, G. Relaxing the Goldschmidt Tolerance Factor: Sizable Incorporation of the Guanidinium Cation into a Two-Dimensional Ruddlesden-Popper Perovskite. *Chem. Mater.* **2020**, *32*, 4024−4037.
(142) Ke, W.; Chen, C.; Spanopoulos, I.; Mao, L.; Hadar, I.; Li, X.; Hoffman, J. M.; Song, Z.; Yan, Y.; Kanatzidis, M. G. Narrow-Bandgap Mixed Lead/Tin-Based 2D Dion-Jacobson Perovskites Boost the Performance of Solar Cells. *J. Am. Chem. Soc.* **2020**, *142*, 15049−15057.
(143) Ramirez, D.; Schutt, K.; Wang, Z.; Pearson, A. J.; Ruggeri, E.; Snaith, H. J.; Stranks, S. D.; Jaramillo, F. Layered Mixed Tin-Lead Hybrid Perovskite Solar Cells with High Stability. *ACS Energy Lett.* **2018**, *3*, 2246−2251.
(144) Vashishtha, P.; Ng, M.; Shivarudraiah, S. B.; Halpert, J. E. High Efficiency Blue and Green Light-Emitting Diodes Using Ruddlesden-Popper Inorganic Mixed Halide Perovskites with Butylammonium Interlayers. *Chem. Mater.* **2019**, *31*, 83−89.
(145) Toso, S.; Gushchina, I.; Oliver, A. G.; Manna, L.; Kuno, M. Are Mixed-Halide Ruddlesden-Popper Perovskites Really Mixed? *ACS Energy Lett.* **2022**, *7*, 4242−4247.
(146) Zhang, W.; Xiong, R.-G. Ferroelectric Metal-Organic Frameworks. *Chem. Rev.* **2012**, *112*, 1163−1195.
(147) Kleemann, W. Random Fields in Dipolar Glasses and Relaxors. *J. Non-Cryst. Solids* **2002**, *307*−*310*, 66−72.
(148) Höchli, U.; Knorr, K.; Loidl, A. Orientational Glasses. *Adv. Phys.* **1990**, *39*, 405−615.
(149) Sarkar, S.; Ren, X.; Otsuka, K. Evidence for Strain Glass in the Ferroelastic-Martensitic System $Ti_{50-x}Ni_{50+x}$. *Phys. Rev. Lett.* **2005**, *95*, No. 205702.
(150) Kleemann, W. Random Fields in Relaxor Ferroelectrics - a Jubilee Review. *J. Adv. Dielectr.* **2012**, *02*, No. 1241001.
(151) Grigalaitis, R.; Banys, J.; Kania, A.; Slodczyk, A. Distribution of Relaxation Times in PMN Single Crystal. *J. Phys. IV France* **2005**, *128*, 127−131.
(152) Jeong, I.-K.; Darling, T. W.; Lee, J. K.; Proffen, T.; Heffner, R. H.; Park, J. S.; Hong, K. S.; Dmowski, W.; Egami, T. Direct Observation of the Formation of Polar Nanoregions in $Pb(Mg_{1/3}Nb_{2/3})O_3$ Using Neutron Pair Distribution Function Analysis. *Phys. Rev. Lett.* **2005**, *94*, No. 147602.
(153) Banys, J.; Klimm, C.; Völkel, G.; Böttcher, R.; Bauch, H.; Klöpperpieper, A. Proton Glass Behaviour in a Solid Solution of Irradiated Betaine $Phosphate_{0.15}$ Betaine $Phosphite_{0.85}$. *J. Phys.: Condens. Matter* **1996**, *8*, L245.
(154) Samara, G. A. Pressure and Temperature Dependence of the Dielectric Properties and Phase Transitions of the Ferroelectric Perovskites: $PbTiO_3$ and $BaTiO_3$. *Ferroelectrics* **1971**, *2*, 277−289.
(155) Levstik, A.; Kutnjak, Z.; Filipič, C.; Pirc, R. Glassy Freezing in Relaxor Ferroelectric Lead Magnesium Niobate. *Phys. Rev. B* **1998**, *57*, 11204−11211.
(156) Courtens, E. Vogel-Fulcher Scaling of the Susceptibility in a Mixed-Crystal Proton Glass. *Phys. Rev. Lett.* **1984**, *52*, 69−72.
(157) Tachibana, M.; Takayama-Muromachi, E. Thermal Conductivity and Heat Capacity of the Relaxor Ferroelectric $[PbMg_{1/3}Nb_{2/3}O_3]_{1-x}[PbTiO3]_x$. *Phys. Rev. B* **2009**, *79*, No. 100104.
(158) Yu, S.; Li, L.; Zhang, W.; Sun, Z.; Dong, H. Multilayer Thin Films with Compositional $PbZr_{0.52}Ti_{0.48}O_3/Bi_{1.5}Zn_{1.0}Nb_{1.5}O_7$ Layers for Tunable Applications. *Sci. Rep.* **2015**, *5*, No. 10173.
(159) Park, S.-E.; Shrout, T. R. Ultrahigh Strain and Piezoelectric Behavior in Relaxor Based Ferroelectric Single Crystals. *J. Appl. Phys.* **1997**, *82*, 1804−1811.
(160) Zhang, L.; Zhao, C.; Zheng, T.; Wu, J. Large Electrocaloric Effect in $(Bi_{0.5}Na_{0.5})TiO_3$-Based Relaxor Ferroelectrics. *ACS Appl. Mater. Interfaces* **2020**, *12*, 33934−33940.
(161) Ptak, M.; Sieradzki, A.; Šimėnas, M.; Maczka, M. Molecular Spectroscopy of Hybrid Organic-Inorganic Perovskites and Related Compounds. *Coord. Chem. Rev.* **2021**, *448*, No. 214180.
(162) Weber, O. J.; Charles, B.; Weller, M. T. Phase Behaviour and Composition in the Formamidinium-Methylammonium Hybrid Lead Iodide Perovskite Solid Solution. *J. Mater. Chem. A* **2016**, *4*, 15375−15382.
(163) Mozur, E. M.; Maughan, A. E.; Cheng, Y.; Huq, A.; Jalarvo, N.; Daemen, L. L.; Neilson, J. R. Orientational Glass Formation in Substituted Hybrid Perovskites. *Chem. Mater.* **2017**, *29*, 10168−10177.
(164) Simenas, M.; Balciunas, S.; Wilson, J. N.; Svirskas, S.; Kinka, M.; Garbaras, A.; Kalendra, V.; Gagor, A.; Szewczyk, D.; Sieradzki, A.; Maczka, M.; Samulionis, V.; Walsh, A.; Grigalaitis, R.; Banys, J. Suppression of Phase Transitions and Glass Phase Signatures in Mixed Cation Halide Perovskites. *Nat. Commun.* **2020**, *11*, 5103.
(165) Simenas, M.; Balciunas, S.; Svirskas, S.; Kinka, M.; Ptak, M.; Kalendra, V.; Gagor, A.; Szewczyk, D.; Sieradzki, A.; Grigalaitis, R.; Walsh, A.; Maczka, M.; Banys, J. Phase Diagram and Cation Dynamics of Mixed $MA_{1-x}FA_xPbBr_3$ Hybrid Perovskites. *Chem. Mater.* **2021**, *33*, 5926−5934.
(166) Simenas, M.; Balciunas, S.; Gagor, A.; Pieniazek, A.; Tolborg, K.; Kinka, M.; Klimavicius, V.; Svirskas, S.; Kalendra, V.; Ptak, M.; Szewczyk, D.; Herman, A. P.; Kudrawiec, R.; Sieradzki, A.; Grigalaitis, R.; Walsh, A.; Maczka, M.; Banys, J. Mixology of $MA_{1-x}EA_xPbI_3$ Hybrid Perovskites: Phase Transitions, Cation Dynamics, and Photoluminescence. *Chem. Mater.* **2022**, *34*, 10104−10112.
(167) Weller, M. T.; Weber, O. J.; Henry, P. F.; Di Pumpo, A. M.; Hansen, T. C. Complete Structure and Cation Orientation in the Perovskite Photovoltaic Methylammonium Lead Iodide Between 100 and 352 K. *Chem. Commun.* **2015**, *51*, 4180−4183.
(168) López, C. A.; Martínez-Huerta, M. V.; Alvarez-Galván, M. C.; Kayser, P.; Gant, P.; Castellanos-Gomez, A.; Fernández-Díaz, M. T.; Fauth, F.; Alonso, J. A. Elucidating the Methylammonium (MA) Conformation in $MAPbBr_3$ Perovskite with Application in Solar Cells. *Inorg. Chem.* **2017**, *56*, 14214−14219.
(169) Yang, B.; Ming, W.; Du, M.-H.; Keum, J. K.; Puretzky, A. A.; Rouleau, C. M.; Huang, J.; Geohegan, D. B.; Wang, X.; Xiao, K. Real-Time Observation of Order-Disorder Transformation of Organic Cations Induced Phase Transition and Anomalous Photoluminescence in Hybrid Perovskites. *Adv. Mater.* **2018**, *30*, No. 1705801.
(170) Schueller, E. C.; Laurita, G.; Fabini, D. H.; Stoumpos, C. C.; Kanatzidis, M. G.; Seshadri, R. Crystal Structure Evolution and Notable Thermal Expansion in Hybrid Perovskites Formamidinium Tin Iodide and Formamidinium Lead Bromide. *Inorg. Chem.* **2018**, *57*, 695−701.
(171) Charles, B.; Weller, M. T.; Rieger, S.; Hatcher, L. E.; Henry, P. F.; Feldmann, J.; Wolverson, D.; Wilson, C. C. Phase Behavior and Substitution Limit of Mixed Cesium-Formamidinium Lead Triiodide Perovskites. *Chem. Mater.* **2020**, *32*, 2282−2291.
(172) Mozur, E. M.; Hope, M. A.; Trowbridge, J. C.; Halat, D. M.; Daemen, L. L.; Maughan, A. E.; Prisk, T. R.; Grey, C. P.; Neilson, J. R. Cesium Substitution Disrupts Concerted Cation Dynamics in Formamidinium Hybrid Perovskites. *Chem. Mater.* **2020**, *32*, 6266−6277.
(173) Krogstad, M. J.; Gehring, P. M.; Rosenkranz, S.; Osborn, R.; Ye, F.; Liu, Y.; Ruff, J. P. C.; Chen, W.; Wozniak, J. M.; Luo, H.; et al. The Relation of Local Order to Material Properties in Relaxor Ferroelectrics. *Nat. Mater.* **2018**, *17*, 718−724.
(174) Paściak, M.; Wołcyrz, M.; Pietraszko, A. Interpretation of the Diffuse Scattering in Pb-Based Relaxor Ferroelectrics in Terms of Three-Dimensional Nanodomains of the < 110>-Directed Relative Interdomain Atomic Shifts. *Phys. Rev. B* **2007**, *76*, No. 014117.

https://doi.org/10.1021/acs.chemrev.3c00532
Chem. Rev. 2024, 124, 2281−2326

(175) Welberry, T.; Weber, T. One Hundred Years of Diffuse Scattering. *Crystallogr. Rev.* **2016**, *22*, 2−78.
(176) Proffen, T.; Kim, H. Advances in Total Scattering Analysis. *J. Mater. Chem.* **2009**, *19*, 5078−5088.
(177) Proffen, T.; Billinge, S. J. L.; Egami, T.; Louca, D. Structural Analysis of Complex Materials Using the Atomic Pair Distribution Function - a Practical Guide. *Z. Kristallogr. Cryst. Mater.* **2003**, *218*, 132−143.
(178) Weadock, N. J.; Sterling, T. C.; Vigil, J. A.; Gold-Parker, A.; Smith, I. C.; Ahammed, B.; Krogstad, M. J.; Ye, F.; Voneshen, D.; Gehring, P. M.; et al. The Nature of Dynamic Local Order in $CH_3NH_3PbI_3$ and $CH_3NH_3PbBr_3$. *Joule* **2023**, *7*, 1051−1066.
(179) Beecher, A. N.; Semonin, O. E.; Skelton, J. M.; Frost, J. M.; Terban, M. W.; Zhai, H.; Alatas, A.; Owen, J. S.; Walsh, A.; Billinge, S. J. L. Direct Observation of Dynamic Symmetry Breaking above Room Temperature in Methylammonium Lead Iodide Perovskite. *ACS Energy Lett.* **2016**, *1*, 880−887.
(180) Bertolotti, F.; Protesescu, L.; Kovalenko, M. V.; Yakunin, S.; Cervellino, A.; Billinge, S. J. L.; Terban, M. W.; Pedersen, J. S.; Masciocchi, N.; Guagliardi, A. Coherent Nanotwins and Dynamic Disorder in Cesium Lead Halide Perovskite Nanocrystals. *ACS Nano* **2017**, *11*, 3819−3831.
(181) Lanigan-Atkins, T.; He, X.; Krogstad, M. J.; Pajerowski, D. M.; Abernathy, D. L.; Xu, G. N. M. N.; Xu, Z.; Chung, D.-Y.; Kanatzidis, M. G.; Rosenkranz, S.; et al. Two-Dimensional Overdamped Fluctuations of the Soft Perovskite Lattice in $CsPbBr_3$. *Nat. Mater.* **2021**, *20*, 977−983.
(182) Onoda-Yamamuro, N.; Matsuo, T.; Suga, H. Calorimetric and IR Spectroscopic Studies of Phase Transitions in Methylammonium Trihalogenoplumbates (II). *J. Phys. Chem. Solids* **1990**, *51*, 1383−1395.
(183) Anusca, I.; Balciunas, S.; Gemeiner, P.; Svirskas, S.; Sanlialp, M.; Lackner, G.; Fettkenhauer, C.; Belovickis, J.; Samulionis, V.; Ivanov, M.; Dkhil, B.; Banys, J.; Shvartsman, V. V.; Lupascu, D. C. Dielectric Response: Answer to Many Questions in the Methylammonium Lead Halide Solar Cell Absorbers. *Adv. Energy Mater.* **2017**, *7*, No. 1700600.
(184) Maczka, M.; Gagor, A.; Zareba, J. K.; Stefanska, D.; Drozd, M.; Balciunas, S.; Simenas, M.; Banys, J.; Sieradzki, A. Three-Dimensional Perovskite Methylhydrazinium Lead Chloride with Two Polar Phases and Unusual Second-Harmonic Generation Bistability above Room Temperature. *Chem. Mater.* **2020**, *32*, 4072−4082.
(185) Maczka, M.; Ptak, M.; Gagor, A.; Stefanska, D.; Zareba, J. K.; Sieradzki, A. Methylhydrazinium Lead Bromide: Noncentrosymmetric Three-Dimensional Perovskite with Exceptionally Large Framework Distortion and Green Photoluminescence. *Chem. Mater.* **2020**, *32*, 1667−1673.
(186) Kawachi, S.; Atsumi, M.; Saito, N.; Ohashi, N.; Murakami, Y.; Yamaura, J.-i. Structural and Thermal Properties in Formamidinium and Cs-Mixed Lead Halides. *J. Phys. Chem. Lett.* **2019**, *10*, 6967−6972.
(187) Schönhals, A.; Kremer, F. *Broadband Dielectric Spectroscopy*, 1st ed.; Springer-Verlag Berlin Heidelberg, 2003.
(188) Grigas, J.; Brilingas, A.; Kalesinskas, V. Microwave and Millimetre Wave Dielectric Spectroscopy of Ferroelectrics. *Ferroelectrics* **1990**, *107*, 61−66.
(189) Banys, J.; Lapinskas, S.; Rudys, S.; Greicius, S.; Grigalaitis, R. High Frequency Measurements of Ferroelecrics and Related Materials in Coaxial Line. *Ferroelectrics* **2011**, *414*, 64−69.
(190) Onoda-Yamamuro, N.; Matsuo, T.; Suga, H. Dielectric Study of $CH_3NH_3PbX_3$ (X = Cl, Br, I). *J. Phys. Chem. Solids* **1992**, *53*, 935−939.
(191) Svirskas, S.; Balciunas, S.; Simenas, M.; Usevicius, G.; Kinka, M.; Velicka, M.; Kubicki, D.; Castillo, M. E.; Karabanov, A.; Shvartsman, V. V.; de Rosario Soares, M.; Sablinskas, V.; Salak, A. N.; Lupascu, D. C.; Banys, J. Phase Transitions, Screening and Dielectric Response of $CsPbBr_3$. *J. Mater. Chem. A* **2020**, *8*, 14015−14022.
(192) Wilson, J. N.; Frost, J. M.; Wallace, S. K.; Walsh, A. Dielectric and Ferroic Properties of Metal Halide Perovskites. *APL Mater.* **2019**, *7*, No. 010901.
(193) Ibaceta-Jaña, J.; Muydinov, R.; Rosado, P.; Mirhosseini, H.; Chugh, M.; Nazarenko, O.; Dirin, D. N.; Heinrich, D.; Wagner, M. R.; Kühne, T. D.; et al. Vibrational Dynamics in Lead Halide Hybrid Perovskites Investigated by Raman Spectroscopy. *Phys. Chem. Chem. Phys.* **2020**, *22*, 5604−5614.
(194) Kontos, A. G.; Manolis, G. K.; Kaltzoglou, A.; Palles, D.; Kamitsos, E. I.; Kanatzidis, M. G.; Falaras, P. Halogen-NH2+ Interaction, Temperature-Induced Phase Transition, and Ordering in $(NH_2CHNH_2)PbX_3$ (X = Cl, Br, I) Hybrid Perovskites. *J. Phys. Chem. C* **2020**, *124*, 8479−8487.
(195) Maczka, M.; Zienkiewicz, J. A.; Ptak, M. Comparative Studies of Phonon Properties of Three-Dimensional Hybrid Organic-Inorganic Perovskites Comprising Methylhydrazinium, Methylammonium, and Formamidinium Cations. *J. Phys. Chem. C* **2022**, *126*, 4048−4056.
(196) Maczka, M.; Ptak, M. Lattice Dynamics and Structural Phase Transitions in Two-Dimensional Ferroelectric Methylhydrazinium Lead Bromide Investigated Using Raman and IR Spectroscopy. *J. Phys. Chem. C* **2022**, *126*, 7991−7998.
(197) Spirito, D.; Asensio, Y.; Hueso, L. E.; Martín-García, B. Raman Spectroscopy in Layered Hybrid Organic-Inorganic Metal Halide Perovskites. *JPhys. Mater.* **2022**, *5*, No. 034004.
(198) Leguy, A. M. A.; Goñi, A. R.; Frost, J. M.; Skelton, J.; Brivio, F.; Rodríguez-Martínez, X.; Weber, O. J.; Pallipurath, A.; Alonso, M. I.; Campoy-Quiles, M.; et al. Dynamic Disorder, Phonon Lifetimes, and the Assignment of Modes to the Vibrational Spectra of Methylammonium Lead Halide Perovskites. *Phys. Chem. Chem. Phys.* **2016**, *18*, 27051−27066.
(199) Schuck, G.; Többens, D. M.; Koch-Müller, M.; Efthimiopoulos, I.; Schorr, S. Infrared Spectroscopic Study of Vibrational Modes across the Orthorhombic-Tetragonal Phase Transition in Methylammonium Lead Halide Single Crystals. *J. Phys. Chem. C* **2018**, *122*, 5227−5237.
(200) Ruan, S.; McMeekin, D. P.; Fan, R.; Webster, N. A. S.; Ebendorff-Heidepriem, H.; Cheng, Y.-B.; Lu, J.; Ruan, Y.; McNeill, C. R. Raman Spectroscopy of Formamidinium-Based Lead Halide Perovskite Single Crystals. *J. Phys. Chem. C* **2020**, *124*, 2265−2272.
(201) Sendner, M.; Nayak, P. K.; Egger, D. A.; Beck, S.; Müller, C.; Epding, B.; Kowalsky, W.; Kronik, L.; Snaith, H. J.; Pucci, A.; et al. Optical Phonons in Methylammonium Lead Halide Perovskites and Implications for Charge Transport. *Mater. Horiz.* **2016**, *3*, 613−620.
(202) Nakada, K.; Matsumoto, Y.; Shimoi, Y.; Yamada, K.; Furukawa, Y. Temperature-Dependent Evolution of Raman Spectra of Methylammonium Lead Halide Perovskites, $CH_3NH_3PbX_3$ (X = I, Br). *Molecules* **2019**, *24*, 626.
(203) Piveteau, L.; Morad, V.; Kovalenko, M. V. Solid-State NMR and NQR Spectroscopy of Lead-Halide Perovskite Materials. *J. Am. Chem. Soc.* **2020**, *142*, 19413−19437.
(204) Mishra, A.; Hope, M. A.; Grätzel, M.; Emsley, L. A Complete Picture of Cation Dynamics in Hybrid Perovskite Materials from Solid-State NMR Spectroscopy. *J. Am. Chem. Soc.* **2023**, *145*, 978−990.
(205) Fykouras, K.; Lahnsteiner, J.; Leupold, N.; Tinnemans, P.; Moos, R.; Panzer, F.; de Wijs, G. A.; Bokdam, M.; Grüninger, H.; Kentgens, A. P. M. Disorder to Order: How Halide Mixing in $MAPbI_{3-x}Br_x$ Perovskites Restricts MA Dynamics. *J. Mater. Chem. A* **2023**, *11*, 4587−4597.
(206) Grüninger, H.; Bokdam, M.; Leupold, N.; Tinnemans, P.; Moos, R.; De Wijs, G. A.; Panzer, F.; Kentgens, A. P. M. Microscopic (Dis)order and Dynamics of Cations in Mixed FA/MA Lead Halide Perovskites. *J. Phys. Chem. C* **2021**, *125*, 1742−1753.
(207) Kubicki, D. J.; Prochowicz, D.; Hofstetter, A.; Zakeeruddin, S. M.; Grätzel, M.; Emsley, L. Phase Segregation in Cs-, Rb- and K-Doped Mixed-Cation $(MA)_x(FA)_{1-x}PbI_3$ Hybrid Perovskites from Solid-State NMR. *J. Am. Chem. Soc.* **2017**, *139*, 14173−14180.

https://doi.org/10.1021/acs.chemrev.3c00532
Chem. Rev. 2024, 124, 2281−2326

(208) Franssen, W. M. J.; van Heumen, C. M. M.; Kentgens, A. P. M. Structural Investigations of $MA_{1-x}DMA_xPbI_3$ Mixed-Cation Perovskites. *Inorg. Chem.* **2020**, *59*, 3730−3739.
(209) Fabini, D. H.; Siaw, T. A.; Stoumpos, C. C.; Laurita, G.; Olds, D.; Page, K.; Hu, J. G.; Kanatzidis, M. G.; Han, S.; Seshadri, R. Universal Dynamics of Molecular Reorientation in Hybrid Lead Iodide Perovskites. *J. Am. Chem. Soc.* **2017**, *139*, 16875−16884.
(210) Dahlman, C. J.; Kubicki, D. J.; Reddy, G. N. M. Interfaces in Metal Halide Perovskites Probed by Solid-State NMR Spectroscopy. *J. Mater. Chem. A* **2021**, *9*, 19206−19244.
(211) Kruteva, M. Dynamics Studied by Quasielastic Neutron Scattering (QENS). *Adsorption* **2021**, *27*, 875−889.
(212) Telling, M. T. *A Practical Guide to Quasi-Elastic Neutron Scattering*; Royal Society of Chemistry, 2020.
(213) Leguy, A. M. A.; Frost, J. M.; McMahon, A. P.; Sakai, V. G.; Kockelmann, W.; Law, C.; Li, X.; Foglia, F.; Walsh, A.; O'Regan, B. C.; et al. The Dynamics of Methylammonium Ions in Hybrid Organic-Inorganic Perovskite Solar Cells. *Nat. Commun.* **2015**, *6*, 7124.
(214) Chen, T.; Foley, B. J.; Ipek, B.; Tyagi, M.; Copley, J. R. D.; Brown, C. M.; Choi, J. J.; Lee, S.-H. Rotational Dynamics of Organic Cations in the $CH_3NH_3PbI_3$ Perovskite. *Phys. Chem. Chem. Phys.* **2015**, *17*, 31278−31286.
(215) Li, J.; Bouchard, M.; Reiss, P.; Aldakov, D.; Pouget, S.; Demadrille, R.; Aumaitre, C.; Frick, B.; Djurado, D.; Rossi, M.; et al. Activation Energy of Organic Cation Rotation in $CH_3NH_3PbI_3$ and $CD_3NH_3PbI_3$: Quasi-Elastic Neutron Scattering Measurements and First-Principles Analysis Including Nuclear Quantum Effects. *J. Phys. Chem. Lett.* **2018**, *9*, 3969−3977.
(216) Li, B.; Kawakita, Y.; Liu, Y.; Wang, M.; Matsuura, M.; Shibata, K.; Ohira-Kawamura, S.; Yamada, T.; Lin, S.; Nakajima, K.; Liu, S. Polar Rotor Scattering as Atomic-Level Origin of Low Mobility and Thermal Conductivity of Perovskite $CH_3NH_3PbI_3$. *Nat. Commun.* **2017**, *8*, No. 16086.
(217) Sharma, V. K.; Mukhopadhyay, R.; Mohanty, A.; Sakai, V. G.; Tyagi, M.; Sarma, D. D. Contrasting Effects of FA Substitution on MA/FA Rotational Dynamics in $FA_xMA_{1-x}PbI_3$. *J. Phys. Chem. C* **2021**, *125*, 13666−13676.
(218) Zhou, X.; Jankowska, J.; Dong, H.; Prezhdo, O. V. Recent Theoretical Progress in The Development of Perovskite Photovoltaic Materials. *J. Energy Chem.* **2018**, *27*, 637−649.
(219) Motta, C.; El-Mellouhi, F.; Sanvito, S. Exploring the Cation Dynamics in Lead-Bromide Hybrid Perovskites. *Phys. Rev. B* **2016**, *93*, No. 235412.
(220) Sukmas, W.; Pinsook, U.; Tsuppayakorn-aek, P.; Pakornchote, T.; Sukserm, A.; Bovornratanaraks, T. Organic Molecule Orientations and Rashba-Dresselhaus Effect in α-Formamidinium Lead Iodide. *J. Phys. Chem. C* **2019**, *123*, 16508−16515.
(221) Weller, M. T.; Weber, O. J.; Frost, J. M.; Walsh, A. Cubic Perovskite Structure of Black Formamidinium Lead Iodide, α-$[HC(NH_2)_2]PbI_3$, at 298 K. *J. Phys. Chem. Lett.* **2015**, *6*, 3209−3212.
(222) Weber, O. J.; Ghosh, D.; Gaines, S.; Henry, P. F.; Walker, A. B.; Islam, M. S.; Weller, M. T. Phase Behavior and Polymorphism of Formamidinium Lead Iodide. *Chem. Mater.* **2018**, *30*, 3768−3778.
(223) Carignano, M. A.; Saeed, Y.; Aravindh, S. A.; Roqan, I. S.; Even, J.; Katan, C. A Close Examination of the Structure and Dynamics of $HC(NH_2)_2PbI_3$ by MD Simulations and Group Theory. *Phys. Chem. Chem. Phys.* **2016**, *18*, 27109−27118.
(224) Bakulin, A. A.; Selig, O.; Bakker, H. J.; Rezus, Y. L.; Müller, C.; Glaser, T.; Lovrincic, R.; Sun, Z.; Chen, Z.; Walsh, A.; et al. Real-Time Observation of Organic Cation Reorientation in Methylammonium Lead Iodide Perovskites. *J. Phys. Chem. Lett.* **2015**, *6*, 3663−3669.
(225) Drużbicki, K.; Lavén, R.; Armstrong, J.; Malavasi, L.; Fernandez-Alonso, F.; Karlsson, M. Cation Dynamics and Structural Stabilization in Formamidinium Lead Iodide Perovskites. *J. Phys. Chem. Lett.* **2021**, *12*, 3503−3508.
(226) Ghosh, D.; Walsh Atkins, P.; Islam, M. S.; Walker, A. B.; Eames, C. Good Vibrations: Locking of Octahedral Tilting in Mixed-Cation Iodide Perovskites for Solar Cells. *ACS Energy Lett.* **2017**, *2*, 2424−2429.
(227) Simenas, M.; Balciunas, S.; Maczka, M.; Banys, J.; Tornau, E. E. Exploring the Antipolar Nature of Methylammonium Lead Halides: A Monte Carlo and Pyrocurrent Study. *J. Phys. Chem. Lett.* **2017**, *8*, 4906−4911.
(228) Simenas, M.; Balciunas, S.; Maczka, M.; Banys, J. Phase Transition Model of FA Cation Ordering in $FAPbX_3$ (X = Br, I) Hybrid Perovskites. *J. Mater. Chem. C* **2022**, *10*, 5210−5217.
(229) Tan, L. Z.; Zheng, F.; Rappe, A. M. Intermolecular Interactions in Hybrid Perovskites Understood from a Combined Density Functional Theory and Effective Hamiltonian Approach. *ACS Energy Lett.* **2017**, *2*, 937−942.
(230) Lahnsteiner, J.; Jinnouchi, R.; Bokdam, M. Long-Range Order Imposed by Short-Range Interactions in Methylammonium Lead Iodide: Comparing Point-Dipole Models to Machine-Learning Force Fields. *Phys. Rev. B* **2019**, *100*, No. 094106.
(231) Park, H.; Ali, A.; Mall, R.; Bensmail, H.; Sanvito, S.; El-Mellouhi, F. Data-Driven Enhancement of Cubic Phase Stability in Mixed-Cation Perovskites. *Mach. Learn.: Sci. Technol.* **2021**, *2*, No. 025030.
(232) Yang, J.; Wang, Y.; Wu, T.; Li, S. Correlating the Composition-Dependent Structural and Electronic Dynamics of Inorganic Mixed Halide Perovskites. *Chem. Mater.* **2020**, *32*, 2470−2481.
(233) Anand, D. V.; Xu, Q.; Wee, J.; Xia, K.; Sum, T. C. Topological Feature Engineering for Machine Learning Based Halide Perovskite Materials Design. *npj Comput. Mater.* **2022**, *8*, 203.
(234) Ahmadi, M.; Ziatdinov, M.; Zhou, Y.; Lass, E. A.; Kalinin, S. V. Machine Learning for High-Throughput Experimental Exploration of Metal Halide Perovskites. *Joule* **2021**, *5*, 2797−2822.
(235) Tao, Q.; Xu, P.; Li, M.; Lu, W. Machine Learning for Perovskite Materials Design and Discovery. *npj Comput. Mater.* **2021**, *7*, 23.
(236) Wiktor, J.; Fransson, E.; Kubicki, D.; Erhart, P. Quantifying Dynamic Tilting in Halide Perovskites: Chemical Trends and Local Correlations. *Chem. Mater.* **2023**, *35*, 6737−6744.
(237) Maczka, M.; Ptak, M.; Gagor, A.; Zareba, J. K.; Liang, X.; Balciunas, S.; Semenikhin, O. A.; Kucheriv, O. I.; Gural'skiy, I.'y. A.; Shova, S.; Walsh, A.; Banys, J.; Simenas, M. Phase Transitions, Dielectric Response, and Nonlinear Optical Properties of Aziridinium Lead Halide Perovskites. *Chem. Mater.* **2023**.359725
(238) Jauch, W.; Palmer, A. Anomalous Zero-Point Motion in $SrTiO_3$: Results from γ-Ray Diffraction. *Phys. Rev. B* **1999**, *60*, 2961−2963.
(239) Glazer, A. M. Simple Ways of Determining Perovskite Structures. *Acta Crystallogr., Sect. A* **1975**, *31*, 756−762.
(240) Poglitsch, A.; Weber, D. Dynamic Disorder in Methylammoniumtrihalogenoplumbates (II) Observed by Millimeter-Wave Spectroscopy. *J. Chem. Phys.* **1987**, *87*, 6373−6378.
(241) Whitfield, P. S.; Herron, N.; Guise, W. E.; Page, K.; Cheng, Y. Q.; Milas, I.; Crawford, M. K. Structures, Phase Transitions and Tricritical Behavior of the Hybrid Perovskite Methyl Ammonium Lead Iodide. *Sci. Rep.* **2016**, *6*, No. 35685.
(242) Yamada, Y.; Yamada, T.; Phuong, L. Q.; Maruyama, N.; Nishimura, H.; Wakamiya, A.; Murata, Y.; Kanemitsu, Y. Dynamic Optical Properties of $CH_3NH_3PbI_3$ Single Crystals As Revealed by One- and Two-Photon Excited Photoluminescence Measurements. *J. Am. Chem. Soc.* **2015**, *137*, 10456−10459.
(243) Szafrański, M.; Katrusiak, A. Mechanism of Pressure-Induced Phase Transitions, Amorphization, and Absorption-Edge Shift in Photovoltaic Methylammonium Lead Iodide. *J. Phys. Chem. Lett.* **2016**, *7*, 3458−3466.
(244) Frost, J. M.; Butler, K. T.; Walsh, A. Molecular Ferroelectric Contributions to Anomalous Hysteresis in Hybrid Perovskite Solar Cells. *APL Mater.* **2014**, *2*, No. 081506.
(245) Kutes, Y.; Ye, L.; Zhou, Y.; Pang, S.; Huey, B. D.; Padture, N. P. Direct Observation of Ferroelectric Domains in Solution-Processed

https://doi.org/10.1021/acs.chemrev.3c00532
Chem. Rev. 2024, 124, 2281−2326

$CH_3NH_3PbI_3$ Perovskite Thin Films. *J. Phys. Chem. Lett.* **2014**, *5*, 3335−3339.
(246) Chen, H.-W.; Sakai, N.; Ikegami, M.; Miyasaka, T. Emergence of Hysteresis and Transient Ferroelectric Response in Organo-Lead Halide Perovskite Solar Cells. *J. Phys. Chem. Lett.* **2015**, *6*, 164−169.
(247) Kim, H.-S.; Kim, S. K.; Kim, B. J.; Shin, K.-S.; Gupta, M. K.; Jung, H. S.; Kim, S.-W.; Park, N.-G. Ferroelectric Polarization in $CH_3NH_3PbI_3$ Perovskite. *J. Phys. Chem. Lett.* **2015**, *6*, 1729−1735.
(248) Rakita, Y.; Bar-Elli, O.; Meirzadeh, E.; Kaslasi, H.; Peleg, Y.; Hodes, G.; Lubomirsky, I.; Oron, D.; Ehre, D.; Cahen, D. Tetragonal $CH_3NH_3PbI_3$ is Ferroelectric. *Proc. Natl. Acad. Sci. U. S. A.* **2017**, *114*, E5504−E5512.
(249) Rakita, Y.; Meirzadeh, E.; Bendikov, T.; Kalchenko, V.; Lubomirsky, I.; Hodes, G.; Ehre, D.; Cahen, D. $CH_3NH_3PbBr_3$ is Not Pyroelectric, Excluding Ferroelectric-Enhanced Photovoltaic Performance. *APL Mater.* **2016**, *4*, No. 051101.
(250) Hoque, M. N. F.; Yang, M.; Li, Z.; Islam, N.; Pan, X.; Zhu, K.; Fan, Z. Polarization and Dielectric Study of Methylammonium Lead Iodide Thin Film to Reveal its Nonferroelectric Nature under Solar Cell Operating Conditions. *ACS Energy Lett.* **2016**, *1*, 142−149.
(251) Gómez, A.; Wang, Q.; Goñi, A. R.; Campoy-Quiles, M.; Abate, A. Ferroelectricity-Free Lead Halide Perovskites. *Energy Environ. Sci.* **2019**, *12*, 2537−2547.
(252) Ambrosio, F.; De Angelis, F.; Goñi, A. R. The Ferroelectric-Ferroelastic Debate about Metal Halide Perovskites. *J. Phys. Chem. Lett.* **2022**, *13*, 7731−7740.
(253) Mayers, M. Z.; Tan, L. Z.; Egger, D. A.; Rappe, A. M.; Reichman, D. R. How Lattice and Charge Fluctuations Control Carrier Dynamics in Halide Perovskites. *Nano Lett.* **2018**, *18*, 8041−8046.
(254) Zhu, T.; Ertekin, E. Mixed Phononic and Non-Phononic Transport in Hybrid Lead Halide Perovskites: Glass-Crystal Duality, Dynamical Disorder, and Anharmonicity. *Energy Environ. Sci.* **2019**, *12*, 216−229.
(255) Comin, R.; Crawford, M. K.; Said, A. H.; Herron, N.; Guise, W. E.; Wang, X.; Whitfield, P. S.; Jain, A.; Gong, X.; McGaughey, A. J. H.; et al. Lattice Dynamics and the Nature of Structural Transitions in Organolead Halide Perovskites. *Phys. Rev. B* **2016**, *94*, No. 094301.
(256) Whalley, L. D.; Frost, J. M.; Jung, Y.-K.; Walsh, A. Perspective: Theory and simulation of hybrid halide perovskites. *J. Chem. Phys.* **2017**, *146*, No. 220901.
(257) Yaffe, O.; Guo, Y.; Tan, L. Z.; Egger, D. A.; Hull, T.; Stoumpos, C. C.; Zheng, F.; Heinz, T. F.; Kronik, L.; Kanatzidis, M. G.; et al. Local Polar Fluctuations in Lead Halide Perovskite Crystals. *Phys. Rev. Lett.* **2017**, *118*, No. 136001.
(258) Songvilay, M.; Giles-Donovan, N.; Bari, M.; Ye, Z.-G.; Minns, J. L.; Green, M. A.; Xu, G.; Gehring, P. M.; Schmalzl, K.; Ratcliff, W. D.; et al. Common Acoustic Phonon Lifetimes in Inorganic and Hybrid Lead Halide Perovskites. *Phys. Rev. Mater.* **2019**, *3*, No. 093602.
(259) Weadock, N. J.; Gehring, P. M.; Gold-Parker, A.; Smith, I. C.; Karunadasa, H. I.; Toney, M. F. Test of the Dynamic-Domain and Critical Scattering Hypotheses in Cubic Methylammonium Lead Triiodide. *Phys. Rev. Lett.* **2020**, *125*, No. 075701.
(260) Guo, Y.; Yaffe, O.; Paley, D. W.; Beecher, A. N.; Hull, T. D.; Szpak, G.; Owen, J. S.; Brus, L. E.; Pimenta, M. A. Interplay Between Organic Cations and Inorganic Framework and Incommensurability in Hybrid Lead-Halide Perovskite $CH_3NH_3PbBr_3$. *Phys. Rev. Mater.* **2017**, *1*, No. 042401.
(261) Kawamura, Y.; Mashiyama, H. Modulated Structure in Phase II of $CH_3NH_3PbCl_3$. *J. Korean Phys. Soc.* **1999**, *35*, S1437−S1440.
(262) Chi, L.; Swainson, I.; Cranswick, L.; Her, J.-H.; Stephens, P.; Knop, O. The Ordered Phase of Methylammonium Lead Chloride $CH_3ND_3PbCl_3$. *J. Solid State Chem.* **2005**, *178*, 1376−1385.
(263) Cordero, F.; Craciun, F.; Trequattrini, F.; Generosi, A.; Paci, B.; Paoletti, A. M.; Pennesi, G. Stability of Cubic $FAPbI_3$ from X-ray Diffraction, Anelastic, and Dielectric Measurements. *J. Phys. Chem. Lett.* **2019**, *10*, 2463−2469.
(264) Chen, T.; Foley, B. J.; Park, C.; Brown, C. M.; Harriger, L. W.; Lee, J.; Ruff, J.; Yoon, M.; Choi, J. J.; Lee, S.-H. Entropy-Driven Structural Transition and Kinetic Trapping in Formamidinium Lead Iodide Perovskite. *Sci. Adv.* **2016**, *2*, No. e1601650.
(265) Chen, T.; Chen, W.-L.; Foley, B. J.; Lee, J.; Ruff, J. P. C.; Ko, J. Y. P.; Brown, C. M.; Harriger, L. W.; Zhang, D.; Park, C.; et al. Origin of Long Lifetime of Band-Edge Charge Carriers in Organic-Inorganic Lead Iodide Perovskites. *Proc. Natl. Acad. Sci. U. S. A.* **2017**, *114*, 7519−7524.
(266) Kennedy, B. J.; Prodjosantoso, A. K.; Howard, C. J. Powder Neutron Diffraction Study of the High Temperature Phase Transitions in $NaTaO_3$. *J. Phys.: Condens. Matter* **1999**, *11*, 6319.
(267) Sun, S.; Deng, Z.; Wu, Y.; Wei, F.; Halis Isikgor, F.; Brivio, F.; Gaultois, M. W.; Ouyang, J.; Bristowe, P. D.; Cheetham, A. K.; et al. Variable Temperature and High-Pressure Crystal Chemistry of Perovskite Formamidinium Lead Iodide: a Single Crystal X-Ray Diffraction and Computational Study. *Chem. Commun.* **2017**, *53*, 7537−7540.
(268) Fabini, D. H.; Stoumpos, C. C.; Laurita, G.; Kaltzoglou, A.; Kontos, A. G.; Falaras, P.; Kanatzidis, M. G.; Seshadri, R. Reentrant Structural and Optical Properties and Large Positive Thermal Expansion in Perovskite Formamidinium Lead Iodide. *Angew. Chem., Int. Ed.* **2016**, *55*, 15392−15396.
(269) Franz, A.; Többens, D. M.; Lehmann, F.; Kärgell, M.; Schorr, S. The Influence of Deuteration on the Crystal Structure of Hybrid Halide Perovskites: a Temperature-Dependent Neutron Diffraction Study of $FAPbBr_3$. *Acta Crystallogr., Sect. B* **2020**, *76*, 267−274.
(270) Mozur, E. M.; Trowbridge, J. C.; Maughan, A. E.; Gorman, M. J.; Brown, C. M.; Prisk, T. R.; Neilson, J. R. Dynamical Phase Transitions and Cation Orientation-Dependent Photoconductivity in $CH(NH_2)_2PbBr_3$. *ACS Mater. Lett.* **2019**, *1*, 260−264.
(271) Maczka, M.; Ptak, M. Temperature-Dependent Raman Studies of $FAPbBr_3$ and $MAPbBr_3$ Perovskites: Effect of Phase Transitions on Molecular Dynamics and Lattice Distortion. *Solids* **2022**, *3*, 111−121.
(272) Dimitrovska-Lazova, S.; Bukleski, M.; Tzvetkov, P.; Pecovska-Gjorgjevich, M.; Kovacheva, D.; Aleksovska, S. The Mechanism of the Isostructural Phase Transition in $C(NH_2)_3PbI_3$ as a Guide for Understanding the Properties of the New Phase. *Mater. Chem. Phys.* **2022**, *275*, No. 125240.
(273) Yesudhas, S.; Burns, R.; Lavina, B.; Tkachev, S. N.; Sun, J.; Ullrich, C. A.; Guha, S. Coupling of Organic Cation and Inorganic Lattice in Methylammonium Lead Halide Perovskites: Insights into a Pressure-Induced Isostructural Phase Transition. *Phys. Rev. Mater.* **2020**, *4*, No. 105403.
(274) Govinda, S.; Kore, B. P.; Swain, D.; Hossain, A.; De, C.; Guru Row, T. N.; Sarma, D. D. Critical Comparison of $FAPbX_3$ and $MAPbX_3$ (X = Br and Cl): How Do They Differ? *J. Phys. Chem. C* **2018**, *122*, 13758−13766.
(275) Sharma, V. K.; Mukhopadhyay, R.; Mohanty, A.; García Sakai, V.; Tyagi, M.; Sarma, D. D. Influence of the Halide Ion on the A-Site Dynamics in $FAPbX_3$ (X = Br and Cl). *J. Phys. Chem. C* **2022**, *126*, 7158−7168.
(276) Møller, C. K. Crystal Structure and Photoconductivity of Caesium Plumbohalides. *Nature* **1958**, *182*, 1436−1436.
(277) Stoumpos, C. C.; Kanatzidis, M. G. The Renaissance of Halide Perovskites and Their Evolution as Emerging Semiconductors. *Acc. Chem. Res.* **2015**, *48*, 2791−2802.
(278) Marronnier, A.; Roma, G.; Boyer-Richard, S.; Pedesseau, L.; Jancu, J.-M.; Bonnassieux, Y.; Katan, C.; Stoumpos, C. C.; Kanatzidis, M. G.; Even, J. Anharmonicity and Disorder in the Black Phases of Cesium Lead Iodide Used for Stable Inorganic Perovskite Solar Cells. *ACS Nano* **2018**, *12*, 3477−3486.
(279) Trots, D.; Myagkota, S. High-Temperature Structural Evolution of Caesium and Rubidium Triiodoplumbates. *J. Phys. Chem. Solids* **2008**, *69*, 2520−2526.
(280) Zhao, B.; Jin, S.-F.; Huang, S.; Liu, N.; Ma, J.-Y.; Xue, D.-J.; Han, Q.; Ding, J.; Ge, Q.-Q.; Feng, Y.; et al. Thermodynamically Stable Orthorhombic γ-$CsPbI_3$ Thin Films for High-Performance Photovoltaics. *J. Am. Chem. Soc.* **2018**, *140*, 11716−11725.

https://doi.org/10.1021/acs.chemrev.3c00532
Chem. Rev. 2024, 124, 2281−2326

(281) Sutton, R. J.; Filip, M. R.; Haghighirad, A. A.; Sakai, N.; Wenger, B.; Giustino, F.; Snaith, H. J. Cubic or Orthorhombic? Revealing the Crystal Structure of Metastable Black-Phase $CsPbI_3$ by Theory and Experiment. *ACS Energy Lett.* **2018**, *3*, 1787−1794.
(282) Cohen, A. V.; Egger, D. A.; Rappe, A. M.; Kronik, L. Breakdown of the Static Picture of Defect Energetics in Halide Perovskites: The Case of the Br Vacancy in $CsPbBr_3$. *J. Phys. Chem. Lett.* **2019**, *10*, 4490−4498.
(283) Li, Z.-G.; Zacharias, M.; Zhang, Y.; Wei, F.; Qin, Y.; Yang, Y.-Q.; An, L.-C.; Gao, F.-F.; Li, W.; Even, J.; et al. Origin of Phase Transitions in Inorganic Lead Halide Perovskites: Interplay between Harmonic and Anharmonic Vibrations. *ACS Energy Lett.* **2023**, *8*, 3016−3024.
(284) Stoumpos, C. C.; Malliakas, C. D.; Peters, J. A.; Liu, Z.; Sebastian, M.; Im, J.; Chasapis, T. C.; Wibowo, A. C.; Chung, D. Y.; Freeman, A. J.; et al. Crystal Growth of the Perovskite Semiconductor $CsPbBr_3$: A New Material for High-Energy Radiation Detection. *Cryst. Growth Des.* **2013**, *13*, 2722−2727.
(285) Cottingham, P.; Brutchey, R. L. Depressed Phase Transitions and Thermally Persistent Local Distortions in $CsPbBr_3$ Quantum Dots. *Chem. Mater.* **2018**, *30*, 6711−6716.
(286) Sakata, M.; Nishiwaki, T.; Harada, J. Neutron Diffraction Study of the Structure of Cubic $CsPbBr_3$. *J. Phys. Soc. Jpn.* **1979**, *47*, 232−233.
(287) Rodová, M.; Brožek, J.; Knížek, K.; Nitsch, K. Phase Transitions in Ternary Caesium Lead Bromide. *J. Therm. Anal. Calorim.* **2003**, *71*, 667−673.
(288) Linaburg, M. R.; McClure, E. T.; Majher, J. D.; Woodward, P. M. $Cs_{1-x}Rb_xPbCl_3$ and $Cs_{1-x}Rb_xPbBr_3$ Solid Solutions: Understanding Octahedral Tilting in Lead Halide Perovskites. *Chem. Mater.* **2017**, *29*, 3507−3514.
(289) Harada, J.; Sakata, M.; Hoshino, S.; Hirotsu, S. Neutron Diffraction Study of the Structure in Cubic $CsPbCl_3$. *J. Phys. Soc. Jpn.* **1976**, *40*, 212−218.
(290) Gesi, K.; Ozawa, K.; Hirotsu, S. Effect of Hydrostatic Pressure on the Structural Phase Transitions in $CsPbCl_3$ and $CsPbBr_3$. *J. Phys. Soc. Jpn.* **1975**, *38*, 463−466.
(291) Hua, G. L. Normal Vibration Modes and the Structural Phase Transitions in Caesium Trichloroplumbate $CsPbCl_3$. *J. Phys.: Condens. Matter* **1991**, *3*, 1371.
(292) Hirotsu, S.; Sawada, S. Crystal Growth and Phase Transitions of $CsPbCl_3$. *Phys. Lett. A* **1969**, *28*, 762−763.
(293) Hirotsu, S. Experimental Studies of Structural Phase Transitions in $CsPbCl_3$. *J. Phys. Soc. Jpn.* **1971**, *31*, 552−560.
(294) Zhang, L.; Wang, L.; Wang, K.; Zou, B. Pressure-Induced Structural Evolution and Optical Properties of Metal-Halide Perovskite $CsPbCl_3$. *J. Phys. Chem. C* **2018**, *122*, 15220−15225.
(295) Szafrański, M.; Katrusiak, A.; Ståhl, K. Time-Dependent Transformation Routes of Perovskites $CsPbBr_3$ and $CsPbCl_3$ Under High Pressure. *J. Mater. Chem. A* **2021**, *9*, 10769−10779.
(296) Sharma, S.; Weiden, N.; Weiss, A. Phase Transitions in $CsSnCl_3$ and $CsPbBr_3$. An NMR and NQR Study. *Z. Naturforsch. A* **1991**, *46*, 329−336.
(297) Kubicki, D. J.; Prochowicz, D.; Salager, E.; Rakhmatullin, A.; Grey, C. P.; Emsley, L.; Stranks, S. D. Local Structure and Dynamics in Methylammonium, Formamidinium, and Cesium Tin(II) Mixed-Halide Perovskites from ^{119}Sn Solid-State NMR. *J. Am. Chem. Soc.* **2020**, *142*, 7813−7826.
(298) Petrosova, H. R.; Kucheriv, O. I.; Shova, S.; Gural'skiy, I. A. Aziridinium Cation Templating 3D Lead Halide Hybrid Perovskites. *Chem. Commun.* **2022**, *58*, 5745−5748.
(299) Cortecchia, D.; Neutzner, S.; Yin, J.; Salim, T.; Srimath Kandada, A. R.; Bruno, A.; Lam, Y. M.; Martí-Rujas, J.; Petrozza, A.; Soci, C. Structure-Controlled Optical Thermoresponse in Ruddlesden-Popper Layered Perovskites. *APL Mater.* **2018**, *6*, No. 114207.
(300) Li, L.; Liu, X.; Li, Y.; Xu, Z.; Wu, Z.; Han, S.; Tao, K.; Hong, M.; Luo, J.; Sun, Z. Two-Dimensional Hybrid Perovskite-Type Ferroelectric for Highly Polarization-Sensitive Shortwave Photodetection. *J. Am. Chem. Soc.* **2019**, *141*, 2623−2629.
(301) Li, L.; Shang, X.; Wang, S.; Dong, N.; Ji, C.; Chen, X.; Zhao, S.; Wang, J.; Sun, Z.; Hong, M.; et al. Bilayered Hybrid Perovskite Ferroelectric with Giant Two-Photon Absorption. *J. Am. Chem. Soc.* **2018**, *140*, 6806−6809.
(302) Koegel, A. A.; Oswald, I. W. H.; Rivera, C.; Miller, S. L.; Fallon, M. J.; Prisk, T. R.; Brown, C. M.; Neilson, J. R. Influence of Inorganic Layer Thickness on Methylammonium Dynamics in Hybrid Perovskite Derivatives. *Chem. Mater.* **2022**, *34*, 8316−8323.
(303) Li, L.; Sun, Z.; Wang, P.; Hu, W.; Wang, S.; Ji, C.; Hong, M.; Luo, J. Tailored Engineering of an Unusual $(C_4H_9NH_3)_2(CH_3NH_3)_2Pb_3Br_{10}$ Two-Dimensional Multilayered Perovskite Ferroelectric for a High-Performance Photodetector. *Angew. Chem., Int. Ed.* **2017**, *56*, 12150−12154.
(304) Wu, Z.; Liu, X.; Ji, C.; Li, L.; Wang, S.; Peng, Y.; Tao, K.; Sun, Z.; Hong, M.; Luo, J. Discovery of an Above-Room-Temperature Antiferroelectric in Two-Dimensional Hybrid Perovskite. *J. Am. Chem. Soc.* **2019**, *141*, 3812−3816.
(305) Ji, C.; Wang, S.; Wang, Y.; Chen, H.; Li, L.; Sun, Z.; Sui, Y.; Wang, S.; Luo, J. 2D Hybrid Perovskite Ferroelectric Enables Highly Sensitive X-Ray Detection with Low Driving Voltage. *Adv. Funct. Mater.* **2020**, *30*, No. 1905529.
(306) Wang, S.; Liu, X.; Li, L.; Ji, C.; Sun, Z.; Wu, Z.; Hong, M.; Luo, J. An Unprecedented Biaxial Trilayered Hybrid Perovskite Ferroelectric with Directionally Tunable Photovoltaic Effects. *J. Am. Chem. Soc.* **2019**, *141*, 7693−7697.
(307) Ma, Y.; Wang, J.; Guo, W.; Han, S.; Xu, J.; Liu, Y.; Lu, L.; Xie, Z.; Luo, J.; Sun, Z. The First Improper Ferroelectric of 2D Multilayered Hybrid Perovskite Enabling Strong Tunable Polarization-Directed Second Harmonic Generation Effect. *Adv. Funct. Mater.* **2021**, *31*, No. 2103012.
(308) Liu, Y.; Han, S.; Wang, J.; Ma, Y.; Guo, W.; Huang, X.-Y.; Luo, J.-H.; Hong, M.; Sun, Z. Spacer Cation Alloying of a Homoconformational Carboxylate trans Isomer to Boost in-Plane Ferroelectricity in a 2D Hybrid Perovskite. *J. Am. Chem. Soc.* **2021**, *143*, 2130−2137.
(309) Han, S.; Li, M.; Liu, Y.; Guo, W.; Hong, M.-C.; Sun, Z.; Luo, J. Tailoring of a Visible-Light-Absorbing Biaxial Ferroelectric Towards Broadband Self-Driven Photodetection. *Nat. Commun.* **2021**, *12*, 284.
(310) Wang, S.; Li, L.; Weng, W.; Ji, C.; Liu, X.; Sun, Z.; Lin, W.; Hong, M.; Luo, J. Trilayered Lead Chloride Perovskite Ferroelectric Affording Self-Powered Visible-Blind Ultraviolet Photodetection with Large Zero-Bias Photocurrent. *J. Am. Chem. Soc.* **2020**, *142*, 55−59.
(311) Liu, X.; Wang, S.; Long, P.; Li, L.; Peng, Y.; Xu, Z.; Han, S.; Sun, Z.; Hong, M.; Luo, J. Polarization-Driven Self-Powered Photodetection in a Single-Phase Biaxial Hybrid Perovskite Ferroelectric. *Angew. Chem., Int. Ed.* **2019**, *58*, 14504−14508.
(312) Peng, Y.; Liu, X.; Sun, Z.; Ji, C.; Li, L.; Wu, Z.; Wang, S.; Yao, Y.; Hong, M.; Luo, J. Exploiting the Bulk Photovoltaic Effect in a 2D Trilayered Hybrid Ferroelectric for Highly Sensitive Polarized Light Detection. *Angew. Chem., Int. Ed.* **2020**, *59*, 3933−3937.
(313) Peng, Y.; Bie, J.; Liu, X.; Li, L.; Chen, S.; Fa, W.; Wang, S.; Sun, Z.; Luo, J. Acquiring High-T_C Layered Metal Halide Ferroelectrics via Cage-Confined Ethylamine Rotators. *Angew. Chem., Int. Ed.* **2021**, *60*, 2839−2843.
(314) Xu, Z.; Dong, X.; Wang, L.; Wu, H.; Liu, Y.; Luo, J.; Hong, M.; Li, L. Precisely Tailoring a $FAPbI_3$-Derived Ferroelectric for Sensitive Self-Driven Broad-Spectrum Polarized Photodetection. *J. Am. Chem. Soc.* **2023**, *145*, 1524−1529.
(315) Liu, Y.; Xu, H.; Liu, X.; Han, S.; Guo, W.; Ma, Y.; Fan, Q.; Hu, X.; Sun, Z.; Luo, J. A Room-Temperature Antiferroelectric in Hybrid Perovskite Enables Highly Efficient Energy Storage at Low Electric Fields. *Chem. Sci.* **2022**, *13*, 13499−13506.
(316) Vasileiadou, E. S.; Hadar, I.; Kepenekian, M.; Even, J.; Tu, Q.; Malliakas, C. D.; Friedrich, D.; Spanopoulos, I.; Hoffman, J. M.; Dravid, V. P.; et al. Shedding Light on the Stability and Structure-Property Relationships of Two-Dimensional Hybrid Lead Bromide Perovskites. *Chem. Mater.* **2021**, *33*, 5085−5107.

https://doi.org/10.1021/acs.chemrev.3c00532
Chem. Rev. 2024, 124, 2281−2326

(317) Li, X.; Fu, Y.; Pedesseau, L.; Guo, P.; Cuthriell, S.; Hadar, I.; Even, J.; Katan, C.; Stoumpos, C. C.; Schaller, R. D.; et al. Negative Pressure Engineering with Large Cage Cations in 2D Halide Perovskites Causes Lattice Softening. *J. Am. Chem. Soc.* **2020**, *142*, 11486−11496.
(318) Lyu, F.; Zheng, X.; Li, Z.; Chen, Z.; Shi, R.; Wang, Z.; Liu, H.; Lin, B.-L. Spatiodynamics, Photodynamics, and Their Correlation in Hybrid Perovskites. *Chem. Mater.* **2021**, *33*, 3524−3533.
(319) Jia, Q.-Q.; Ni, H.-F.; Lun, M.-M.; Xie, L.-Y.; Lu, H.-F.; Fu, D.-W.; Guo, Q. Tunable Phase Transition Temperature and Nonlinear Optical Properties of Organic-Inorganic Hybrid Perovskites Enabled by Dimensional Engineering. *J. Mater. Chem. C* **2022**, *10*, 16330−16336.
(320) Lu, L.; Weng, W.; Ma, Y.; Liu, Y.; Han, S.; Liu, X.; Xu, H.; Lin, W.; Sun, Z.; Luo, J. Anisotropy in a 2D Perovskite Ferroelectric Drives Self-Powered Polarization-Sensitive Photoresponse for Ultraviolet Solar-Blind Polarized-Light Detection. *Angew. Chem., Int. Ed.* **2022**, *61*, No. e202205030.
(321) Xu, Z.; Weng, W.; Li, Y.; Liu, X.; Yang, T.; Li, M.; Huang, X.; Luo, J.; Sun, Z. 3D-to-2D Dimensional Reduction for Exploiting a Multilayered Perovskite Ferroelectric toward Polarized-Light Detection in the Solar-Blind Ultraviolet Region. *Angew. Chem., Int. Ed.* **2020**, *59*, 21693−21697.
(322) Guo, W.; Xu, H.; Ma, Y.; Liu, Y.; Gao, H.; Hu, T.; Ren, W.; Luo, J.; Sun, Z. Electrically Switchable Persistent Spin Texture in a Two-Dimensional Hybrid Perovskite Ferroelectric. *Angew. Chem., Int. Ed.* **2023**, *62*, No. e202300028.
(323) Li, M.; Xu, Y.; Han, S.; Xu, J.; Xie, Z.; Liu, Y.; Xu, Z.; Hong, M.; Luo, J.; Sun, Z. Giant and Broadband Multiphoton Absorption Nonlinearities of a 2D Organometallic Perovskite Ferroelectric. *Adv. Mater.* **2020**, *32*, No. 2002972.
(324) Hua, L.; Wang, J.; Liu, Y.; Guo, W.; Ma, Y.; Xu, H.; Han, S.; Luo, J.; Sun, Z. Improper High-T_c Perovskite Ferroelectric with Dielectric Bistability Enables Broadband Ultraviolet-to-Infrared Photopyroelectric Effects. *Adv. Sci.* **2023**, *10*, No. 2301064.
(325) Wang, J.; Ma, Y.; Wang, Z.; Liu, X.; Han, S.; Liu, Y.; Guo, W.; Luo, J.; Sun, Z. Unusual Ferroelectric-Dependent Birefringence in 2D Trilayered Perovskite-Type Ferroelectric Exploited by Dimensional Tailoring. *Matter* **2022**, *5*, 194−205.
(326) Guo, W.; Xu, H.; Ma, Y.; Liu, Y.; Wang, B.; Tang, L.; Hua, L.; Luo, J.; Sun, Z. The Unprecedented Highest-Layer-Number Ferroelectric Semiconductor of 2D Homologous Single-Phase Perovskites Tailored by Regulating Thickness of Inorganic Frameworks. *Adv. Funct. Mater.* **2022**, *32*, No. 2207854.
(327) Zhuang, J.-c.; Wei, W.-j.; Song, N.; Tang, Y.-z.; Tan, Y.-h.; Han, D.-c.; Li, Y.-k. A Narrow Bandgap of 2D Ruddlesden-Popper Bilayer Perovskite with Giant Entropy Change and Photoluminescence. *Chem.—Eur. J.* **2021**, *27*, 15716−15721.
(328) Li, X.; Wu, F.; Yao, Y.; Wu, W.; Ji, C.; Li, L.; Sun, Z.; Luo, J.; Liu, X. Robust Spin-Dependent Anisotropy of Circularly Polarized Light Detection from Achiral Layered Hybrid Perovskite Ferroelectric Crystals. *J. Am. Chem. Soc.* **2022**, *144*, 14031−14036.
(329) Wang, B.; Guo, W.; Liu, Y.; Xu, H.; Fan, Q.; Hua, L.; Tang, L.; Han, S.; Luo, J.; Sun, Z. Exceptionally Strong Self-Powered Polarization Behaviors Involving with Bulk Photovoltaics in Highly Anisotropic 2D Hybrid Perovskite Ferroelectric Crystals. *Chem. Mater.* **2023**, *35*, 4007−4014.
(330) Han, S.; Li, L.; Ji, C.; Liu, X.; Wang, G.-E.; Xu, G.; Sun, Z.; Luo, J. Visible-Photoactive Perovskite Ferroelectric-Driven Self-Powered Gas Detection. *J. Am. Chem. Soc.* **2023**, *145*, 12853−12860.
(331) Wu, Z.; Ji, C.; Li, L.; Kong, J.; Sun, Z.; Zhao, S.; Wang, S.; Hong, M.; Luo, J. Alloying n-Butylamine into $CsPbBr_3$ To Give a Two-Dimensional Bilayered Perovskite Ferroelectric Material. *Angew. Chem., Int. Ed.* **2018**, *57*, 8140−8143.
(332) Ye, H.; Peng, Y.; Shang, X.; Li, L.; Yao, Y.; Zhang, X.; Zhu, T.; Liu, X.; Chen, X.; Luo, J. Self-Powered Visible-Infrared Polarization Photodetection Driven by Ferroelectric Photovoltaic Effect in a Dion-Jacobson Hybrid Perovskite. *Adv. Funct. Mater.* **2022**, *32*, No. 2200223.
(333) Drozdowski, D.; Fedoruk, K.; Kabanski, A.; Maczka, M.; Sieradzki, A.; Gagor, A. Broadband Yellow and White Emission from Large Octahedral Tilting in (110)-Oriented Layered Perovskites: Imidazolium-Methylhydrazinium Lead Halides. *J. Mater. Chem. C* **2023**, *11*, 4907−4915.
(334) Lee, J.-W.; Seo, S.; Nandi, P.; Jung, H. S.; Park, N.-G.; Shin, H. Dynamic Structural Property of Organic-Inorganic Metal Halide Perovskite. *iScience* **2021**, *24*, No. 101959.
(335) Byranvand, M. M.; Otero-Martínez, C.; Ye, J.; Zuo, W.; Manna, L.; Saliba, M.; Hoye, R. L. Z.; Polavarapu, L. Recent Progress in Mixed A-Site Cation Halide Perovskite Thin-Films and Nanocrystals for Solar Cells and Light-Emitting Diodes. *Adv. Opt. Mater.* **2022**, *10*, No. 2200423.
(336) Mohanty, A.; Swain, D.; Govinda, S.; Row, T. N. G.; Sarma, D. D. Phase Diagram and Dielectric Properties of $MA_{1-x}FA_xPbI_3$. *ACS Energy Lett.* **2019**, *4*, 2045−2051.
(337) Zheng, H.; Dai, J.; Duan, J.; Chen, F.; Zhu, G.; Wang, F.; Xu, C. Temperature-Dependent Photoluminescence Properties of Mixed-Cation Methylammonium-Formamidium Lead Iodide $[HC(NH_2)_2]_x[CH_3NH_3]_{1-x}PbI_3$ Perovskite Nanostructures. *J. Mater. Chem. C* **2017**, *5*, 12057−12061.
(338) Glinka, Y. D.; Cai, R.; Gao, X.; Wu, D.; Chen, R.; Sun, X. W. Structural Phase Transitions and Photoluminescence Mechanism in a Layer of 3D Hybrid Perovskite Nanocrystals. *AIP Adv.* **2020**, *10*, No. 065028.
(339) Ahmadi, M.; Collins, L.; Puretzky, A.; Zhang, J.; Keum, J. K.; Lu, W.; Ivanov, I.; Kalinin, S. V.; Hu, B. Exploring Anomalous Polarization Dynamics in Organometallic Halide Perovskites. *Adv. Mater.* **2018**, *30*, No. 1705298.
(340) Onoda-Yamamuro, N.; Matsuo, T.; Suga, H. Dielectric Study of $CH_3NH_3PbX_3$ (X = Cl, Br, I). *J. Phys. Chem. Solids* **1992**, *53*, 935−939.
(341) Govinda, S.; Kore, B. P.; Bokdam, M.; Mahale, P.; Kumar, A.; Pal, S.; Bhattacharyya, B.; Lahnsteiner, J.; Kresse, G.; Franchini, C.; et al. Behavior of Methylammonium Dipoles in $MAPbX_3$ (X = Br and I). *J. Phys. Chem. Lett.* **2017**, *8*, 4113−4121.
(342) Fabini, D. H.; Seshadri, R.; Kanatzidis, M. G. The Underappreciated Lone Pair in Halide Perovskites Underpins their Unusual Properties. *MRS Bull.* **2020**, *45*, 467−477.
(343) Kalita, D.; Sahu, P.; Nandi, P.; Madapu, K. K.; Dhara, S.; Schoekel, A.; Mahanti, S. D.; Topwal, D.; Manju, U. Elucidating Phase Transitions and the Genesis of Broadband Emission in $MA_{1-x}FA_xPbBr_3$ Perovskites. *J. Phys. Chem. C* **2023**.*12*724608
(344) Gallop, N. P.; Ye, J.; Greetham, G. M.; Jansen, T. L. C.; Dai, L.; Zelewski, S. J.; Arul, R.; Baumberg, J. J.; Hoye, R. L. Z.; Bakulin, A. A. The Effect of Caesium Alloying on the Ultrafast Structural Dynamics of Hybrid Organic-Inorganic Halide Perovskites. *J. Mater. Chem. A* **2022**, *10*, 22408−22418.
(345) García-Fernández, A.; Bermúdez-García, J. M.; Castro-García, S.; Llamas-Saiz, A. L.; Artiaga, R.; López-Beceiro, J.; Hu, S.; Ren, W.; Stroppa, A.; Sánchez-Andújar, M.; et al. Phase Transition, Dielectric Properties, and Ionic Transport in the $[(CH_3)_2NH_2]PbI_3$ Organic-Inorganic Hybrid with 2H-Hexagonal Perovskite Structure. *Inorg. Chem.* **2017**, *56*, 4918−4927.
(346) García-Fernández, A.; Juarez-Perez, E. J.; Bermúdez-García, J. M.; Llamas-Saiz, A. L.; Artiaga, R.; López-Beceiro, J. J.; Señarís-Rodríguez, M. A.; Sánchez-Andújar, M.; Castro-García, S. Hybrid Lead Halide $[(CH_3)_2NH_2]PbX_3$ (X = Cl^- and Br^-) Hexagonal Perovskites with Multiple Functional Properties. *J. Mater. Chem. C* **2019**, *7*, 10008−10018.
(347) Im, J.-H.; Chung, J.; Kim, S.-J.; Park, N.-G. Synthesis, Structure, and Photovoltaic Property of a Nanocrystalline 2H Perovskite-Type Novel Sensitizer $(CH_3CH_2NH_3)PbI_3$. *Nanoscale Res. Lett.* **2012**, *7*, 353.
(348) Lin, C.-W.; Liu, F.; Chen, T.-Y.; Lee, K.-H.; Chang, C.-K.; He, Y.; Leung, T. L.; Ng, A. M. C.; Hsu, C.-H.; Popović, J.; et al. Structure-Dependent Photoluminescence in Low-Dimensional Ethylammonium, Propylammonium, and Butylammonium Lead Iodide Perovskites. *ACS Appl. Mater. Interfaces* **2020**, *12*, 5008−5016.

https://doi.org/10.1021/acs.chemrev.3c00532
Chem. Rev. 2024, 124, 2281−2326

(349) Jung, M.-H. Exploration of Two-Dimensional Perovskites Incorporating Methylammonium for High Performance Solar Cells. *CrystEngComm* **2021**, *23*, 1181−1200.
(350) Peng, W.; Miao, X.; Adinolfi, V.; Alarousu, E.; El Tall, O.; Emwas, A.-H.; Zhao, C.; Walters, G.; Liu, J.; Ouellette, O.; et al. Engineering of $CH_3NH_3PbI_3$ Perovskite Crystals by Alloying Large Organic Cations for Enhanced Thermal Stability and Transport Properties. *Angew. Chem., Int. Ed.* **2016**, *55*, 10686−10690.
(351) Wu, C.; Chen, K.; Guo, D. Y.; Wang, S. L.; Li, P. G. Cations Substitution Tuning Phase Stability in Hybrid Perovskite Single Crystals by Strain Relaxation. *RSC Adv.* **2018**, *8*, 2900−2905.
(352) Wang, Y.; Zhang, T.; Li, G.; Xu, F.; Wang, T.; Li, Y.; Yang, Y.; Zhao, Y. A Mixed-Cation Lead Iodide $MA_{1-x}EA_xPbI_3$ Absorber for Perovskite Solar Cells. *J. Energy Chem.* **2018**, *27*, 215−218.
(353) Vega, E.; Mollar, M.; Marí, B. Effect of Guanidinium on the Optical Properties and Structure of the Methylammonium Lead Halide Perovskite. *J. Alloys Compd.* **2018**, *739*, 1059−1064.
(354) Wang, W.; Xu, Q. Guanidinium Cation Doped $(Gua)_x(MA)_{1-x}PbI_3$ Single Crystal for High Performance X-Ray Detector. *Nucl. Instrum. Methods Phys. Res., Sect. A* **2021**, *1000*, No. 165234.
(355) Minussi, F. B.; Bertoletti, E. M.; Reis, S. P.; Carvalho, J. F.; Araújo, E. B. Guanidinium Substitution-Dependent Phase Transitions, Ionic Conductivity, and Dielectric Properties of $MAPbI_3$. *Chem. Commun.* **2022**, *58*, 2212−2215.
(356) Minussi, F. B.; Silva, L. A.; Araújo, E. B. Structure, Optoelectronic Properties and Thermal Stability of the Triple Organic Cation GA_xFA_xMA1- $2xPbI_3$ System Prepared by Mechanochemical Synthesis. *Phys. Chem. Chem. Phys.* **2022**, *24*, 4715−4728.
(357) Minussi, F. B.; Silva, R. M., Jr.; Araújo, E. B. Composition-Property Relations for $GA_xFA_yMA_{1-x-y}PbI_3$ Perovskites. *Small* **2023**, *20*, No. 2305054.
(358) Minussi, F. B.; da Silva, R. M. J.; Araújo, E. B. Differing Effects of Mixed A-Site Composition on the Properties of Hybrid Lead Iodide Perovskites. *J. Phys. Chem. C* **2023**, *127*, 8814−8824.
(359) Saliba, M.; Matsui, T.; Domanski, K.; Seo, J.-Y.; Ummadisingu, A.; Zakeeruddin, S. M.; Correa-Baena, J.-P.; Tress, W. R.; Abate, A.; Hagfeldt, A.; et al. Incorporation of Rubidium Cations into Perovskite Solar Cells Improves Photovoltaic Performance. *Science* **2016**, *354*, 206−209.
(360) Aebli, M.; Porenta, N.; Aregger, N.; Kovalenko, M. V. Local Structure of Multinary Hybrid Lead Halide Perovskites Investigated by Nuclear Quadrupole Resonance Spectroscopy. *Chem. Mater.* **2021**, *33*, 6965−6973.
(361) Mundt, L. E.; Zhang, F.; Palmstrom, A. F.; Xu, J.; Tirawat, R.; Kelly, L. L.; Stone, K. H.; Zhu, K.; Berry, J. J.; Toney, M. F.; et al. Mixing Matters: Nanoscale Heterogeneity and Stability in Metal Halide Perovskite Solar Cells. *ACS Energy Lett.* **2022**, *7*, 471−480.
(362) Shannon, R. D. Revised Effective Ionic Radii and Systematic Studies of Interatomic Distances in Halides and Chalcogenides. *Acta Crystallogr., Sect. A* **1976**, *32*, 751−767.
(363) Noh, J. H.; Im, S. H.; Heo, J. H.; Mandal, T. N.; Seok, S. I. Chemical Management for Colorful, Efficient, and Stable Inorganic-Organic Hybrid Nanostructured Solar Cells. *Nano Lett.* **2013**, *13*, 1764−1769.
(364) Niemann, R. G.; Kontos, A. G.; Palles, D.; Kamitsos, E. I.; Kaltzoglou, A.; Brivio, F.; Falaras, P.; Cameron, P. J. Halogen Effects on Ordering and Bonding of CH3NH3+ in $CH_3NH_3PbX_3$ (X = Cl, Br, I) Hybrid Perovskites: A Vibrational Spectroscopic Study. *J. Phys. Chem. C* **2016**, *120*, 2509−2519.
(365) Shahrokhi, S.; Dubajic, M.; Dai, Z.-Z.; Bhattacharyya, S.; Mole, R. A.; Rule, K. C.; Bhadbhade, M.; Tian, R.; Mussakhanuly, N.; Guan, X.; Yin, Y.; Nielsen, M. P.; Hu, L.; Lin, C.-H.; Chang, S. L. Y.; Wang, D.; Kabakova, I. V.; Conibeer, G.; Bremner, S.; Li, X.-G.; Cazorla, C.; Wu, T. Anomalous Structural Evolution and Glassy Lattice in Mixed-Halide Hybrid Perovskites. *Small* **2022**, *18*, No. 2200847.
(366) Brivio, F.; Caetano, C.; Walsh, A. Thermodynamic Origin of Photoinstability in the $CH_3NH_3Pb(I_{1-x}Br_x)_3$ Hybrid Halide Perovskite Alloy. *J. Phys. Chem. Lett.* **2016**, *7*, 1083−1087.
(367) Lehmann, F.; Franz, A.; Többens, D. M.; Levcenco, S.; Unold, T.; Taubert, A.; Schorr, S. The Phase Diagram of a Mixed Halide (Br, I) Hybrid Perovskite Obtained by Synchrotron X-Ray Diffraction. *RSC Adv.* **2019**, *9*, 11151−11159.
(368) Tang, S.; Xiao, X.; Hu, J.; Gao, B.; Chen, H.; Peng, Z.; Wen, J.; Era, M.; Zou, D. Solvent-Free Mechanochemical Synthesis of a Systematic Series of Pure-Phase Mixed-Halide Perovskites $MAPb(I_xBr_{1-x})_3$ and $MAPb(Br_xCl_{1-x})_3$ for Continuous Composition and Band-Gap Tuning. *ChemPlusChem.* **2020**, *85*, 240−246.
(369) Selig, O.; Sadhanala, A.; Müller, C.; Lovrincic, R.; Chen, Z.; Rezus, Y. L. A.; Frost, J. M.; Jansen, T. L. C.; Bakulin, A. A. Organic Cation Rotation and Immobilization in Pure and Mixed Methylammonium Lead-Halide Perovskites. *J. Am. Chem. Soc.* **2017**, *139*, 4068−4074.
(370) Askar, A. M.; Karmakar, A.; Bernard, G. M.; Ha, M.; Terskikh, V. V.; Wiltshire, B. D.; Patel, S.; Fleet, J.; Shankar, K.; Michaelis, V. K. Composition-Tunable Formamidinium Lead Mixed Halide Perovskites via Solvent-Free Mechanochemical Synthesis: Decoding the Pb Environments Using Solid-State NMR Spectroscopy. *J. Phys. Chem. Lett.* **2018**, *9*, 2671−2677.
(371) López, C. A.; Alvarez-Galván, M. C.; Martínez-Huerta, M. V.; Fauth, F.; Alonso, J. A. Crystal Structure Features of $CH_3NH_3PbI_{3-x}Br_x$ Hybrid Perovskites Prepared by Ball Milling: a Route to More Stable Materials. *CrystEngComm* **2020**, *22*, 767−775.
(372) Colella, S.; Mosconi, E.; Fedeli, P.; Listorti, A.; Gazza, F.; Orlandi, F.; Ferro, P.; Besagni, T.; Rizzo, A.; Calestani, G.; et al. $MAPbI_{3-x}Cl_x$ Mixed Halide Perovskite for Hybrid Solar Cells: The Role of Chloride as Dopant on the Transport and Structural Properties. *Chem. Mater.* **2013**, *25*, 4613−4618.
(373) Unger, E. L.; Bowring, A. R.; Tassone, C. J.; Pool, V. L.; Gold-Parker, A.; Cheacharoen, R.; Stone, K. H.; Hoke, E. T.; Toney, M. F.; McGehee, M. D. Chloride in Lead Chloride-Derived Organo-Metal Halides for Perovskite-Absorber Solar Cells. *Chem. Mater.* **2014**, *26*, 7158−7165.
(374) Pistor, P.; Borchert, J.; Fränzel, W.; Csuk, R.; Scheer, R. Monitoring the Phase Formation of Coevaporated Lead Halide Perovskite Thin Films by in Situ X-ray Diffraction. *J. Phys. Chem. Lett.* **2014**, *5*, 3308−3312.
(375) Franz, A.; Többens, D. M.; Steckhan, J.; Schorr, S. Determination of the Miscibility Gap in the Solid Solutions Series of Methylammonium Lead Iodide/Chloride. *Acta Crystallogr., Sect. B* **2018**, *74*, 445−449.
(376) Schuck, G.; Lehmann, F.; Ollivier, J.; Mutka, H.; Schorr, S. Influence of Chloride Substitution on the Rotational Dynamics of Methylammonium in $MAPbI_{3-x}Cl_x$ Perovskites. *J. Phys. Chem. C* **2019**, *123*, 11436−11446.
(377) Naqvi, F. H.; Ko, J.-H.; Kim, T. H.; Ahn, C. W.; Hwang, Y. Disentangled Structural and Vibrational Characteristics of Methylammonium Halide Perovskite $MAPbBr_{3-x}Cl_x$ with x = 0 ∼ 3 Studied by X-Ray Diffraction and Raman Scattering. *Curr. Appl. Phys.* **2022**, *44*, 150−157.
(378) Lee, A. Y.; Park, D. Y.; Jeong, M. S. Correlational Study of Halogen Tuning Effect in Hybrid Perovskite Single Crystals with Raman Scattering, X-Ray Diffraction, and Absorption Spectroscopy. *J. Alloys Compd.* **2018**, *738*, 239−245.
(379) López, C. A.; Álvarez Galván, M. C.; Martínez-Huerta, M. V.; Fernández-Díaz, M. T.; Alonso, J. A. Dynamic Disorder Restriction of Methylammonium (MA) Groups in Chloride-Doped $MAPbBr_3$ Hybrid Perovskites: A Neutron Powder Diffraction Study. *Chem.—Eur. J.* **2019**, *25*, 4496−4500.
(380) Alvarez-Galván, M. C.; Alonso, J. A.; López, C. A.; López-Linares, E.; Contreras, C.; Lázaro, M. J.; Fauth, F.; Martínez-Huerta, M. V. Crystal Growth, Structural Phase Transitions, and Optical Gap Evolution of $CH_3NH_3Pb(Br_{1-x}Cl_x)_3$ Perovskites. *Cryst. Growth Des.* **2019**, *19*, 918−924.

https://doi.org/10.1021/acs.chemrev.3c00532
Chem. Rev. 2024, 124, 2281−2326

(381) van de Goor, T. W. J.; Liu, Y.; Feldmann, S.; Bourelle, S. A.; Neumann, T.; Winkler, T.; Kelly, N. D.; Liu, C.; Jones, M. A.; Emge, S. P.; et al. Impact of Orientational Glass Formation and Local Strain on Photo-Induced Halide Segregation in Hybrid Metal-Halide Perovskites. *J. Phys. Chem. C* **2021**, *125*, 15025−15034.
(382) Karmakar, A.; Askar, A. M.; Bernard, G. M.; Terskikh, V. V.; Ha, M.; Patel, S.; Shankar, K.; Michaelis, V. K. Mechanochemical Synthesis of Methylammonium Lead Mixed-Halide Perovskites: Unraveling the Solid-Solution Behavior Using Solid-State NMR. *Chem. Mater.* **2018**, *30*, 2309−2321.
(383) Schuck, G.; Többens, D. M.; Wallacher, D.; Grimm, N.; Tien, T. S.; Schorr, S. Temperature-Dependent EXAFS Measurements of the Pb L3-Edge Allow Quantification of the Anharmonicity of the Lead-Halide Bond of Chlorine-Substituted Methylammonium (MA) Lead Triiodide. *J. Phys. Chem. C* **2022**, *126*, 5388−5402.
(384) Näsström, H.; Becker, P.; Márquez, J. A.; Shargaieva, O.; Mainz, R.; Unger, E.; Unold, T. Dependence of Phase Transitions on Halide Ratio in Inorganic $CsPb(Br_xI_{1-x})_3$ Perovskite Thin Films Obtained from High-Throughput Experimentation. *J. Mater. Chem. A* **2020**, *8*, 22626−22631.
(385) Ma, J.; Qin, M.; Li, Y.; Wu, X.; Qin, Z.; Wu, Y.; Fang, G.; Lu, X. Unraveling the Impact of Halide Mixing on Crystallization and Phase Evolution in $CsPbX_3$ Perovskite Solar Cells. *Matter* **2021**, *4*, 313−327.
(386) Yuan, L.; Yuan, M.; Xu, H.; Hou, C.; Meng, X. Moisture-Stimulated Reversible Thermochromic $CsPbI_{3-x}Br_x$ Films: In-Situ Spectroscopic-Resolved Structure and Optical Properties. *Appl. Surf. Sci.* **2022**, *573*, No. 151484.
(387) Wang, Y.; Guan, X.; Chen, W.; Yang, J.; Hu, L.; Yang, J.; Li, S.; Kalantar-Zadeh, K.; Wen, X.; Wu, T. Illumination-Induced Phase Segregation and Suppressed Solubility Limit in Br-Rich Mixed-Halide Inorganic Perovskites. *ACS Appl. Mater. Interfaces* **2020**, *12*, 38376−38385.
(388) Breniaux, E.; Dufour, P.; Guillemet-Fritsch, S.; Tenailleau, C. Unraveling All-Inorganic $CsPbI_3$ and $CsPbI_2Br$ Perovskite Thin Films Formation - Black Phase Stabilization by $Cs_2PbCl_2I_2$ Addition and Flash-Annealing. *Eur. J. Inorg. Chem.* **2021**, *2021*, 3059−3073.
(389) Jung, J.; Yun, Y.; Yang, S. W.; Oh, H. G.; Jeon, A.-Y.; Nam, Y.; Heo, Y.-W.; Chae, W.-S.; Lee, S. Ternary Diagrams of Phase, Stability, and Optical Properties of Cesium Lead Mixed-Halide Perovskites. *Acta Mater.* **2023**, *246*, No. 118661.
(390) Chen, K.; Deng, X.; Goddard, R.; Tüysüz, H. Pseudomorphic Transformation of Organometal Halide Perovskite Using the Gaseous Hydrogen Halide Reaction. *Chem. Mater.* **2016**, *28*, 5530−5537.
(391) Maczka, M.; Ptak, M.; Gagor, A.; Stefanska, D.; Sieradzki, A. Layered Lead Iodide of $[Methylhydrazinium]_2PbI_4$ with a Reduced Band Gap: Thermochromic Luminescence and Switchable Dielectric Properties Triggered by Structural Phase Transitions. *Chem. Mater.* **2019**, *31*, 8563−8575.
(392) Greenland, C.; Shnier, A.; Rajendran, S. K.; Smith, J. A.; Game, O. S.; Wamwangi, D.; Turnbull, G. A.; Samuel, I. D. W.; Billing, D. G.; Lidzey, D. G. Correlating Phase Behavior with Photophysical Properties in Mixed-Cation Mixed-Halide Perovskite Thin Films. *Adv. Energy Mater.* **2020**, *10*, No. 1901350.
(393) Menéndez-Proupin, E.; Grover, S.; Montero-Alejo, A. L.; Midgley, S. D.; Butler, K. T.; Grau-Crespo, R. Mixed-Anion Mixed-Cation Perovskite $(FAPbI_3)_{0.875}(MAPbBr_3)_{0.125}$: an Ab Initio Molecular Dynamics Study. *J. Mater. Chem. A* **2022**, *10*, 9592−9603.
(394) Johnston, A.; Walters, G.; Saidaminov, M. I.; Huang, Z.; Bertens, K.; Jalarvo, N.; Sargent, E. H. Bromine Incorporation and Suppressed Cation Rotation in Mixed-Halide Perovskites. *ACS Nano* **2020**, *14*, 15107−15118.
(395) Xie, L.-Q.; Chen, L.; Nan, Z.-A.; Lin, H.-X.; Wang, T.; Zhan, D.-P.; Yan, J.-W.; Mao, B.-W.; Tian, Z.-Q. Understanding the Cubic Phase Stabilization and Crystallization Kinetics in Mixed Cations and Halides Perovskite Single Crystals. *J. Am. Chem. Soc.* **2017**, *139*, 3320−3323.
(396) Barrier, J.; Beal, R. E.; Gold-Parker, A.; Vigil, J. A.; Wolf, E.; Waquier, L.; Weadock, N. J.; Zhang, Z.; Schelhas, L. T.; Nogueira, A. F.; et al. Compositional Heterogeneity in $Cs_yFA_{1-y}Pb(Br_xI_{1-x})_3$ Perovskite Films and Its Impact on Phase Behavior. *Energy Environ. Sci.* **2021**, *14*, 6394−6405.
(397) Ye, H.-Y.; Liao, W.-Q.; Hu, C.-L.; Zhang, Y.; You, Y.-M.; Mao, J.-G.; Li, P.-F.; Xiong, R.-G. Bandgap Engineering of Lead-Halide Perovskite-Type Ferroelectrics. *Adv. Mater.* **2016**, *28*, 2579−2586.
(398) Abid, H.; Trigui, A.; Mlayah, A.; Hlil, E.; Abid, Y. Phase Transition in Organic-Inorganic Perovskite $(C_9H_{19}NH_3)_2PbI_2Br_2$ of Long-Chain Alkylammonium. *Results Phys.* **2012**, *2*, 71−76.
(399) Wright, N. E.; Qin, X.; Xu, J.; Kelly, L. L.; Harvey, S. P.; Toney, M. F.; Blum, V.; Stiff-Roberts, A. D. Influence of Annealing and Composition on the Crystal Structure of Mixed-Halide, Ruddlesden-Popper Perovskites. *Chem. Mater.* **2022**, *34*, 3109−3122.
(400) Roy, C. R.; Zhou, Y.; Kohler, D. D.; Zhu, Z.; Wright, J. C.; Jin, S. Intrinsic Halide Immiscibility in 2D Mixed-Halide Ruddlesden-Popper Perovskites. *ACS Energy Lett.* **2022**, *7*, 3423−3431.
(401) Calabrese, J.; Jones, N. L.; Harlow, R. L.; Herron, N.; Thorn, D. L.; Wang, Y. Preparation and Characterization of Layered Lead Halide Compounds. *J. Am. Chem. Soc.* **1991**, *113*, 2328−2330.
(402) Vasileiadou, E. S.; Jiang, X.; Kepenekian, M.; Even, J.; De Siena, M. C.; Klepov, V. V.; Friedrich, D.; Spanopoulos, I.; Tu, Q.; Tajuddin, I. S.; et al. Thick-Layer Lead Iodide Perovskites with Bifunctional Organic Spacers Allylammonium and Iodopropylammonium Exhibiting Trap-State Emission. *J. Am. Chem. Soc.* **2022**, *144*, 6390−6409.
(403) Ma, Y.; Li, W.; Liu, Y.; Guo, W.; Xu, H.; Han, S.; Tang, L.; Fan, Q.; Luo, J.; Sun, Z. Mixing Cage Cations in 2D Metal-Halide Ferroelectrics Enhances the Ferro-Pyro-Phototronic Effect for Self-Driven Photopyroelectric Detection. *Chem. Sci.* **2023**, *14*, 10347−10352.
(404) Mishra, A.; Kubicki, D. J.; Boziki, A.; Chavan, R. D.; Dankl, M.; Mladenović, M.; Prochowicz, D.; Grey, C. P.; Rothlisberger, U.; Emsley, L. Interplay of Kinetic and Thermodynamic Reaction Control Explains Incorporation of Dimethylammonium Iodide into CsPbI3. *ACS Energy Lett.* **2022**, *7*, 2745−2752.
(405) Wang, K.; Tang, M.-C.; Dang, H. X.; Munir, R.; Barrit, D.; De Bastiani, M.; Aydin, E.; Smilgies, D.-M.; De Wolf, S.; Amassian, A. Kinetic Stabilization of the Sol-Gel State in Perovskites Enables Facile Processing of High-Efficiency Solar Cells. *Adv. Mater.* **2019**, *31*, No. 1808357.
(406) Leblanc, A.; Mercier, N.; Allain, M.; Dittmer, J.; Fernandez, V.; Pauporté, T. Lead- and Iodide-Deficient $(CH_3NH_3)PbI_3$ (d-MAPI): The Bridge between 2D and 3D Hybrid Perovskites. *Angew. Chem., Int. Ed.* **2017**, *56*, 16067−16072.
(407) Li, N.; Zhu, Z.; Chueh, C.-C.; Liu, H.; Peng, B.; Petrone, A.; Li, X.; Wang, L.; Jen, A. K.-Y. Mixed Cation $FA_xPEA_{1-x}PbI_3$ with Enhanced Phase and Ambient Stability toward High-Performance Perovskite Solar Cells. *Adv. Energy Mater.* **2017**, *7*, No. 1601307.
(408) Stefanska, D.; Ptak, M.; Maczka, M. Synthesis, Photoluminescence and Vibrational Properties of Aziridinium Lead Halide Perovskites. *Molecules* **2022**, *27*, 7949.
(409) Semenikhin, O. A.; Kucheriv, O. I.; Sacarescu, L.; Shova, S.; Gural'skiy, I. A. Quantum Dots Assembled from an Aziridinium Based Hybrid Perovskite Displaying Tunable Luminescence. *Chem. Commun.* **2023**, *59*, 3566−3569.
(410) Laurita, G.; Fabini, D. H.; Stoumpos, C. C.; Kanatzidis, M. G.; Seshadri, R. Chemical Tuning of Dynamic Cation Off-Centering in the Cubic Phases of Hybrid Tin and Lead Halide Perovskites. *Chem. Sci.* **2017**, *8*, 5628−5635.
(411) Marshall, A. R.; Sansom, H. C.; McCarthy, M. M.; Warby, J. H.; Ashton, O. J.; Wenger, B.; Snaith, H. Dimethylammonium: An A-Site Cation for Modifying $CsPbI_3$. *Sol. RRL* **2021**, *5*, No. 2000599.
(412) Wang, Z.; Zeng, L.; Zhu, T.; Chen, H.; Chen, B.; Kubicki, D. J.; Balvanz, A.; Li, C.; Maxwell, A.; Ugur, E. Suppressed Phase Segregation for Triple-Junction Perovskite Solar Cells. *Nature* **2023**, *618*, 74−79.
(413) Duijnstee, E. A.; Gallant, B. M.; Holzhey, P.; Kubicki, D. J.; Collavini, S.; Sturdza, B. K.; Sansom, H. C.; Smith, J.; Gutmann, M. J.; Saha, S.; et al. Understanding the Degradation of Methylenediammo-

https://doi.org/10.1021/acs.chemrev.3c00532
Chem. Rev. 2024, 124, 2281−2326

nium and Its Role in Phase-Stabilizing Formamidinium Lead Triiodide. *J. Am. Chem. Soc.* **2023**, *145*, 10275−10284.
(414) Teri, G.; Ni, H.-F.; Luo, Q.-F.; Wang, X.-P.; Wang, J.-Q.; Fu, D.-W.; Guo, Q. Tin-Based Organic-Inorganic Metal Halides with a Reversible Phase Transition and Thermochromic Response. *Mater. Chem. Front.* **2023**, *7*, 2235−2240.
(415) Liu, X.; Ji, C.; Wu, Z.; Li, L.; Han, S.; Wang, Y.; Sun, Z.; Luo, J. $[C_5H_{12}N]SnCl_3$: A Tin Halide Organic-Inorganic Hybrid as an Above-Room-Temperature Solid-State Nonlinear Optical Switch. *Chem.—Eur. J.* **2019**, *25*, 2610−2615.
(416) Zhang, W.; Hong, M.; Luo, J. Centimeter-Sized Single Crystal of a One-Dimensional Lead-Free Mixed-Cation Perovskite Ferroelectric for Highly Polarization Sensitive Photodetection. *J. Am. Chem. Soc.* **2021**, *143*, 16758−16767.
(417) Jakubas, R.; Rok, M.; Mencel, K.; Bator, G.; Piecha-Bisiorek, A. Correlation Between Crystal Structures and Polar (Ferroelectric) Properties of Hybrids of Haloantimonates(III) and Halobismuthates-(III). *Inorg. Chem. Front.* **2020**, *7*, 2107−2128.
(418) Zhang, H.-Y.; Wei, Z.; Li, P.-F.; Tang, Y.-Y.; Liao, W.-Q.; Ye, H.-Y.; Cai, H.; Xiong, R.-G. The Narrowest Band Gap Ever Observed in Molecular Ferroelectrics: Hexane-1,6-diammonium Pentaiodobismuth(III). *Angew. Chem., Int. Ed.* **2018**, *57*, 526−530.
(419) Szklarz, P.; Gagor, A.; Jakubas, R.; Zielinski, P.; Piecha-Bisiorek, A.; Cichos, J.; Karbowiak, M.; Bator, G.; Cizman, A. Lead-Free Hybrid Ferroelectric Material Based on Formamidine: $[NH_2CHNH_2]_3Bi_2I_9$. *J. Mater. Chem. C* **2019**, *7*, 3003−3014.
(420) Wang, B.; Ma, D.; Zhao, H.; Long, L.; Zheng, L. Room Temperature Lead-Free Multiaxial Inorganic-Organic Hybrid Ferroelectric. *Inorg. Chem.* **2019**, *58*, 13953−13959.
(421) Wang, Y.; Shi, C.; Han, X.-B. Mixed Bromine-Chlorine Induced Great Dielectric and Second-Order Nonlinear Optical Properties Changes in Phase Transitions Compounds $[H_2mdap][BiBr_5(1- x)Cl_{5x}]$($x$ = 0.00 − 1.00). *J. Phys. Chem. C* **2017**, *121*, 23039−23044.
(422) Ju, D.; Zheng, X.; Yin, J.; Qiu, Z.; Türedi, B.; Liu, X.; Dang, Y.; Cao, B.; Mohammed, O. F.; Bakr, O. M.; et al. Tellurium-Based Double Perovskites A2TeX6 with Tunable Band Gap and Long Carrier Diffusion Length for Optoelectronic Applications. *ACS Energy Lett.* **2019**, *4*, 228−234.
(423) Wei, F.; Deng, Z.; Sun, S.; Xie, F.; Kieslich, G.; Evans, D. M.; Carpenter, M. A.; Bristowe, P. D.; Cheetham, A. K. The Synthesis, Structure and Electronic Properties of a Lead-Free Hybrid Inorganic-Organic Double Perovskite $(MA)_2KBiCl_6$ (MA = methylammonium). *Mater. Horiz.* **2016**, *3*, 328−332.
(424) Liu, X.; Xu, Z.; Long, P.; Yao, Y.; Ji, C.; Li, L.; Sun, Z.; Hong, M.; Luo, J. A Multiaxial Layered Halide Double Perovskite Ferroelectric with Multiple Ferroic Orders. *Chem. Mater.* **2020**, *32*, 8965−8970.
(425) He, L.; Shi, P.-P.; Zhou, L.; Liu, Z.-B.; Zhang, W.; Ye, Q. Coexisting Ferroelectric and Ferroelastic Orders in Rare 3D Homochiral Hybrid Bimetal Halides. *Chem. Mater.* **2021**, *33*, 6233−6239.
(426) Zhou, J.; Xie, P.; Wang, C.; Bian, T.; Chen, J.; Liu, Y.; Guo, Z.; Chen, C.; Pan, X.; Luo, M.; Yin, J.; Mao, L. Hybrid Double Perovskite Derived Halides Based on Bi and Alkali Metals (K, Rb): Diverse Structures, Tunable Optical Properties and Second Harmonic Generation Responses. *Angew. Chem., Int. Ed.* **2023**, *62*, No. e202307646.
(427) Wei, F.; Deng, Z.; Sun, S.; Zhang, F.; Evans, D. M.; Kieslich, G.; Tominaka, S.; Carpenter, M. A.; Zhang, J.; Bristowe, P. D.; et al. Synthesis and Properties of a Lead-Free Hybrid Double Perovskite: $(CH_3NH_3)_2AgBiBr_6$. *Chem. Mater.* **2017**, *29*, 1089−1094.
(428) Long, G.; Sabatini, R.; Saidaminov, M. I.; Lakhwani, G.; Rasmita, A.; Liu, X.; Sargent, E. H.; Gao, W. Chiral-Perovskite Optoelectronics. *Nat. Rev. Mater.* **2020**, *5*, 423−439.
(429) Ma, J.; Wang, H.; Li, D. Recent Progress of Chiral Perovskites: Materials, Synthesis, and Properties. *Adv. Mater.* **2021**, *33*, No. 2008785.
(430) Dong, Y.; Zhang, Y.; Li, X.; Feng, Y.; Zhang, H.; Xu, J. Chiral Perovskites: Promising Materials toward Next-Generation Optoelectronics. *Small* **2019**, *15*, No. 1902237.
(431) Leng, K.; Li, R.; Lau, S. P.; Loh, K. P. Ferroelectricity and Rashba Effect in 2D Organic-Inorganic Hybrid Perovskites. *Trends Chem.* **2021**, *3*, 716−732.
(432) Huang, P.-J.; Taniguchi, K.; Miyasaka, H. Bulk Photovoltaic Effect in a Pair of Chiral-Polar Layered Perovskite-Type Lead Iodides Altered by Chirality of Organic Cations. *J. Am. Chem. Soc.* **2019**, *141*, 14520−14523.
(433) Ahn, J.; Ma, S.; Kim, J.-Y.; Kyhm, J.; Yang, W.; Lim, J. A.; Kotov, N. A.; Moon, J. Chiral 2D Organic Inorganic Hybrid Perovskite with Circular Dichroism Tunable Over Wide Wavelength Range. *J. Am. Chem. Soc.* **2020**, *142*, 4206−4212.
(434) Kim, Y.-H.; Zhai, Y.; Lu, H.; Pan, X.; Xiao, C.; Gaulding, E. A.; Harvey, S. P.; Berry, J. J.; Vardeny, Z. V.; Luther, J. M.; et al. Chiral-Induced Spin Selectivity Enables a Room-Temperature Spin Light-Emitting Diode. *Science* **2021**, *371*, 1129−1133.
(435) Huang, P.-J.; Taniguchi, K.; Miyasaka, H. Crucial Contribution of Polarity for the Bulk Photovoltaic Effect in a Series of Noncentrosymmetric Two-Dimensional Organic-Inorganic Hybrid Perovskites. *Chem. Mater.* **2022**, *34*, 4428−4436.
(436) Ma, J.; Fang, C.; Chen, C.; Jin, L.; Wang, J.; Wang, S.; Tang, J.; Li, D. Chiral 2D Perovskites with a High Degree of Circularly Polarized Photoluminescence. *ACS Nano* **2019**, *13*, 3659−3665.
(437) Liu, S.; Heindl, M. W.; Fehn, N.; Caicedo-Dávila, S.; Eyre, L.; Kronawitter, S. M.; Zerhoch, J.; Bodnar, S.; Shcherbakov, A.; Stadlbauer, A.; et al. Optically Induced Long-Lived Chirality Memory in the Color-Tunable Chiral Lead-Free Semiconductor (R)/(S)-$CHEA_4Bi_2Br_xI_{10-x}$ (x = 0−10). *J. Am. Chem. Soc.* **2022**, *144*, 14079−14089.
(438) Yao, B.; Wei, Q.; Yang, Y.; Zhou, W.; Jiang, X.; Wang, H.; Ma, M.; Yu, D.; Yang, Y.; Ning, Z. Symmetry-Broken 2D Lead-Tin Mixed Chiral Perovskite for High Asymmetry Factor Circularly Polarized Light Detection. *Nano Lett.* **2023**, *23*, 1938−1945.
(439) Ahart, M.; Somayazulu, M.; Cohen, R. E.; Ganesh, P.; Dera, P.; Mao, H.-k.; Hemley, R. J.; Ren, Y.; Liermann, P.; Wu, Z. Origin of Morphotropic Phase Boundaries in Ferroelectrics. *Nature* **2008**, *451*, 545−548.

https://doi.org/10.1021/acs.chemrev.3c00532
Chem. Rev. 2024, 124, 2281−2326